DOKUZ EYLÜL UNIVERSITY

GRADUATE SCHOOL OF NATURAL AND APPLIED SCIENCES

IMPROVEMENT OF PHOTOCATALYTIC PROPERTIES OF METAL OXIDE NANOPARTICLES

by

Serdar GÜLTEKİN

March, 2025

İZMİR

IMPROVEMENT OF PHOTOCATALYTIC PROPERTIES OF METAL OXIDE NANOPARTICLES

A Thesis Submitted to the
Graduate School of Natural and Applied Sciences of Dokuz Eylül University
In Partial Fulfillment of the Requirements for the Degree of Doctor of Philosophy in Department of Metalurgy and Material Engineering, Metallurgy and Material Engineering Program

by

Serdar GÜLTEKİN

March, 2025

İZMİR

Ph.D. THESIS EXAMINATION RESULT FORM

We have read the thesis entitled **"IMPROVEMENT OF PHOTOCATALYTIC PROPERTIES OF METAL OXIDE NANOPARTICLES"** completed by **SERDAR GÜLTEKİN** under supervision of **ASSOC.PROF.DR. IŞIL BİRLİK** and we certify that in our opinion it is fully adequate, in scope and in quality, as a thesis for the degree of Doctor of Philosophy.

Assoc.Prof.Dr. Işıl BİRLİK

Supervisor

Prof. Dr. Osman ÇULHA

Thesis Committee Member

Assoc. Prof. Dr. N. Funda AK AZEM

Thesis Committee Member

Prof. Dr. Nur AKSUNER

Examining Committee Member

Prof. Dr. Nüket TİRTOM

Examining Committee Member

Prof. Dr. Abdullah SEÇGİN

Director

Graduate School of Natural and Applied Sciences

ACKNOWLEDGMENT

Firstly, I would like to express my sincerest gratitude to my supervisor, Assoc. Prof. Dr. Işıl BİRLİK, for her priceless advices, invaluable experiences, his constructive ideas and scientific guidance throughout the course of this thesis. I extend my heartfelt appreciation to esteemed Prof. Dr. Erdal ÇELIK, for his unwavering mentorship and continuous encouragement in all aspects of my academic career.

I am also immensely grateful to Assoc. Prof. Dr. N. Funda AK AZEM and Prof. Dr. Osman ÇULHA. Prof Dr. Kadriye Ertekin for their valuable support and suggestion at all times. My thanks extend to Assoc. Prof. Dr. Tuncay DİKİCİ and Assoc. Prof. Dr. Ramazan DALMIŞ, Assoc. Prof. Dr. Sibel OĞUZLAR, Dr. Mehmet İsmail KATI, Dr. İlker Çetin KESKİN and Özgür Yasin KESKİN for their invaluable help during challenging times.

I extend my sincere gratitude to my dear friend Dr. Ozan YILMAZ, whose continuous support and friendship have always been with me. I also would like to thank dear Enes KARABULUT amd F. Okan US for their valuable helps.

I owe my deepest gratitude to my dear aunt, Prof. Dr. Fatma KOYUNCU, and her husband, Prof. Dr. M. Ali KOYUNCU, for their unwavering support and guidance throughout my entire educational journey.

A special thank goes to my beloved parents, Kasım GÜLTEKİN and Şükriye GÜLTEKİN, as well as my siblings, Kibar GÜLTEKİN KURT and Cihangir GÜLTEKİN, for their enduring support, encouragement, and guidance, which have been the foundation of my achievements.

Last but not least, I would like to express my deepest appreciation to my dear wife Sıdıka YILDIRIM GÜLTEKİN, whose encouragement and essential assistance provided invaluable strength throughout this journey. This accomplishment would not have been possible without her by my side.

Serdar GÜLTEKİN

IMPROVEMENT OF PHOTOCATALYTIC PROPERTIES OF METAL OXIDE NANOPARTICLES

ABSTRACT

Zinc oxide nanoparticles, yttrium oxide, yttrium aluminum garnet (YAG), and their composites were synthesized for photocatalytic studies. Pure zinc oxide, as a photocatalyst, and yttrium oxide and YAG, as photoluminescent materials, were produced using the sol-gel method. Zinc oxide-yttrium oxide and zinc oxide-YAG composites were prepared via mechanical mixing and chemical precipitation. Europium and cerium doped yttrium oxide and YAG materials were also synthesized for comparison purposes. During synthesis, pH and turbidity were monitored, and DTA and FTIR analyses identified optimal production parameters. Characterization of the synthesized materials was carried out using XRD, SEM, BET and time-resolved photoluminescence devices.

The photocatalytic activity was evaluated by measuring methylene blue degradation using UV-VIS spectrophotometry. Bandgap energy of zinc oxide-yttrium oxide composites was determined by solid-state UV-VIS spectrophotometry. According to the results, while the zinc oxide-YAG composite exhibited poorer performance compared to pure zinc oxide, the zinc oxide-yttrium oxide composite demonstrated exceptionally strong photocatalytic performance. Additionally, europium and cerium doping did not enhance photocatalytic performance. Yttrium oxide, lacking its own photocatalytic activity, significantly improved zinc oxide's efficiency in composites. Zinc oxide-yttrium oxide (5 percent yttrium oxide by weight of zinc oxide) composite achieved 98.4 percent methylene blue degradation after 150 minutes of UV exposure, outperforming pure zinc oxide's 77 percent, due to energy transfer between the materials, which increased the photodegradation rate constant of zinc oxide from 0.009/min to 0.0242/min, showing its potential for advanced photocatalytic applications.

Keywords: Photocatalysis, Photoluminescence, sol-gel processes, Zinc oxide, Yttrium oxide, Composite

METAL OKSİT NANOPARTIKÜLLERİN FOTOKATALİTİK ÖZELLİKLERİNİN GELİŞTİRİLMESİ

ÖZ

Çinko oksit nanopartikülleri, itriyum oksit, itriyum alüminyum garnet (YAG) ve bunların kompozitleri fotokatalitik çalışmalar için sentezlenmiştir. Fotokatalizör olarak saf çinko oksit ile fotolüminesans özellikli itriyum oksit ve YAG sol-jel yöntemiyle üretilmiş, çinko oksit-itriyum oksit ve çinko oksit-YAG kompozitleri ise mekanik karıştırma ve kimyasal çöktürme yöntemleriyle hazırlanmıştır. Karşılaştırma amacıyla ayrıca, europium ve seryum katkılı itriyum oksit ve YAG malzemeleri de sentezlenmiştir. Sentez sırasında pH ve bulanıklık ölçümleri yapılmış, DTA ve FTIR analizleriyle optimum üretim parametreleri belirlenmiştir. Sentezlenen malzemelerin karakterizasyonu XRD, SEM, BET ve zaman çözümlemeli fotolüminesans cihazları kullanılarak gerçekleştirilmiştir..

Fotokatalitik aktivite, UV-VIS spektrofotometresi kullanılarak metilen mavisi bozunumu üzerinden değerlendirilmiştir. Çinko oksit-itriyum oksit kompozitlerinin band aralığı enerjisi katı hal UV-VIS ile belirlenmiştir. Sonuçlara göre, çinko oksit-YAG kompoziti saf çinko okside göre daha düşük fotokatalitik performans sergilerken, çinko oksit-itriyum oksit kompoziti son derece güçlü bir fotokatalitik performans göstermiştir. Ayrıca, europium ve seryum katkısı fotokatalitik performansı artırmamıştır. Kendi başına fotokatalitik aktivite göstermeyen itriyum oksit, çinko oksidin kompozitlerdeki verimliliğini önemli ölçüde artırmıştır. Çinko oksite göre ağırlıkça yüzde 5 itriyum oksit içeren kompozit 150 dakika UV ışınımı sonrasında metilen mavisinde yüzde 98,4 oranında bozunma sağlamış ve saf çinko oksidin yüzde 77'lik bozunma performansını büyük ölçüde aşmıştır. Bu iyileşme, itriyum oksit ve çinko oksit arasındaki enerji transferi mekanizmasına bağlanmakta olup, çinko oksidin fotobozunma hız sabitinin 0.009/dakikadan 0.0242/dakikaya artması ile doğrulanmıştır. Bu bulgu, çinko oksit-itriyum oksit kompozitlerinin ileri düzey fotokatalitik uygulamalardaki potansiyelini ortaya koymuştur.

Anahtar kelimeler: Fotokataliz, fotoluminesans, sol-jel, Çinko Oksit, Ytrium Oksit, Kompozit

CONTENTS

Page

Ph.D. THESIS EXAMINATION RESULT FORM ii
ACKNOWLEDGMENT iii
ABSTRACT iv
ÖZ v
CONTENTS vi
LIST OF FIGURES ix
LIST OF TABLES i

CHAPTER ONE - INTRODUCTION 1

1.1 General 1
1.2 Organization of the Thesis 5

CHAPTER TWO - THEORITICAL BACKGROUND 7

2.1 Photocatalysis 7
2.1.1 Mechanism and Basic Principles of Photocatalysis 7
2.1.2 Types of Photocatalytic Materials 9
2.1.3 Photocatalytic Processes 14
2.1.4 Improving Photocatalytic properties 16
2.1.5 Parameters Affecting Photocatalytic Performance 19
2.2 Luminescence 23
2.2.1 Mechanism of Luminescence 23
2.2.2 Photoluminescence 24
2.2.3 Luminescent Properties of Y_2O_3 and YAG 29
2.3 Production Techniques of Metal Oxides 33
2.3.1 Sol-Gel Process 34
2.3.2 Hydrolysis and Condensation Reaction 34
2.3.3 Gelation 35
2.3.4 Drying and Sintering 36

2.4 Motivation of the Research 36

CHAPTER THREE - EXPERIMENTAL STUDIES 38

3.1 The Aim of Thesis 38

3.2 Precursor Materials 39

3.3 Synthesis of ZnO Nanoparticles 40

3.4 Synthesis of undoped and doped Y_2O_3 Particles 42

3.5 $Y_3Al_5O_{12}$ (YAG) production 47

3.6 Composite ZnO-Y_2O_3 Production 50

3.7 ZnO-Y_2O_3 Production by Precipitation 51

3.8 Characterization 53

3.8.1 Solution Characterization 53

3.8.2 Material Characterization 55

3.8.3 Photocatalytic Characterization 58

3.8.4 Photoluminescence Characterization 59

CHAPTER FOUR - RESULTS AND DISCUSSION 61

4.1 Structural Characterization of ZnO Nanoparticles 61

4.2 Structural Characterization of Y_2O_3 powders 64

4.3 Luminescent Characterization of Y_2O_3 powders 74

4.4 Structural Characterization of ZnO-Y_2O_3 Composite Produced by Mechanical Mixing 77

4.5 Luminescent Characterization of ZnO-Y_2O_3 Composite Produced by Mechanical Mixing 82

4.6 Structural Characterization of Combine ZnO-Y_2O_3 Produced by Precipitation 85

4.7 Structural and Luminescent Characterization of YAG powders 88

4.8 Photocatalytic Analyzes 93

4.8.1 Photocatalytic Analyzes of Pure Y_2O_3 , YAG and ZnO 94
4.8.2 Photocatalytic Analyzes of Composite ZnO-Y_2O_3, ZnO-Y_2O_3;Eu, ZnO-Y_2O_3;Ce 96
4.8.3 Photocatalytic Analyzes of Combine ZnO-Y_2O_3 101
4.8.4 Photocatalytic Analyzes of Composite ZnO-YAG, ZnO-YAG;Eu and ZnO-YAG;Ce 101
4.8.5 Detailed photocatalytic studies of ZnO-Y_2O_3 composites 102

CHAPTER FIVE - CONCUSLUSION 107

REFERENCES 111

LIST OF FIGURES

Page

Figure 2.1 The (a) rocksalt (cubic) (b)zinc blende (cubic) and (c) wurtzite (hexagonal) structures model of ZnO 10

Figure 2.2 Schematic illustration of the photocatalytic mechanism of ZnO 11

Figure 2.3 Example of persistent phosphors synthesized in our laboratory 26

Figure 2.4 Schematic illustration of Jablonski diagram 28

Figure 2.5 Emission spectra of Y_2O_3:Eu^{3+} excited at 255 30

Figure 2.6 Emission spectra of YAG:Ce^{3+} excited at 455 nm 32

Figure 2.7 Emission spectra of YAG:Eu^{+3} excited at 395 32

Figure 2.8 (a) Site percolation and (b) bond percolation on a square bi-dimensional network 36

Figure 3.1 Heat treatment regime for ZnO 40

Figure 3.2 Flow chart of ZnO production 42

Figure 3.3 Heat treatment regime for Y_2O_3 44

Figure 3.4 Flow chart of pure, Eu doped, Ce doped Y_2O_3 production 46

Figure 3.5 Heat treatment regime for YAG 48

Figure 3.6 Flow chart of pure, Eu doped and Ce doped YAG production 49

Figure 3.7 Composite ZnO-Y_2O_3 samples preparation 51

Figure 3.8 Heat treatment regime for Combine ZnO-5Y_2O_3 produced by precipitation 52

Figure 3.9 Flow chart of combine ZnO-5Y_2O_3 production by precipitation 53

Figure 3.10 X-Ray Diffraction 56

Figure 4.1 DTA-TG analysis of dried ZnO xerogel powders 61

Figure 4.2 FTIR spectra of dried ZnO xerogel 62

Figure 4.3 XRD pattern of ZnO nanoparticles 63

Figure 4.4 SEM micrographs of pure ZnO 63

Figure 4.5 DTA-TG analysis of dried Y_2O_3 xerogel powders 64

Figure 4.6 FTIR spectra of dried Y_2O_3 gel with different acid concentration 65

Figure 4.7 XRD patterns of Y_2O_3 with 0.5, 1 and 2 MRCM 66

Figure 4.8 (a) XRD patterns of pure and Eu doped Y_2O_3 67

Figure 4.9 XRD patterns of pure, 1% Eu and 1% Ce doped Y_2O_3 68

Figure 4.10 SEM micrographs of Y_2O_3 0.5 MRCM 69

Figure 4.11 SEM micrographs of Y_2O_3 1 MRCM 70

Figure 4.12 SEM micrographs of Y_2O_3 2 MRCM 71

Figure 4.13 Post-drying states of Y_2O_3 materials synthesized with three different acid concentrations 71

Figure 4.14 BET transform plot of Y_2O_3 with 0.5, 1 and 2 MRCM 72

Figure 4.15 Isotherm Linear plot of Y_2O_3 with 0.5, 1 and 2 MRCM 74

Figure 4.16 Excitation and emission spectrum of pure Y_2O_3 (a); λ_{max}^{ex}:370 nm, λ_m (b) λ_{max}^{ex}:292 nm 75

Figure 4.17 Excitation and emission spectrum of Eu doped Y_2O_3 (a); λex:370 nm, (b) λex:292 nm 76

Figure 4.18 Excitation and emission spectrum of Ce doped Y_2O_3 (a); λ_{ex}:380 nm, (b) λ_{ex}:292 nm 77

Figure 4.19 (a) XRD pattern of composite ZnO-Y_2O_3 78

Figure 4.20 EDX mapping micrographs of **(a)** ZnO-2.5Y_2O_3, **(b)** ZnO-5Y_2O_3,**(c)** ZnO-10Y_2O_3 and **(d)** ZnO-20Y_2O_3 composites. 79

Figure 4.21 EDX elemental analysis of marked regions 81

Figure 4.22 (a); Reflectance spectra of ZnO-Y_2O_3 vs. wavelength, (b); $(F(R)h\nu)^{0.5}$ plot vs. photon energy (eV) 82

Figure 4.23 Excitation and emission spectrum of Y_2O_3 (λmax^{ex}:292 nm, λmax^{em}:362 nm) and ZnO (λmax^{ex}:376 nm, λmax^{em}:652 nm) recorded in powder form. 83

Figure 4.24 FTIR spectra of dried and heat treated combine ZnO-5Y_2O_3 86

Figure 4.25 XRD pattern of combine ZnO-5Y_2O_3 dried and heat treated gel 87

Figure 4.26 SEM micrographs of combine ZnO-Y_2O_3. 87

Figure 4.27 DTA-TG analysis of dried YAG xerogel powders 88

Figure 4.28 FTIR spectra of dried YAG 2 MRCM gel 89

Figure 4.29 XRD patterns of pure, 1% Eu and 1% Ce doped YAG 90

Figure 4.30 XRD pattern of composite ZnO-5YAG 90

Figure 4.31 Excitation and emission spectra of pure YAG between 200 and 500 nm 91

Figure 4.32 (a): Excitation and emission spectra Eu doped YAG (λ_{max}^{ex}:366 nm, λ_{max}^{em}:554 nm) (b): Excitation and emission spectra of Ce doped YAG between 200 and 450 nm 92

Figure 4.33 (a): Excitation and emission spectra Ce doped YAG (λ_{max}^{ex}:460 nm, λ_{max}^{em}:540 nm), (b) Excitation and emission spectra of Ce doped YAG between 200 and 500 nm. 93

Figure 4.34 Absorbance spectrum of MB solution versus irradiation time 94

Figure 4.35 Absorbance spectrum of MB solution versus irradiation time for pure Y_2O_3 95

Figure 4.36 Absorbance spectrum of MB solution versus irradiation time for pure YAG 95

Figure 4.37 Absorbance spectrum of MB solution versus irradiation time for pure ZnO 96

Figure 4.38 Absorbance spectrum of MB solution versus irradiation time for pure ZnO and composite ZnO-Y_2O_3 samples after (a) 30 min. and (b) 150 min. irradiation 97

Figure 4.39 Illustration ZnO-Y_2O_3 photocatalytic system 99

Figure 4.40 Absorbance spectrum of MB solution versus irradiation time for pure ZnO, composite ZnO-5Y_2O_3, and ZnO-5Y_2O_3 with different amount of Eu such 0.25%, 0.5%, 1% and 2% samples after (a) 30 and (b) 90 min. irradiation 100

Figure 4.41 Absorbance spectrum of MB solution versus irradiation time for pure ZnO and composite ZnO-5Y_2O_3, ZnO-5Y_2O_3 % 1 Eu, ZnO-5Y_2O_3 % 1 Ce samples after (a) 30 and (b) 90 min. irradiation 100

Figure 4.42 Absorbance spectrum of MB solution versus irradiation time for pure ZnO, composite ZnO-Y_2O_3 and combine ZnO-Y_2O_3 samples after (a) 30 min. and (b) 150 min. irradiation..... 101

Figure 4.43 Absorbance spectrum of MB solution versus irradiation time for pure ZnO and composite ZnO-5YAG, ZnO-5YAG % 1Eu, ZnO-5YAG % 1Ce samples after (a) 30 and (b) 90 min. irradiation 102

Figure 4.44 Relative concentration changes (C/C_0) of MB solutions 103

Figure 4.45 Photocatalytic degradation kinetic constant of ZnO photocatalysts 104

Figure 4.46 Photocatalytic degradation efficiency of pure ZnO and ZnO-Y_2O_3 composites photocatalysts 104

Figure 4.47 Stability and reusability study of ZnO-Y_2O_3 coposite photocatalyst powders in the MB degradation process under irradiation for five runs. 105

LIST OF TABLES

Page

Table 3.1 All chemicals used for the production of ZnO nanoparticles, Y_2O_3 and YAG powders 39

Table 3.2 MRCM ratios, pH values, amount of ethylene glycol for Y_2O_3 each solution 43

Table 3.3 Content of doped Y_2O_3 samples 47

Table 3.4 Content of doped and undoped YAG samples..... 50

Table 3.5 Recipe for pure, Eu doped, Ce doped YAG powders 50

Table 4.1 BET surface area of each sample prepared with different acid concentrations. 74

Table 4.2 Decay times of the composites prepared by the donor; Y_2O_3 and their blends including increasing amounts of the acceptor counterpart; ZnO. 84

Table 4.3 Photocatalytic degradation performances of pure ZnO, pure Y_2O_3, and ZnO-Y_2O_3 composites 105

Table 4.4 Comparison of the photocatalytic performance of composite ZnO-5Y_2O_3 with reported studies in the literature..... 106

CHAPTER ONE
INTRODUCTION

1.1 General

Nowadays, the utilization and contamination of natural resources are escalating rapidly due to the intensification of industrial activities, increasing global population, and surging energy demands. Particularly, the demand for water, a paramount natural resource, is incessantly rising while the availability of clean water sources is dwindling. In arid regions characterized by minimal rainfall and prolonged drought, water industries and governments encounter challenges in accessing suitable water resources, exacerbated by the effects of global warming. Researchers project that approximately 3.8 billion individuals worldwide lack adequate access to clean water, resulting in millions of fatalities due to waterborne diseases (Malato, Fernández-Ibáñez, Maldonado, Blanco & Gernjak, 2009). These statistical projections are anticipated to escalate in the near future, attributed to the excessive discharge of micro-pollutants into the natural water cycle (Richardson, 2010; Suárez, Carballa, Omil & Lema, 2008; Wintgens, Salehi, Hochstrat & Melin, 2008).

Water purification is essential for ensuring safe and clean potable water, industrial use, and environmental protection. Among the various treatment methods, photocatalytic degradation and complete removal techniques are two prominent approaches that target pollutants in water. Both methods aim to eliminate contaminants, but they differ in their mechanisms, effectiveness, and application (Burkhard, Deletic & Craig, 2000; Koe, Lee, Chong, Pang & Sim, 2020). The photocatalytic process is a degradation process**,** not necessarily removing the contaminants but breaking them down into simpler, less harmful compounds. Complete removal techniques focus on the removal or extraction of pollutants from water without breaking them down, often leaving the contaminants in a separate waste form (e.g., sludge or adsorbent material) (Burkhard et al., 2000; Koe et al., 2020). Photocatalysis is particularly effective at breaking down organic contaminants such as dyes, pharmaceuticals, pesticides, and industrial chemicals. The technique works well with persistent organic pollutants that are difficult to remove using traditional methods. However, photocatalysis may not be very effective against inorganic contaminants like

heavy metals or salts, as it mainly targets organic matter. Complete removal techniques are more versatile and capable of removing both organic and inorganic contaminants. For instance, filtration can remove particles and some microorganisms. Ion exchange can remove dissolved inorganic contaminants like heavy metals (e.g., lead, mercury). Adsorption can remove both organic compounds and metals depending on the material used (e.g., activated carbon for organic compounds). Some complete removal techniques, like ion exchange or reverse osmosis, can produce waste byproducts, such as spent resin or concentrated brine, which must be properly treated or disposed of. These techniques can be energy-intensive, especially when dealing with large volumes of water (Gaya & Abdullah, 2008; Yang & Cheng, 2007).

A myriad of techniques are deployed to convert polluted or waste water into a reusable state such as the use of ozone, hydrochloric acid, chlorine, sodium hydrooxide, ferric salt, ion exchange, coagulation, and filtration techniques. (Aieta, Berg, Roberts & Cooper, 1980; Gregory & Dhond, 1972; Jiang & Lloyd, 2002; Phasey, Vandamme & Fallowfield, 2017; Prazeres, Luz, Fernandes & Jerónimo, 2020; Rodríguez et al., 2008; Šostar-Turk, Petrinić & Simonič, 2005). The methods applied on the basis of adsorption and precipitation, which are industrially preferred, concentrate the existing pollutants by converting them to other phases, but they cannot be completely eliminated (Padmanabhan et al., 2006). Other traditional water treatment methods such as sedimentation, filtration, chemical and membrane technologies are not considered very attractive methods because of their high operating costs and they can create toxic secondary pollutants in the ecosystem (Gaya & Abdullah, 2008). These include the need for substantial engineering infrastructure, lengthy initial investment periods, significant energy requirements, and their reliance on complex chemical processes. Additionally, toxic residues that may result from the purification process can also lead to contamination of clean water sources. Although chlorination is the most widely used disinfection process, disinfection by-products resulting from chlorination are mutagenic and are known to have carcinogenic effects (Yang & Cheng, 2007).

The photocatalytic materials have important role in the protection of clean water resources and wastewater cleaning. Materials such as semiconductor zinc oxide (ZnO),

titanium oxide (TiO_2), iron oxide (Fe_2O_3), cadmium sulfide (CdS), gallium phosphide (GaP) and zinc sulfide (ZnS) that are activated by light are known as catalysis materials that are frequently employed in researches. The capacity of these catalysts to convert diverse organic pollutants into easily biodegradable compounds, subsequently mineralizing them into benign carbon dioxide and water, has garnered considerable attention as a promising area of research among scholars (Esplugas, Gimenez, Contreras, Pascual & Rodríguez, 2002; Pera-Titus, García-Molina, Baños, Giménez & Esplugas, 2004).

Among photocatalytic semiconductor materials, ZnO has been widely used in the application of photocatalytic processing to date on account of its versatile, inexpensive, non-toxic, unique electronic and optical properties (Bomila, Suresh & Srinivasan, 2019; Mohamed, Hammami, Akhtar & Youssef, 2019). ZnO possesses a band gap of 3.37 eV, forming electron-hole pairs under UV light. The binding energies of these electrons are 60 MeV at room temperature for ZnO (Lee, Lai, Ngai & Juan, 2016; Raji & Gopchandran, 2017; Tangcharoen, Klysubun & Kongmark, 2018). Methods such as wet chemical method, spray pyrolysis, precipitation method, thermal annealing, hydrothermal, and sol-gel method have been employed for ZnO production until today (Adam, Pozina, Willander & Nur, 2018; Baruah & Dutta, 2009; Dikici & Demirci, 2019; Hasnidawani et al., 2016; Li & Haneda, 2003; Shimpi et al., 2016). Among these methodologies, the sol-gel method has risen to prominence among researchers due to its exceptional control over the production process, precision in stoichiometry, repeatability, and straightforwardness in generating complex oxide particles (Farley et al., 2004; Luna-Arredondo et al., 2005). This approach enables the fabrication of high-purity and uniform oxides exhibiting diverse morphologies. Extensive literature is available, underscoring investigations focused on ZnO synthesized via the sol-gel technique, specifically for its application in the photocatalytic degradation of organic pollutants (Kilinc, Demirci, Uysal, Celik & Kurt, 2017; Mahdavi & Talesh, 2017). These studies delve into various parameters influencing the catalytic efficacy of ZnO, aiming to optimize the degradation process. Diverse strategies, including doping with specific elements, surface modifications, and composite material development, have been explored to enhance the catalytic capabilities of photocatalytic materials (Demirci et al., 2016; Hong et al., 2009; Lei et

al., 2015; Woan, Pyrgiotakis & Sigmund, 2009). Unlike prior efforts, our study is based on stimulating the photocatalytic material with a more efficient excitation to enhance its performance rather than altering the material itself. Consequently, rather than employing complex and costly modification techniques, catalytic performance has been enhanced through a simple, yet unique and highly effective mechanism. To improve the efficacy for excitation source-photocatalyst material interaction, using photoluminescent materials presents a viable strategy.

To effectively utilize photocatalytic materials, it is essential to introduce a suitable light source into the environment. When exposed to a light source, semiconductor photocatalytic materials become activated, facilitating the conversion of harmful organic pollutants in the environment into benign compounds (Esplugas et al., 2002; Pera-Titus et al., 2004). Without a light source, organic content's decomposition reaction cannot occur. Further degradation can be achieved by prolonging the interaction time or enhancing the interaction efficiency of the photocatalytic material with light. To optimize the interaction between the light source and photocatalytic materials, photoluminescent materials can be employed. Upon irradiation with light, these materials undergo excitation, entering a transient unstable state. Subsequently, as the irradiation ceases, photoluminescent materials emit radiation to return to a stable state (Dubey, Agrawal & Kaur, 2015; Gültekin et al., 2019; Rao, 1996). The emitted radiation may vary depending on the specific luminescent material employed. Notably, yttrium oxide (Y_2O_3) and yttrium aluminum garnet (YAG, $Y_3Al_5O_{12}$) phosphors are recognized for their exceptional luminescent properties and have been extensively studied across various fields. In research of semiconductor heterostructures, electronics in transistors, and superconducting ceramics in the ceramic industry, Y_2O_3 and YAG have attracted a lot of interest. Moreover, they have demonstrated remarkable performance as light-emitting materials (Chambers & Parsons, 2001; Fujita, Yoshihara, Sakamoto, Yamamoto & Tanabe, 2005; Konrad, Herr, Tidecks, Kummer & Samwer, 2001; Latynina et al., 2013; Regnier, Sapin & de Montpreville, 1989; Tzu, Chen & Hsu, 2021; Vetrone, Boyer, Capobianco, Speghini & Bettinelli, 2003).

In the literature, studies examining the photoluminescent and photocatalytic

properties of ZnO, Y_2O_3, and YAG are frequently encountered. However, there is a limited number of studies that utilize these two mechanisms in a complementary manner. While the notion of enhancing the photocatalytic mechanism through the influence of luminescence appears promising, research in this area is notably scarce. In our study, ZnO nanoparticles were employed as the photocatalyst, while pure, Eu and Ce doped Y_2O_3, as well as YAG, were synthesized via the sol-gel method for photoluminescence. Composite materials and pure ZnO with pure and doped Y_2O_3 and YAG, along with various weight percentages, were produced using simple and cost effective mechanical mixing and precipitation techniques. Morphological, structural, optical, and photocatalytic properties of ZnO, Y_2O_3, YAG, ZnO-Y_2O_3, and ZnO-YAG composite samples were thoroughly analyzed to elucidate the findings.

1.2 Organization of the Thesis

The objective of this study is to enhance the catalytic performance of photocatalytic materials through the incorporation of photoluminescent materials. The aim is to augment the efficiency and catalytic activity of photocatalytic materials using photoluminescent materials. Photoluminescent materials possess the ability to absorb light energy and subsequently emit light when the excitation source is removed, returning to their stable state. The duration of this emission varies depending on the type of photoluminescent material. In this thesis, we seek to leverage this characteristic of photoluminescent materials to enhance the efficiency of photocatalytic materials. Specifically, our focus is on composite materials combining photoluminescent and photocatalytic properties. ZnO has been selected as the photocatalytic material due to its noteworthy electrochemical, optical, and photocatalytic characteristics. As for the photoluminescent materials, Y_2O_3 and YAG were chosen for their favorable luminescent properties. Combining the advantages of these photoluminescent and photocatalytic materials holds promise for the development of advanced photocatalytic systems.

In the context provided, Chapter One presents theoretical insights concerning the research area and the specific objectives pursued within this thesis. The subsequent chapter, Chapter Two, delves into theoretical frameworks elucidating photocatalytic and photoluminescent phenomena, alongside discussions on corresponding materials,

composite oxide structures, and the sol-gel process. Chapter Three is dedicated to experimental works, encompassing studies on materials utilized in fabricating photocatalytic-photoluminescent composites, as well as the techniques employed for their production and characterization. Chapter Four, detailed observations derived from the optimization and production phases are presented, shedding light on the characteristics of the resulting products. Additionally, this chapter explores the influence of doping, and the presence of pure Y_2O_3 and YAG on the photocatalytic properties of ZnO. Finally, Chapter Five summarizes the thesis findings, drawing conclusions from the study and proposing future research directions.

CHAPTER TWO
THEORITICAL BACKGROUND

2.1 Photocatalysis

Photocatalysis is a light-driven process facilitated by a photocatalyst, which accelerates chemical reactions without undergoing permanent chemical changes. This process is gaining significant attention for its ability to address environmental and energy-related challenges, such as water purification, pollutant degradation, and hydrogen production through water splitting. The process relies on the interaction of light with a semiconductor, which generates reactive species that enable redox reactions (Fujishima & Honda, 1972; Hoffmann, Martin, Choi & Bahnemann, 1995).

Photocatalysis can be categorized into homogeneous and heterogeneous systems. Homogeneous photocatalysis occurs when the photocatalyst and the reactants are in the same phase, typically liquid. In contrast, heterogeneous photocatalysis involves a solid photocatalyst and liquid or gas-phase reactants, making it more versatile for practical applications.

2.1.1 Mechanism and Basic Principles of Photocatalysis

A photo-induced process that is accelerated in the presence of a catalyst is known as photocatalysis. For the electrons in the valence band to be activated and moved to the conduction band in semiconductors like ZnO, TiO_2, WO_3, and CdS, the energy of the radiation must be larger than or equal to the band gap energy. As a result, charge separation occurs by forming positively charged ions in the valence band (Carp, Huisman & Reller, 2004; Mills & Le Hunte, 1997). Photogenerated electrons produce $O_2 \cdot^-$ radicals when they react with electron acceptors like O_2 dissolved in water or adsorbed on the catalyst surface. To create $OH \cdot$ radicals, photogenerated holes react with OH^- or H_2O (Uduak G Akpan & Bassim H Hameed, 2009; Konstantinou & Albanis, 2004). By mediating charge transfer between the two adsorbed molecules, photocatalysts enhance the photocatalytic reaction, whereas active radicals decompose organic substances.

The photocatalyst, on the other hand, takes an electron from the medium or transfers the charge to the other substrate to return from the excited state to the unexcited state (Mohamed, McKinney & Sigmund, 2012). The more the photocatalyst can prevent or delay charge recombination, the more it provides an ideal environment for the catalysis reaction to continue (Van Gerven, Mul, Moulijn & Stankiewicz, 2007).

A photon with energy $E = h\vartheta$ (where h is Planck's constant and ϑ is the frequency of light) excites an electron from the valence band (VB) to the conduction band (CB) of a semiconductor, leaving a hole in the VB. The condition for this excitation is that the photon energy must be equal to or greater than the bandgap energy (E_g) of the semiconductor. Detailed mechanism of photocatalytic reactions are given below.

$$Photocatalyst + h\vartheta \rightarrow e^- + h^+ \qquad \text{Eq. (2.1)}$$

After the creation of the electron-hole pairs, these charge carriers can either recombine (which would result in energy loss and no further reaction) or migrate to the surface of the catalyst, where they participate in chemical reactions. To enhance photocatalytic efficiency, the recombination rate must be minimized by optimizing the semiconductor material and experimental conditions (Van Gerven et al., 2007).

Electrons in the CB and holes in the VB participate in reduction and oxidation reactions, respectively, with adsorbed molecules on the photocatalyst surface. Both oxidation and reduction can occur on the surface of the photo excited semiconductor photocatalyst (Fujishima & Honda, 1972; Gurylev, 2021).

$$e^- + O_2 \rightarrow O_2 \cdot^- \qquad \text{Eq. (2.2)}$$

$$h^+ + H_2O \rightarrow H^+ + OH \cdot \qquad \text{Eq. (2.3)}$$

$$H_2O \rightarrow H^+ + OH^- \qquad \text{Eq. (2.4)}$$

$$O_2 \cdot^- + H^+ \rightarrow HOO \cdot \qquad \text{Eq. (2.5)}$$

The reduction time of the photogenerated hole can be prolonged due to the inhibitory ability of the hydroprexyl radical $HOO\cdot$, just like O_2 does.

$$HOO \cdot + e^- \rightarrow HOO^- \qquad \text{Eq. (2.6)}$$

$$HOO^- + H^+ + e^- \rightarrow H_2O_2 \quad \text{Eq. (2.7)}$$

If the oxygen is insufficient to inhibit the electrons to form superoxides ($O_2 \cdot^-$), it then forms hydroperoxyl radicals ($HOO \cdot$) and H_2O_2. The resulting $OH \cdot$ radicals oxidize the organic compounds and produce H_2O and CO_2, which are the products of the catalysis reaction (L. V. Trandafilović, D. J. Jovanović, X. Zhang, S. Ptasińska & M. D. Dramićanin, 2017; Wen, Ding & Shan, 2011; Yu, Xiong, Cheng & Liu, 2005);.

$$OH \cdot + organic\ compound \rightarrow CO_2 + H_2O \quad \text{Eq. (2.8)}$$

2.1.2 Types of Photocatalytic Materials

Photocatalytic materials, with their ability to catalyze reactions under light irradiation, are the cornerstone of many emerging technologies for sustainable energy production and environmental remediation. Several example of these materials, such as zinc oxide (ZnO), titanium dioxide (TiO_2), molybdenum oxide (MoO_3), tungsten trioxide (WO_3), and quantum dots (QDs), graphitic carbon nitride (g-C_3N_4) exhibit unique properties that make them suitable for different photocatalytic applications.

2.1.2.1 ZnO

ZnO has emerged as a prominent semiconductor material with diverse applications owing to its unique electronic and optical properties. In its pure form, ZnO is a semiconductor with both n-type and p-type conductivity. The conductivity can be modulated through doping with elements such as Al, Ga, or In (Bhosle, Tiwari & Narayan, 2006; Hong, Katsumata & Matsushita, 2016; Ilican, Caglar, Caglar & Yakuphanoglu, 2006; Singh, Chaudhary & Pandya, 2016).

ZnO exhibits distinct crystal structures, typically adopting the rocksalt, wurtzite, or cubic (zinc blende) arrangement. Figure 2.1 depicts the crystal structure of ZnO. While ZnO can transform into a rocksalt structure under high pressure, occurrences of ZnO in this configuration are uncommon. Among these structures, the wurtzite form stands out as the most thermodynamically stable, making it the prevalent and widely observed crystal structure for ZnO (Özgür et al., 2005; Zhong Lin, 2004). Its lattice constants are a = 3.25 Å, c = 5.21 Å and density approximately 5.61 g/cm³. The melting point of ZnO is around 1974 °C (3585 °F) (Lee, Sorescu & Deng, 2016).

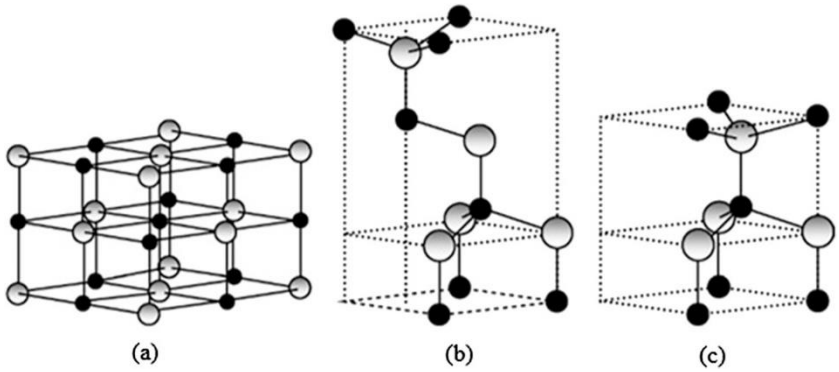


Figure 2.1 The (a) rocksalt (cubic), (b) zinc blende (cubic) and (c) wurtzite (hexagonal) structures model of ZnO (Kian Mun Lee et al., 2016)

ZnO's wurtzite crystal structure influences its electronic properties, making it suitable for various electronic devices. It possesses both n-type and p-type conductivity, and these properties are controlled through intentional doping with various impurities. This flexibility in electronic characteristics enhances its utility in the development of electronic components (Harun, Salleh, Deghfel, Yaakob & Mohamad, 2020).

ZnO is utilized as a UV filter in sunscreens owing to its capacity to absorb and scatter UV radiation. Additionally, it finds application in gas sensors, detecting diverse gases through changes in electrical conductivity. Moreover, ZnO is employed in solar cells, facilitating the advancement of efficient and cost-effective photovoltaic devices. Furthermore, it exhibits antibacterial properties and is employed in various applications such as medical textiles and wound dressings (Fouda, El-Din Hassan, Salem & Shaheen, 2018; Giancaterini et al., 2015; Luo, Wang & Zhang, 2018; Porrawatkul, Nuengmatcha, Kuyyogsuy, Pimsen & Rattanaburi, 2023; Talebian, Amininezhad & Doudi, 2013; Vittal & Ho, 2017).

ZnO's exceptional photocatalytic activity, particularly under UV light, has gained significant attention. When exposed to light, ZnO generates electron-hole pairs, initiating redox reactions. These reactions play a crucial role in the degradation of organic pollutants, highlighting their potential for environmental applications (Chen, Wu, Liu & Gao, 2017; Demirci, Dikici, Tünçay & Kaya, 2020; Machrouhi et al., 2023; Qi, Cheng, Yu & Ho, 2017; Silva et al., 2024). The schematic diagram of photocatalytic degradation mechanism is given in Figure 2.2.

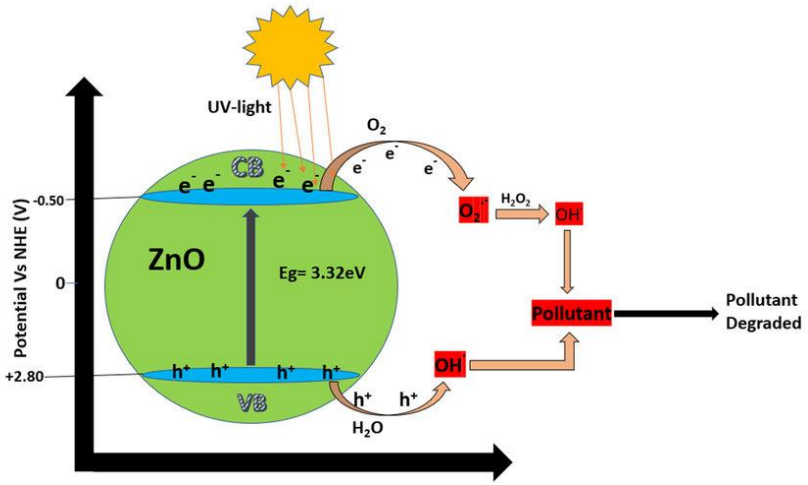


Figure 2.2 Schematic illustration of the photocatalytic mechanism of ZnO (Yaqoob, Mohd Noor, Serrà & Mohamad Ibrahim, 2020)

This compound, with a bandgap of 3.37 eV and excitation binding energy of 60 meV at room temperature, exhibits a wurtzite crystal structure, impacting its physical and chemical characteristics (Kian Mun Lee et al., 2016; Raji & Gopchandran, 2017; Tangcharoen et al., 2018). The bandgap energy of ZnO determines the wavelength of light it can absorb. Strategies to tailor the bandgap energy are explored to optimize light absorption in the visible spectrum, broadening its photocatalytic applicability. Bridging the gap between laboratory-scale studies and scalable production for practical applications remains a focus for researchers and industry (Sun et al., 2023). Efforts are ongoing to modify ZnO to extend its absorption into the visible light range for improved photocatalytic efficiency. However in our study, a different approach was followed to increase the effectiveness of ZnO. Instead of increasing the absorption ability of ZnO, ways to expose it to more light in an effective and inexpensive way have been sought. For this purpose we use photoluminescent materials.

2.1.2.2 TiO_2

TiO_2 is one of the most widely studied photocatalysts, just like ZnO, due to its non-toxic nature, high chemical stability, and excellent photocatalytic performance, particularly in the degradation of organic pollutants. TiO_2 exists primarily in three polymorphic forms: anatase, rutile, and brookite, with anatase being the most efficient photocatalyst due to its higher surface area and better charge separation properties

(Chen et al., 2020). Rutile, although more thermodynamically stable, shows lower photocatalytic efficiency compared to anatase due to slower electron-hole recombination rates (Li, Wang, Wu & Zhou, 2022).

TiO_2 operates mainly under UV light, as its band gap (~3.2 eV for anatase) is too large for visible light absorption. However, doping with metals (e.g., silver) or non-metals (e.g., nitrogen) can shift its absorption spectrum (Dong et al., 2015; Li et al., 2022).

2.1.2.3 MoO_3

MoO_3 has attracted attention as a photocatalyst due to its moderate band gap (~2.8 eV), allowing it to harness visible light for photocatalytic processes. MoO_3 possesses a layered orthorhombic structure that facilitates the migration of charge carriers, which is crucial for photocatalytic activity (Afridha, Prakash & Roopan, 2025). However, its photocatalytic efficiency is limited by poor charge separation and rapid recombination of photoinduced electrons and holes. Combining MoO_3 with other semiconductors, such as TiO_2 or graphene, can significantly enhance its photocatalytic properties by improving charge transfer and reducing recombination (Afridha et al., 2025; da Silva Júnior et al., 2023). It's active in both oxidation and reduction reactions, particularly in CO_2 reduction.

2.1.2.4 WO_3

WO_3 is another semiconductor material with a monoclinic crystal structure that shows promise in photocatalytic applications, especially in the fields of water splitting and CO_2 reduction. With a band gap of approximately 2.6 eV, WO_3 is capable of absorbing visible light and catalyzing oxidation reactions, making it highly effective for the degradation of organic pollutants and the production of hydrogen (Mohd Razali et al., 2021). It has good activity for oxidation reactions in water splitting and pollutant degradation. However, WO_3 suffers from relatively poor charge separation and slow reaction kinetics. To address this, doping with elements like Nb or Cr and combining WO_3 with other semiconductors has been shown to improve its photocatalytic efficiency (Gu et al., 2024; Mohd Razali et al., 2021).

2.1.2.5 Quantum Dots

Quantum dots (QDs) are nanoscale semiconductor particles that display exceptional optical and electronic properties, which arise from the phenomenon of quantum confinement.. They have a tunable band gap, which allows for a wide range of photocatalytic applications under visible light, depending on the size and composition of the QDs. QDs are advantageous for photocatalysis due to their high surface-to-volume ratio, which facilitates enhanced adsorption and reaction rates. Moreover, QDs can be engineered to have superior charge carrier dynamics, improving their photocatalytic performance. However, their high surface energy and tendency to undergo photoinduced degradation limit their long-term stability and scalability for commercial applications. Furthermore, the synthesis of QDs is often complex and expensive, limiting their practical use.(Anil Kumar et al., 2023; Bajorowicz et al., 2018; Hoang, Dave & Gomes, 2019; Pirsaheb, Asadi, Sillanpää & Farhadian, 2018)

2.1.2.6 g-C_3N_4

Graphitic Carbon Nitride (g-C_3N_4) has emerged as a promising photocatalytic material due to its unique properties, such as visible-light absorption, chemical stability, and high photocatalytic activity for various applications, including water splitting, CO_2 reduction, and pollutant degradation. g-C_3N_4 is a non-metallic photocatalyst with a graphitic-like structure that enables it to efficiently absorb visible light and generate photoinduced charge carriers. Its simple synthesis, low cost, and environmentally friendly nature make it a highly attractive material for photocatalysis (Lin, Pan & Wang, 2014; Niu et al., 2021; Yang et al., 2020).

g-C_3N_4 operates primarily under visible light due to its moderate band gap (~2.7 eV), which allows it to harness a significant portion of the solar spectrum for photocatalytic processes. However, its charge carrier separation efficiency remains a challenge. In g-C_3N_4, the photogenerated electrons and holes often recombine quickly, reducing the photocatalytic efficiency. To address this, several strategies have been explored, including doping (e.g., with metal or non-metal elements), coupling with other semiconductors, and structuring g-C_3N_4 at the nanoscale to improve charge

separation and surface reactivity (Ismael, 2020; Jiang et al., 2017; Tian, Huang, Du, Dong & Zhang, 2019; Wang et al., 2020).

2.1.3 Photocatalytic Processes

2.1.3.1 Water splitting

Water splitting, the process of converting water into hydrogen and oxygen using solar energy, is a crucial area of photocatalysis due to its potential for hydrogen production, a clean energy carrier. The ideal photocatalyst for water splitting must possess several key properties, including a suitable band gap, high charge carrier mobility, and stability under reaction conditions. Materials like TiO_2, ZnO and WO_3 have been extensively investigated for water splitting applications (Fajrina & Tahir, 2019). ZnO, for example, has demonstrated the ability to produce hydrogen from water under UV light, but its large band gap limits its efficiency under natural sunlight. The development of hybrid photocatalysts, such as ZnO coupled with graphene or carbon-based materials, has shown promise in enhancing the photocatalytic performance by improving charge carrier separation and extending light absorption into the visible spectrum (Raizada, Sudhaik & Singh, 2019; Xu, Zhang, Cheng & Zhu, 2011). Moreover, quantum dots (QDs) have been increasingly used in water splitting due to their tunable band gap and high efficiency under visible light (Jin, Zhao, Wang & Rosei, 2021; Juan Liu et al., 2014)

The overall water splitting reaction can be described as (Graham & Hammer, 2012):

$$2H_2O + h\vartheta \rightarrow 2H_2 + O_2 \qquad \text{(Eq. 2.9)}$$

The reaction involves two half-reactions:

Anode reaction (oxidation):

$$2H_2O \rightarrow O_2 + 4H^+ + 4\ e^- \qquad \text{(Eq. 2.10)}$$

Cathode reaction (reduction):

$$4H^+ + 4\ e^- \rightarrow 2H_2 \qquad \text{(Eq. 2.11)}$$

2.1.3.2 Waste water treatment

In wastewater treatment, photocatalytic materials are used to degrade harmful organic pollutants and pathogens. The photocatalytic degradation involves the generation of reactive oxygen species (ROS), such as hydroxyl radicals (OH·), which can oxidize and break down organic contaminants. TiO_2 and ZnO are the most common photocatalysts for wastewater treatment due to their high efficiency in generating ROS under UV light.

The general photocatalytic degradation reaction is as follows:

$$Organic\ pollutant\ + O_2 + h\vartheta \rightarrow Degredation\ product \quad \text{(Eq. 2.12)}$$

For example, ZnO generates hydroxyl radicals under UV light, which can oxidize pollutants like phenols, dyes, and pesticides into less harmful substances (Dong et al., 2015; Ong, Ng & Mohammad, 2018)

$$C_6H_5OH + 4O_2 + h\vartheta \rightarrow 6CO_2 + 3H_2O \quad \text{(Eq. 2.13)}$$

However, the efficiency of this process can be limited by factors such as low light absorption, inefficient charge transfer, and the potential for photocatalyst deactivation due to the deposition of pollutants on the catalyst surface. The incorporation of metal dopants, like Ag or Cu, has been shown to improve the photocatalytic performance by enhancing light absorption and charge carrier separation (Hosseini, Sarsari, Kameli & Salamati, 2015; Mohan, Krishnamoorthy & Kim, 2012).

2.1.3.3 Air purification

Photocatalytic materials also play a significant role in air purification by breaking down toxic gases like NOx, CO_2, and volatile organic compounds (VOCs). WO_3 and TiO_2 have been extensively studied for their ability to catalyze the oxidation of NOx, with TiO_2 showing superior performance due to its high surface area and stability under UV light (Balayeva, Fleisch & Bahnemann, 2018). Additionally, recent studies have focused on the development of hybrid photocatalysts that combine metal oxide semiconductors with carbon-based materials like graphene to enhance the photocatalytic degradation of VOCs under visible light (Pham et al., 2021). Quantum

dots, due to their tunable band gap, also show promise for air purification applications, particularly in indoor environments where visible light is more prevalent (Jing, Zhao, Sun, Zhong & Peng, 2019; Pham et al., 2021)

2.1.3.4 CO_2 reduction

Photocatalytic CO_2 reduction is a process where CO_2 is converted into valuable chemicals, such as methane (CH_4) or methanol (CH_3OH), using solar energy (Fang et al., 2023). Photocatalysts like TiO_2, and WO_3 are commonly used for CO_2 reduction under UV or visible light. The process involves the reduction of CO_2 molecules using photoinduced electrons generated by the photocatalyst (Habisreutinger, Schmidt-Mende & Stolarczyk, 2013).

The general reaction for CO_2 reduction is:

$$CO_2 + H_2O + 4\,e^- + h\vartheta \rightarrow CH_4 + 2O_2$$

WO_3, due to its visible-light absorption, is particularly effective for CO_2 reduction, and recent studies have shown that coupling WO_3 with carbon-based materials enhances its performance (Ohno, Murakami, Koyanagi & Yang, 2014)(Nguyen et al., 2019). Quantum dots have also been explored for CO_2 reduction due to their tunable band gaps and efficient charge separation, which help convert CO_2 into useful hydrocarbons under visible light (Wu, Li, Tung & Wu, 2019) .

2.1.4 Improving Photocatalytic properties

The efficiency of photocatalysis is determined by several factors, including the ability of the photocatalyst to absorb light, generate charge carriers, prevent recombination, and interact with reactants effectively. To enhance photocatalytic efficiency, various strategies have been developed to address these challenges. The following approaches are widely employed to improve the overall performance of photocatalytic systems.

2.1.4.1 *Band gap modulation*

The band gap of a semiconductor material is crucial in determining its photon absorption capability. Photocatalysts with narrow band gaps can absorb a broader

range of the solar spectrum, including visible light. Materials like ZnO with a band gap of approximately 3.3 eV, are typically restricted to absorbing only ultraviolet (UV) light, which accounts for only a small portion of the solar spectrum (Kamarulzaman, Kasim & Rusdi, 2015).To improve the photon absorption properties, several strategies are employed.

Doping the semiconductor with metal or non-metal elements is a common method to change the band gap. For example, nitrogen doping in TiO_2 lowers its band gap and extends its absorption into the visible region. Similarly, sulfur or carbon doping can achieve similar effects (Asahi, Morikawa, Ohwaki, Aoki & Taga, 2001). Co-doping combines different elements to further optimize the photocatalytic performance. For example, co-doping ZnO with nitrogen and sulfur has been shown to improve photocatalytic activity by reducing recombination rates and enhancing absorption under visible light (Farhadian et al., 2019).

Creating heterojunctions by combining semiconductors with different band gaps can significantly improve charge separation and enhance light absorption. For instance, a combination of ZnO and MoS_2 or CeO_2 forms a Z-scheme photocatalytic system that enhances photocatalytic efficiency by facilitating electron transfer between the two materials (Fu et al., 2021; Zhu, Li, Xia, Liu & Xiong, 2018).

2.1.4.2 Surface area and morphology Optimization

The surface area of a photocatalyst directly influences its efficiency by providing more active sites for the adsorption of reactants and the formation of charge carriers. Materials with a larger surface area allow for more efficient interactions between the catalyst and the reactants.

Nanostructuring materials into nanofibers, nanoparticles, or nanosheets significantly enhance the surface area and the diffusion of reactants. Photocatalysts with larger surface areas are more effective at adsorbing reactants and providing more sites for charge separation. For example, TiO_2 nanotubes exhibit higher photocatalytic activity due to their increased surface area and improved charge carrier mobility (Adán, Marugán, Sánchez, Pablos & van Grieken, 2016; Lai et al., 2006).

Creating porous structures can also enhance photocatalytic efficiency. Porosity improves the diffusion of reactants to the active sites, leading to higher reaction rates. Materials like mesoporous ZnO have been shown to improve the degradation of pollutants by enhancing reactant accessibility, ratio of surface defect to bulk material and facilitating charge transport (Di Liu et al., 2014)

2.1.4.3 Co-catalysts

The use of co-catalysts such as platinum, gold, or silver can enhance photocatalytic efficiency by facilitating charge carrier separation and promoting faster reaction rates. These co-catalysts act as electron sinks, helping to prevent recombination. The introduction of co-catalysts and dopants into the photocatalytic system can significantly enhance the separation of electron-hole pairs and promote surface reactions. They also facilitate charge transfer, making them particularly useful in reactions like water splitting or pollutant degradation. (Gao, Liu & Sun, 2013; Silva et al., 2014; Zhai et al., 2013). For example, Platinum/TiO_2 composites exhibit enhanced hydrogen production efficiency due to the ability of Platinum to reduce electron-hole recombination (Núñez et al., 2016).

2.1.4.4 Photocatalytic composite materials

The formation of composite materials by combining photocatalysts with other functional materials, such as carbon-based materials (graphene, carbon nanotubes carbon dots) or polymers, can enhance photocatalytic performance by improving charge carrier transport and extending the absorption spectrum. The incorporation of graphene enhances electron mobility, preventing recombination and improving the overall photocatalytic efficiency (Di Mauro et al., 2017; Fan et al., 2012; Fu, Guo, Pan, Huang & Wang, 2019; Jiang & Gao, 2005; Mochane, Motloung, Mokhena & Mofokeng, 2022; Siahsahlan, Aref, Naghshara & Azmayesh, 2024; Xue & Zou, 2018).

Graphene, with its high electrical conductivity and large surface area, can be used to create composites with photocatalysts. The incorporation of graphene enhances electron mobility, preventing recombination and improving the overall photocatalytic efficiency. For example, the coupling of ZnO with graphene has shown enhanced

photocatalytic activity for various applications, including dye degradation and hydrogen production (Fan et al., 2012; Siahsahlan et al., 2024).

2.1.4.5 Reaction condition and light source

Optimizing reaction conditions such as temperature, pH, and light the intensity and wavelength of the light source can also improve photocatalytic performance (Bayarri, Abellán, Giménez & Esplugas, 2007; Chen & Hsu, 2021; Kazeminezhad & Sadollahkhani, 2016; Mohamadpour & Amani, 2024).

The choice of light source is crucial for optimizing the energy input into the system. UV light is typically used for semiconductor materials like ZnO, but visible light-active photocatalysts such as g-C_3N_4 are being developed for broader solar utilization because they enable the utilization of solar energy more efficiently. For optimal performance, the photocatalyst must be tuned to absorb the appropriate wavelengths of light. (Iqbal & Liu, 2024; Nasir et al., 2013; Saleh & Djaja, 2014; Samadi, Zirak, Naseri, Khorashadizade & Moshfegh, 2016; Soni, Teli, Teli & Agarwal, 2024).

2.1.5 Parameters Affecting Photocatalytic Performance

The photocatalytic performance of a system is highly dependent on several factors, ranging from the properties of the photocatalyst material to the experimental conditions. Optimizing these parameters is essential to maximize photocatalytic efficiency.

2.1.5.1 Semiconductor materials

The type of semiconductor used plays a critical role in the photocatalytic process. The ideal photocatalyst should have a suitable band gap, high surface area, and good stability under light exposure.

Photocatalysts with narrower band gaps, such as those in the range of 1.5 to 3 eV, are better suited for solar light utilization. For instance, ZnO and TiO_2 have a wide band gap (~3.3 and ~3.2 eV), which limits its efficiency to UV light. However, doping or coupling them with other materials like g-C_3N_4 or CdS can extend the absorption

spectrum into the visible range, making it more efficient under sunlight (Boonprakob et al., 2014; Fereidooni et al., 2024; Huo et al., 2016; Meng et al., 2012).

2.1.5.2 Light intensity and wavelength

Light intensity directly impacts the generation of charge carriers in photocatalysis. Higher light intensity increases the number of photons hitting the photocatalyst, leading to more electron-hole pairs and faster reactions. The rate of the reaction can be described by:

$$r = \Phi . \eta . I$$

where r is the reaction rate, Φ is the quantum efficiency, η is the charge separation efficiency, and I is the light intensity. However, at very high intensities, the rate may plateau due to saturation of active sites or increased recombination of charge carriers, which limits further gains (Benabbou, Derriche, Felix, Lejeune & Guillard, 2007; Serpone, 1997; Yang & Liu, 2007).

The wavelength of light determines which photons can excite the photocatalyst. Photons with energy higher than the bandgap of the photocatalyst will generate electron-hole pairs. The energy of a photon is inversely related to its wavelength:

$$E = \frac{hc}{\lambda}$$

Where h is Planck's constant, c is the speed of light, and λ is the wavelength (Jose, Vincent, Lilly & Lazar, 2019). The wavelength of the light must match the absorption spectrum of the photocatalyst. If the light source emits wavelengths outside the absorption range of the photocatalyst, the efficiency of the process will decrease. TiO_2 or ZnO absorbs UV light, so it performs better under UV illumination, but visible-light-active materials like g-C_3N_4 are better suited for solar energy harvesting (Djurišić, He & Ng, 2020).

In practical applications, UV light is effective for many photocatalysts, but visible-light-activated photocatalysts are preferable for large-scale, solar-driven processes. Optimizing light intensity and wavelength based on the photocatalyst's absorption properties is essential for improving photocatalytic efficiency.

2.1.5.3 Concentration of reactants

The concentration of reactants plays a key role in determining the rate of photocatalytic reactions. Reactant concentration affects both the adsorption of molecules onto the photocatalyst surface and the overall reaction rate.

At low concentrations, the reaction rate typically increases with the concentration of the reactant. In this regime, the reaction follows first-order kinetics, where the rate is directly proportional to the concentration. At high concentrations**,** the photocatalyst surface can become saturated, and the reaction rate plateaus. This is because the active sites on the photocatalyst are fully occupied, leading to zero-order kinetics. The concentration of reactants influences the adsorption process. At low concentrations, reactants are efficiently adsorbed onto the photocatalyst surface, enhancing the reaction rate. However, at higher concentrations, the surface may become saturated, reducing the rate of adsorption. The Langmuir adsorption model describes this relationship:

$$\theta = \frac{K[C]}{1 + K[C]}$$

Where θ is the fractional coverage of the photocatalyst surface, and K is the adsorption constant. At higher concentrations, the surface is fully covered, and increasing the concentration no longer significantly improves the rate (Hanaor, Ghadiri, Chrzanowski & Gan, 2014; Zhang & Jaroniec, 2020).

At high reactant concentrations, diffusion limitations can occur. As the concentration increases, the rate of diffusion of reactants to the catalyst surface decreases, slowing down the overall reaction rate. This can lead to a situation where the reaction is no longer limited by the concentration of reactants but by the rate of diffusion (Ballari, Brandi, Alfano & Cassano, 2008). For practical considerations at low concentrations, high surface area catalysts (e.g., nanoparticles) are effective for maximizing reaction rates. At high concentrations, factors such as diffusion and surface saturation become more important. Here, photocatalysts with larger surface areas or those designed to improve diffusion (e.g., porous structures) may be more efficient.

2.1.5.4 pH of the solution

The pH of the solution significantly impacts photocatalytic reactions by affecting both the surface properties of the photocatalyst and the behavior of reactants.

The surface charge of photocatalysts depends on the pH of the solution. At low pH, the surface becomes positively charged, favoring the adsorption of anionic species, while at high pH, it becomes negatively charged, favoring cationic species. This influences the efficiency of pollutant degradation, as different pollutants are more easily adsorbed depending on the pH (Degen & Kosec, 2000; Zhao et al., 2020).

The ionization of reactants, such as organic pollutants or dyes, is pH-dependent. For example, phenol is more reactive in basic conditions, while many dyes are better degraded in acidic or neutral conditions. Optimizing pH enhances the interaction between the photocatalyst and the reactant, improving the degradation rate (U. G. Akpan & B. H. Hameed, 2009).

The pH affects the redox behavior of photogenerated charge carriers. In acidic solutions, protonation can enhance the generation of reactive oxygen species (·OH), improving oxidation reactions. In alkaline conditions, the photogenerated electrons promote hydrogen production in water splitting. Extreme pH levels can increase charge recombination, reducing efficiency (Karimi Estahbanati, Mahinpey, Feilizadeh, Attar & Iliuta, 2019).

For practical applications, the pH is adjusted slightly acidic to optimize adsorption and degradation in pollutant degradation. A slightly alkaline pH is preferred for efficient hydrogen generation in water splitting. For CO_2 reduction, alkaline conditions favor the conversion of CO_2 into useful fuels (Karimi Estahbanati et al., 2019; Kazeminezhad & Sadollahkhani, 2016).

2.1.5.5 Temperature

Although photocatalysis is primarily driven by light, the temperature of the reaction medium can influence the rate of reaction. Higher temperatures increase the kinetic energy of molecules, leading to faster diffusion of reactants to the photocatalyst surface and a higher reaction rate. This is particularly beneficial in processes where

reactant diffusion is a limiting factor. Temperature also affects charge carrier dynamics. Increased temperature enhances the mobility of electrons and holes, improving photocatalytic efficiency. However**,** excessive temperatures can lead to higher recombination rates of these charge carriers, reducing efficiency. At very high temperatures, there may be a risk of catalyst degradation or changes in the photocatalyst structure, which can negatively affect performance (Chen & Hsu, 2021; Meng et al., 2018; Velázquez et al., 2017).

2.2 Luminescence

Luminescence is a term used to describe the conversion of a certain type of energy into light which is different than thermal radiation. The term luminescence is defined as the spontaneous emission of light as a result of the excitation of a non-hot material with an external energy source. This phenomenon is distinct from incandescence, as luminescence occurs without the involvement of heat. It is a broad and diverse category of light emission processes, encompassing a variety of mechanisms through which electronic or atomic systems relax from an excited state to a lower energy state. These processes are fundamental to a wide array of applications, including spectroscopy, imaging, material science, and quantum computing, as well as biological and medical fields (Valeur & Berberan-Santos, 2011; Wu, Pan, Chen & Liu, 2017).

The study of luminescence provides insight into the electronic and structural properties of materials, as the light emitted can be directly related to the nature of the energy states within the substance. These processes can be classified into several types based on the mechanisms of energy absorption and emission, including photoluminescence, chemiluminescence, triboluminescence, thermoluminescence, cathodolumiescence and electroluminescence (Campbell, 1988; Shionoya, Yen & Yamamoto, 2018; Yacobi & Holt, 1986; Zink, Hardy & Sutton, 1976). Following sections will specifically focus on photoluminescence.

2.2.1 Mechanism of Luminescence

The underlying mechanism of luminescence involves the excitation of electrons within a material due to the absorption of external energy. Upon absorption, electrons are promoted from a lower energy state, typically the ground state, to higher energy

levels, creating an excited state. This excited state is typically unstable, and the system will return to a lower energy configuration by releasing energy in the form of electromagnetic radiation. This process of energy release is what gives rise to luminescence (Valeur & Berberan-Santos, 2011; Wu et al., 2017).

The emission process generally follows two key stages: excitation and relaxation. In the excitation phase, a substance absorbs energy (e.g., photons from an external light source) that causes an electron to be excited to a higher energy state. After excitation, the system undergoes a relaxation phase where the electron typically loses energy in the form of non-radiative processes, such as phonon interactions or electron-electron scattering, before eventually returning to a lower energy state. It is during this final step that the excess energy is emitted as light, and the wavelength of this emitted light is determined by the energy gap between the excited state and the final relaxed state (Valeur & Berberan-Santos, 2011; Wu et al., 2017).

The nature of the emitted light depends on the material in question, as well as the specific mechanisms governing electron transitions. These transitions can be influenced by various factors, including the electronic structure of the material, the temperature, and the surrounding environment. Additionally, the presence of impurities or defects within the material can alter the emission characteristics, a factor that is particularly important in the context of semiconductors and luminescent materials (Valeur & Berberan-Santos, 2011; Wu et al., 2017).

2.2.2 Photoluminescence

Photoluminescence (PL) refers to a subset of luminescence where the emission of light occurs after the absorption of photons. In this process, materials absorb electromagnetic radiation, promoting electrons from the valence band to the conduction band in semiconductors or from molecular orbitals in organic materials. The excited electrons then relax to lower energy states, releasing energy in the form of light. Photoluminescence is particularly significant in semiconductors, insulators, and organic materials, as it provides valuable insight into the electronic structure and optical properties of these substances (Liqiang et al., 2006; Shinde, Dhoble, Swart & Park, 2012).

PL is widely used to study the electronic properties of materials, especially in the characterization of semiconductors, quantum dots, and thin-film solar cells The efficiency and characteristics of photoluminescence depend on several factors, including the intrinsic electronic structure of the material, the presence of defects, impurities, or dopants, and the temperature at which the material is measured (Dean, 1982; Durose et al., 2004; Lie, Duerdin, Tuite, Houlton & Horrocks, 2002; Martín-García, Paulo, Costa & Velázquez, 2013; Wang, Mandelis, Sun, Li & Gao, 2018)

The emission spectrum of photoluminescence is typically characterized by a peak that corresponds to the energy difference between the initial excited state and the final relaxed state. Additionally, the decay time of the PL emission can be used to study the dynamics of charge carriers and their interactions with the material (Mokari (Empedocles, Neuhauser, Shimizu & Bawendi, 1999)

Another name for inorganic luminescent materials is phosphorus. Phosphorus is a word derived from the Greek and is formed from the combination of the words phos and phoros. In Greek, phos means light and phoros means bearer. Phosphorus prepared by the Japanese for the first time in the 10th century was formed from seashells. The first use of the word "phosphorus" took place 600 years later, after a scientist named Vincentinus Casciarolo in Bologna fired a stone, probably $BaSO_4$. Casciarolo discovered that this material, exposed to sun light during the day, emits a red light at night. (Virk, 2015)

Discovered by the young French chemist Thedore Sidot, ZnS is the prototype of the catod ray tube used in modern television. It seems that the discovery of ZnS in 1866 marked the beginning of scientific studies and synthesis of phosphorus (Shionoya et al., 2018).

Some photoluminescent powders, which are synthesized in our laboratory, are indicated in Figure 2.3. The powders are excited by UV light and emit at different wavelengths. There is a special type of luminescence that has a very slow decay, with the emission continuing for minutes or hours. This type of luminescence is called long lasting or persistent luminescence and it is commonly used in safety and exit marking.

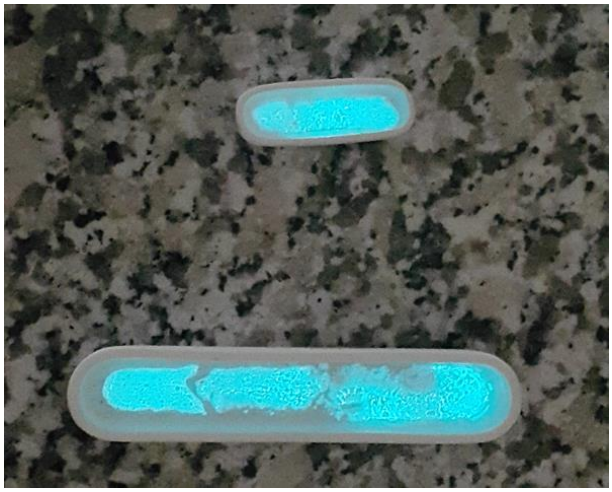


Figure 2.3 Example of persistent phosphors synthesized in our laboratory

2.2.2.1 Fluorescence and Phosphorescence

Photoluminescence can be classified into two types in itself. Fluorescence and phosphorescence are two primary types of photoluminescence that differ in their emission mechanisms and temporal characteristics. Both phenomena involve the absorption of photons followed by the emission of light, but the processes differ in terms of the electron transitions involved and the duration of the emitted light. The main difference between these two types of luminescence is the emission time of the material after the excitation light source has been eliminated. Fluorescence is characterized by the rapid emission of light following excitation. After a material absorbs a photon, the excited electron typically relaxes to a lower energy state almost immediately, emitting a photon in the process. The emitted photon has a longer wavelength (lower energy) than the absorbed photon, a phenomenon known as Stokes shift (Limpouchová & Procházka, 2016). The fluorescence terminates in nanosecond (10^{-9} to 10^{-8}) after the excitation light source cut-off. Therefore, fluorescence type luminescence can also be called short-live luminescence (Valeur & Berberan-Santos, 2011; Wu et al., 2017).

Fluorescence and phosphorescence can be understood by examining the concept of electron spin and the differences between singlet and triplet states. At the heart of this lies the Pauli Exclusion Principle, which dictates that no two electrons in an atom can share the same set of quantum numbers. As a result, two electrons can occupy a single

orbital, but they must have opposite spins. This is known as spin pairing (Kaplan, 2017; O'Hara & Kovács, 2022). Because of spin pairing, most molecules are diamagnetic, meaning they do not generate a magnetic field. These molecules' electrons are unaffected by static electric fields, neither drawn to nor repelled by them. However, free radicals stand in stark contrast: they are paramagnetic because they possess unpaired electrons, which generate magnetic moments that interact with external magnetic fields.

The essential distinction between a molecule's ground state and its triplet excited state lies in the magnetic properties: the ground state is diamagnetic, while the triplet excited state is paramagnetic. This shift in electron spin makes the transition from a singlet state to a triplet state (or vice versa) far less likely than a singlet-to-singlet transition because it involves a spin flip an event that has low probability. Consequently, the lifetime of a triplet state is significantly longer than that of the singlet state. This difference in transition probabilities also means that absorption bands related to triplet states are less intense since the absorption of radiation that causes a transition to the triplet state is a rare occurrence. Phosphorescence occurs when a molecule, excited in a singlet state, transitions to a triplet state. (Itoh, 2012) (Kaplan, 2017; O'Hara & Kovács, 2022)

The Jablonski diagram depicted in Figure 2.4 offers a visual representation of these processes. This energy diagram shows the various electronic states of a photoluminescent molecule. The lowest, darkest horizontal line represents the ground-state energy of the molecule, which is the singlet state (labeled S_0). At room temperature, the majority of molecules are found in this ground state. Upper lines in the diagram represent excited electronic states: S_1 and S_2 (the singlet states) and T_1 (the triplet state). These are positioned higher on the diagram, with T_1 placed on the right and S_1 and S_2 to the left. The darkest lines at the top of these excited states correspond to their vibrational ground states. Notably, the energy of the triplet state (T_1) is lower than that of the corresponding singlet state, creating an asymmetry in the diagram.

Each of these excited electronic states can contain multiple vibrational levels, which are represented by the thinner lines. Absorption transitions, shown as blue arrows in the diagram, occur when a molecule in the ground singlet state (S_0) absorbs energy and

jumps to one of the vibrational levels in the singlet excited states (S_1 or S_2). Once the molecule reaches an excited singlet state, it may undergo vibrational relaxation (depicted as light blue arrows labeled "R"), dissipating excess vibrational energy. However, the transition from S_0 to the triplet state (T_1) is highly unlikely due to the need for a spin flip, making this transition forbidden. This results in a transition that is much less probable, contributing to the rarity of such transitions in comparison to singlet-singlet transitions.

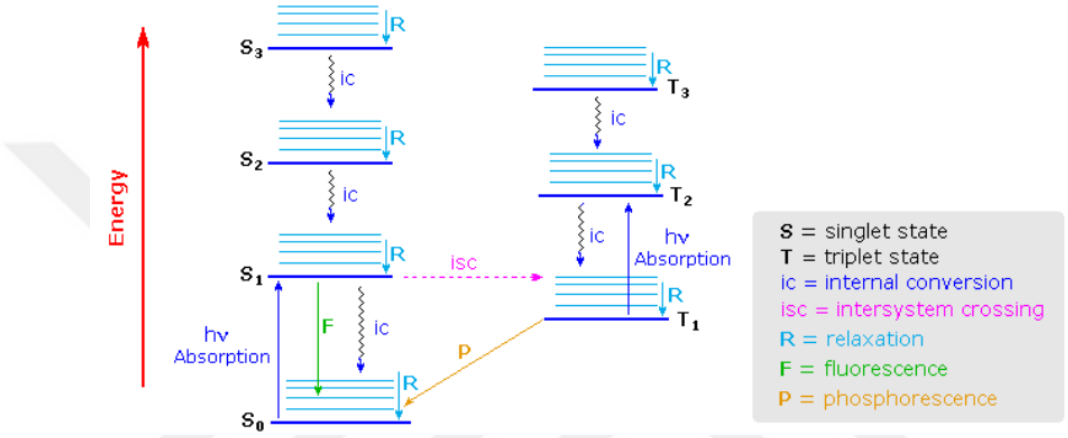


Figure 2.4 Schematic illustration of Jablonski diagram

Phosphorescence involves a delayed emission of light. After the absorption of a photon, the excited electron transitions to a triplet excited state, which has a longer lifetime due to spin-forbidden transitions. This prolonged state leads to delayed emission, often lasting from microseconds to hours after the excitation source is removed (Köhler & Bässler, 2009). Phosphorescence typically occurs in materials exhibiting strong spin-orbit coupling, allowing intersystem crossing between the singlet and triplet states. The delayed emission is characteristic of phosphorescent materials, such as those used in glow in the dark applications and certain organic semiconductors. In addition, emission intensity is significantly lower than fluorescence (Valeur & Berberan-Santos, 2011; Wu et al., 2017).

The primary distinction between fluorescence and phosphorescence lies in the electronic states involved and the time required for the emission of light. Fluorescence is associated with fast, direct transitions between singlet states, while phosphorescence involves slower, triplet state transitions, leading to longer-lived emissions (Friend et

al., 1997; Karabunarliev & Bittner, 2003). Both fluorescence and phosphorescence are essential in a variety of applications. Fluorescence is extensively used in biological imaging, chemical sensing, and optoelectronic devices, whereas phosphorescence is applied in materials for time-resolved spectroscopy, security inks, and glow-in-the-dark technologies (Sasabe & Kido, 2013).

2.2.3 Luminescent Properties of Y_2O_3 and YAG

2.2.3.1 Y_2O_3

The Y_2O_3 has two known phases: cubic and monoclinic. The cubic phase of Y_2O_3, also known as the fluorite phase, is the stable phase at high temperatures of 2600 K (Bose et al., 2011; Yu et al., 2017; Zinkevich, 2007). The cubic phase is characterized by a face-centered cubic crystal structure and is transparent and colorless. The monoclinic phase of Y_2O_3, also known as the bixbyite phase, is the stable phase at room temperature and atmospheric pressure. The monoclinic phase is characterized by a distorted crystal structure and is opaque and black (Zinkevich, 2007). The transition from the cubic to the monoclinic phase occurs at around 1700°C and is accompanied by a significant decrease in volume(Krauss & Birringer, 1997; Lee, Park, Park & Rhee, 2013; Mudavakkat, Atuchin, Kruchinin, Kayani & Ramana, 2012; Tissue & Yuan, 2003; Yan, Liu & Liu, 2011). In addition to the two known phases, Y_2O_3 is also known to exhibit an intermediate hexagonal phase under high pressure. The hexagonal phase has a close-packed hexagonal crystal structure and is stable at pressures above 12 GPa. Overall, the phase diagram of Y_2O_3 is relatively simple, with only two known phases: cubic and monoclinic. However, the ability of Y_2O_3 to exhibit an intermediate hexagonal phase under high pressure makes it an interesting material for high-pressure applications (Bose et al., 2011; Gajović, Tomašić, Djerdj, Su & Furić, 2008; Husson, Proust, Gillet & Itié, 1999; Li, Xia, Xu, Zhong & He, 2019; Wang et al., 2010; Zhang, Gui & Zeng, 2017).

Pure Y_2O_3 does not exhibit significant luminescent properties in the visible light region. However, it has been reported to exhibit weak luminescence in the ultraviolet region, with emission peaks at around 300 nm and 550 nm. This ultraviolet luminescence in pure Y_2O_3 is attributed to intrinsic defects in the crystal lattice, such as oxygen vacancies or interstitial oxygen atoms, which can trap excited electrons and

emit photons upon relaxation (Osipov, Rasuleva & Solomonov, 2008; Osipov, Solomonov, Spirina, Vovkotrub & Strekalovskii, 2014; Pan et al., 2001; Solomonov, Spirina, Spirin & Paranin, 2016). However, the luminescent intensity of pure Y_2O_3 is relatively weak compared to Y_2O_3 doped with rare earth ions, which can exhibit much stronger and tunable luminescence in the visible and infrared regions (Edgar, 2017).

In the literature, studies on Eu doped Y_2O_3 materials are frequently encountered. One example of such a study is as follows. Upon excitation at 255 nm, the emission spectra of Y_2O_3:Eu^{3+} contain a group of peaks, which are from $^5D_1$-$^7F_1$ and $^5D_0$-^7F_J (J = 0, 1, 2, 3, 4) transitions of Eu^{3+} ions, as labeled in Figure 2.5 Among them, the dominant red emission at 610 nm is attributed to the forced electric dipole transition ($^5D_0$-$^7F_2$) of Eu^{3+} ions while peaks at 586, 592, 598 nm are due to the allowed magnetic dipole transition ($^5D_0$-$^7F_1$) of Eu^{3+} ions (Zhang et al., 2012).

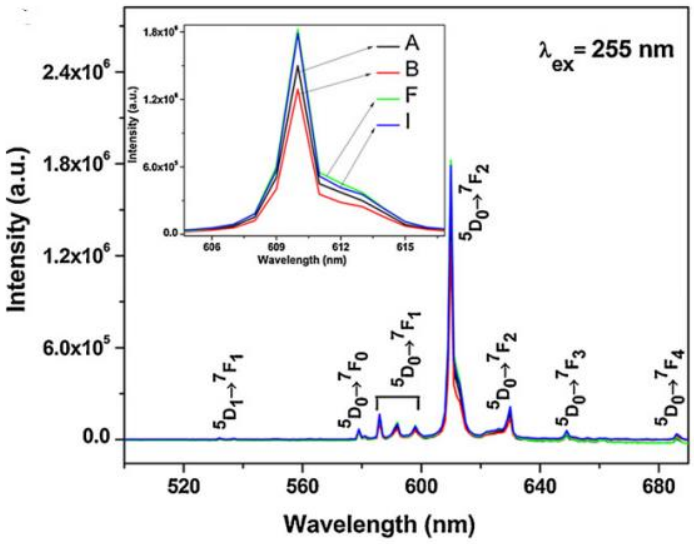


Figure 2.5 Emission spectra of Y_2O_3:Eu^{3+} excited at 255 (Zhang et al., 2012).

2.2.3.2 $Y_3Al_5O_{12}$

The garnet structure was first analyzed by Menzer in 1926 (Menzer, 1929). Artificially obtained garnet crystals $A_3B_5O_{12}$ (A = Y or rare earth element; B = Al, Ga), on the other hand, are used in modern photonic applications, laser systems and electronic systems, thanks to their excellent chemical stability, good thermal

properties, wide transparency range, and suitable hardness (Chen, 2012; Huber, Kränkel & Petermann, 2010; Jüstel, Nikol & Ronda, 1998; Song, Liao, Ding, Liu & Liu, 2013; Speghini, Piccinelli & Bettinelli, 2011; Xia & Liu, 2016; Xia & Meijerink, 2017). The garnet structure is cubically crystalized and exhibits isotropic physical properties thanks to the la-3d space group (Kidyarov & Atuchin, 2007) .

$Y_3Al_5O_{12}$ known as Yttrium Aluminum Garnet (YAG), has high-temperature resistance, high chemical stability and good mechanical properties. YAG is one of the 3 phases with yttrium aluminum monoclinic (YAM) and yttrium aluminum perovskite (YAP) in yttrium aluminum compounds (Kong et al., 2015). Thanks to its centrosymmetric structure, it has optically isotropic properties. Thanks to its high-temperature stability and homogeneous optical properties, it is not only used as a high-temperature structural element material but also used in high-power laser systems and fluorescence applications (Ikesue, Furusato & Kamata, 1995). Nd and Er doped YAG productions are used for laser applications. In addition, Ce dopant is also used for LED and scintillator applications. Since the first Nd-doped YAG synthesis for laser application by Ikeseu in 1995 (Ikesue, Kinoshita, Kamata & Yoshida, 1995), the interest in this material has grown steadily.

In literature, there are many studies about the luminescent properties of YAG phosphors using different dopant elements. According to a research that examines luminescent properties of YAG: Ce^{+3} when the phosphor excited at 455 nm radiation, the PL emission spectrum of YAG:Ce^{+3} phosphors occurred in the range of 480–650 nm with the maximum intensity at around 525 nm. The emission of Ce^{3+} was assigned to the electron transition from the lowest crystal-splitting component of $^5d_2$ to two ground states of $^4f_2$ due to the spin-orbit interaction (Figure 2.6) (Wang et al., 2016).

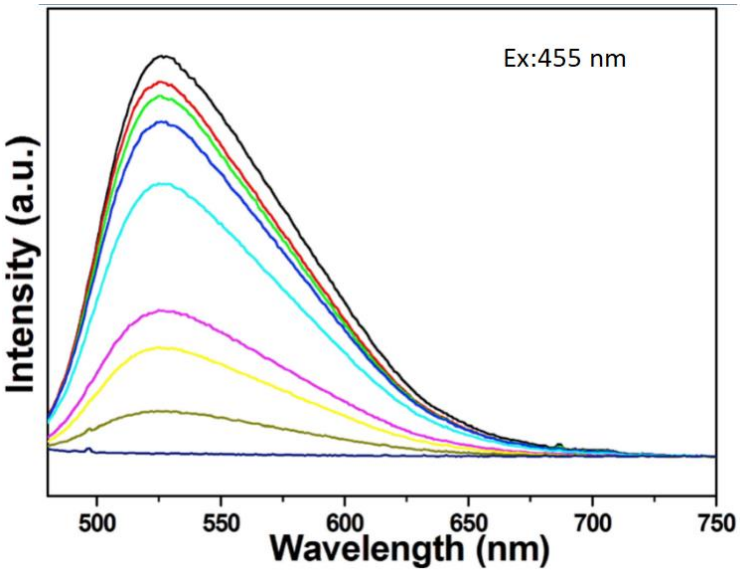


Figure 2.6 Emission spectra of YAG:Ce^{3+} excited at 455 nm (Wang et al., 2016)

Another research revealed that upon excitation with the charge-transfer band of Eu^{3+} ions, the strongest emission peak centered at 590 nm was assigned to the $^5D_0 \rightarrow {}^7F_1$ magnetic dipole transition. In the cubic phase, Y^{3+} is coordinated with eight oxygen ions with D_2 point symmetry, which is a slight deviation from the centrosymmetric D_{2h} point symmetry. The Eu^{3+} ions were substituted into Y^{3+} and were coordinated by eight oxygen ions with D_2 point symmetry (Figure 2.7) (Yang & Jeong, 2010).

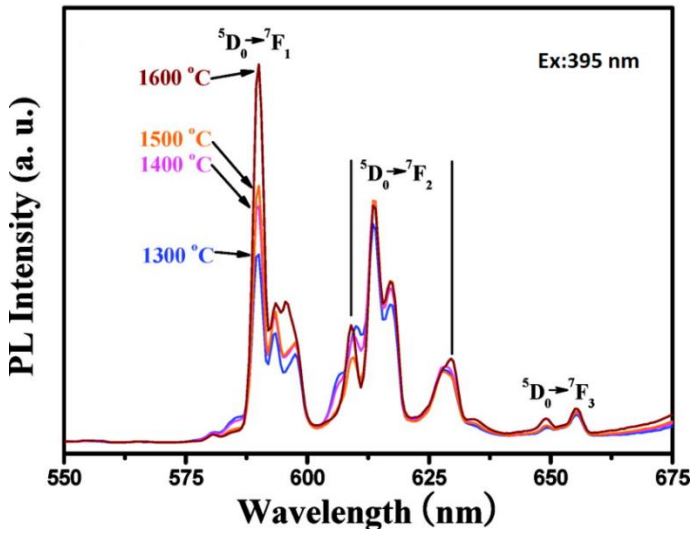


Figure 2.7 Emission spectra of YAG:Eu^{+3} excited at 395 (Yang & Jeong, 2010)

Yttrium Aluminate phosphorus has more than one stoichiometry. These materials have been focused on due to their ability to be excitable in daylight with high stability. The most striking phase of the this phosphor is $Y_3Al_5O_{12}$ While the stoichiometry of the phases affects the excitation and radiation wavelengths, the dopant elements added to the phase can also change these values, and phosphors that glow in different colors such as yellow, orange-red, green or blue can be obtained (Chen et al., 2015; Qiang Liu et al., 2014; Setlur & Srivastava, 2007; Yang et al., 2009). It is thought that the efficiency of photocatalytic excitation can also be increased, thanks to the ability to change the radiant energy and wavelength. With this respect, the YAG was chosen as one of the luminescent materials for our setup.

2.3 Production Techniques of Metal Oxides

Metal oxide materials are of significant interest in a wide range of applications, including catalysis, semiconductor technology, sensors, and energy storage devices, due to their unique electrical, optical, and chemical properties (Chavali & Nikolova, 2019). The production of high-quality metal oxides often requires the implementation of precise fabrication techniques that allow for control over the chemical composition, structure, and morphology of the final product. There are a variety of methods to produce metal oxides such as sol-gel, chemical vapor deposition (CVD), physical vapor deposition (PVD), atomic layer deposition (ALD), hydrothermal and solvothermal synthesis, spray pyrolysis, ball milling, electrochemical deposition. Each of these techniques has its unique advantages and limitations depending on the desired properties of the final metal oxide semiconductor material (Bizarro, 2010; Gültekin et al., 2019; Hamelmann, 2016; Huber, Madel, Reiser, Bauer & Thonke, 2016; Hunge, Yadav & Mathe, 2019; Jimenez-Cadena, Comini, Ferroni, Vomiero & Sberveglieri, 2010; Salah et al., 2011; Tynell & Karppinen, 2014). The choice of production method is guided by the specific application requirements, such as film thickness, uniformity, crystallinity, and morphology, as well as scalability and cost considerations. Methods like sol-gel and hydrothermal synthesis are excellent for producing nanostructured materials, while techniques such as CVD, ALD, and PVD are ideal for thin films and semiconductor device fabrication. In our study, we focused on sol-gel technique.

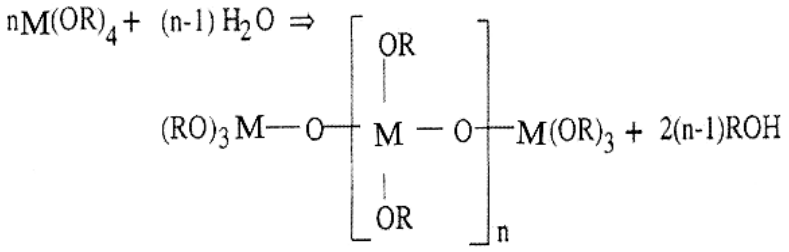
2.3.1 Sol-Gel Process

The sol-gel process is a versatile chemical technique used to create a gel-like network from a chemical solution or colloidal dispersion. In this process, sols, dispersions of colloidal particles in a liquid, are transformed into gels, rigid, interconnected networks with submicrometer-sized pores and polymeric chains exceeding a micrometer in length (Hench & West, 1990).

Metal alkoxides and metal chlorides are common precursors for the sol-gel process. The overall procedure involves several key stages: hydrolysis and polycondensation of these precursors, followed by gelation, drying, and sintering. One of the effective models used to predict these reactions is the Partial Charge Model. Ligands, which are atomic or molecular groups, can attach to a complex C or cation M either directly or by replacing another ligand. The transformation mechanism is influenced by the partial charge of different atoms in the species; nucleophilic atoms have a negative partial charge, while electrophilic ones have a positive charge. In a substitution reaction, the nucleophile is the ligand with the highest partial charge, while the leaving group in the metal complex has the highest positive charge (Pierre, 2013).

2.3.2 Hydrolysis and Condensation Reaction

Hydrolysis is a process that can be described by the deprotonation of a solvated M cation, leading to the loss of a proton from one or more water molecules surrounding the M in the first solvation shell. During hydrolysis, the aqua ligand molecule (H_2O) bonded to the metal transforms into a hydroxo ligand (OH^-) if only one proton is lost, or into an oxo ligand (O^{2-}) if two protons are removed.



(Hydrolysis) Eq. (2.14)

After hydrolysis, condensation reactions occur, forming a polynuclear complex with two metal atoms. In aqueous solutions, condensation can result from either an olation or oxolation reaction. Care must be taken as oxygen can sometimes accelerate the reaction, making it necessary to work in an inert atmosphere, such as argon, to control the process (Pierre, 2013). In the olation process, a hydrogen atom is transferred to an OR ligand according to the following reaction:

$$2M(OR)_{x-1}(OH) \rightarrow M_2O\,(OR)_{2X-3} + ROH \qquad \text{Eq. (2.15)}$$

In oxolation, the hydrogen atom is transferred to an OH group according to the following reaction:

$$2M(OR)_{x-1}(OH) \rightarrow M_2O\,(OR)_{2X-3} + H_2O \qquad \text{Eq. (2.16)}$$

As hydrolysis and condensation continue, they build a three-dimensional network that eventually forms a solid gel. The rate of these reactions is temperature-dependent, with varying pH influencing the structure and type of polymers formed, ranging from linear polymers to dense colloidal particles and cross-linked clusters (Pierre, 2013).

2.3.3 Gelation

Gelation is the stage where the sol or solution transforms into a gel by forming a three-dimensional network. This transition occurs when the extent of polymerization reactions reaches a critical threshold, known as the gel point, at which a polymer of infinite size is formed. This point marks the shift from a viscous liquid to a material with elastic properties. Gelation can be described through percolation theories, which model the formation of networks by establishing bonds or occupying sites in a random manner across a geometrical lattice. The simplest percolation models, such as bond percolation and site percolation, help to understand how these networks evolve into a continuous structure as the probability of bond formation or site occupancy increases (Figure 2.8) (Pierre, 2013).

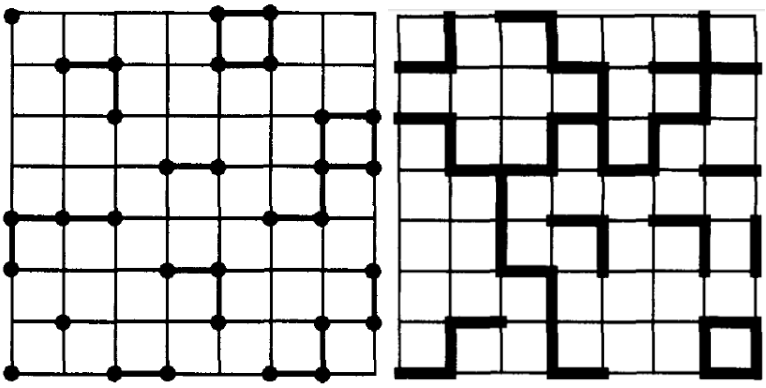


Figure 2.8 (a) Site percolation and (b) bond percolation on a square bi-dimensional network (Hench & West, 1990)

2.3.4 Drying and Sintering

The drying phase is an irreversible process that removes the liquid from the gel, which is initially composed of a solid network and a liquid matrix. During drying, evaporation creates a liquid-vapor meniscus at the pore exits, inducing hydrostatic tension in the liquid and axial compression on the solid. This compression causes the gel to shrink, further concentrating the remaining liquid and continuing the evaporation process. Sintering follows drying and involves heating the material to high temperatures. This process reduces the specific surface area and eliminates pores, resulting in a denser and more stable material. Sintering can involve two types of pore evaluations: changing the shape of pores without altering their volume or completely eliminating them. The end result is a material with improved mechanical properties and stability (Pierre, 2013).

2.4 Motivation of the Research

The integration of photoluminescent and photocatalytic properties in materials offers significant potential for enhancing the efficiency of photocatalytic processes. ZnO, Y_2O_3, and YAG are well-known materials for their individual photocatalytic and photoluminescent properties, but research exploring their synergistic effects in composite forms remains limited. Specifically, the potential to utilize photoluminescence as a mechanism to enhance photocatalytic activity is underexplored, despite its promise for improving photocatalytic efficiency. This thesis

seeks to address this gap by investigating ZnO-based composites, incorporating Y_2O_3 and YAG, as materials for advanced photocatalytic applications.

The motivation for this study is driven by the need to explore the complementary effects of photoluminescence and photocatalysis. While traditional photocatalysts like ZnO have demonstrated substantial photocatalytic potential, there is an opportunity to enhance their performance through composites with other materials that influence energy transfer. By combining ZnO with Y_2O_3, which lacks photocatalytic activity but can potentially enhance ZnO's efficiency, this study aims to optimize photocatalytic performance. The results of this research will provide deeper insights into the interplay between luminescence and photocatalysis and open the door to more effective composite materials for future photocatalytic technologies.

CHAPTER THREE
EXPERIMENTAL STUDIES

3.1 The Aim of Thesis

Composite structures have been the subject of extensive research over the past few decades because of their potential for use in a wide range of applications, including fuel cells, photonic applications, detectors, thin film transistors, and photocatalytic applications. In this thesis we focus on composite materials with unique properties that are easy to apply in photocatalytic applications. We synthesized ZnO nanoparticles using the sol-gel method to serve as the photocatalytic material in the composite structure. Additionally, we produced photoluminescent materials Y_2O_3 and YAG also through the sol-gel method, which functions as the photoluminescent component of the composite structure. Moreover, Eu^{+3} and Ce^{+3} doped Y_2O_3 and YAG materials were produced. Using a simple and cost-effective mechanical mixing technique, we developed ZnO-Y_2O_3 and ZnO-YAG nanocomposite photocatalytic structures with varying weight percentages of the photoluminescent materials. We also synthesized combined ZnO-Y_2O_3 and ZnO-YAG structures using a precipitation technique for comparison with the composite structures. The aim of this thesis is to clarify preparation methods and characterization of photocatalytic-photoluminescent composite structures, as well as to improve the performance of photocatalytic metal oxide nanoparticles. This new approach investigates the influence of photoluminescent materials on photocatalytic activity, establishing connections between the observed results and the properties of materials. Furthermore, it seeks to highlight engineering concepts that could be utilized to develop or enhance photocatalytic systems.

Sol-derived photocatalytic and photoluminescent particles were combined in varying weight ratios to determine optimal parameters for producing composite photocatalytic structures. DTA-TG and FTIR analyses were employed to establish an appropriate heat treatment regime and to describe the chemical structure and reaction type of intermediate temperature products. XRD analysis was used to monitor the phase structure of ceramic nanoparticles and the composite structure. The morphology of the particles was revealed by the SEM instrument. A BET device was used to assess the particle surface area, which fluctuates depending on production conditions. UV-

Vis spectroscopy was used to assess the optical and photocatalytic characteristics of the composite structures as well as the pure particles.

3.2 Precursor Materials

Precursor materials were chosen from alkoxide-based chemical materials which can be easily dissolved in organic solvents such as distilled water. Zinc nitrate hexahydrate ($Zn(NO_3)_2 \cdot 6H_2O$ (Sigma-Aldrich), Triethanolamine $N(CH_2CH_2OH)_3$ (Sigma-Aldrich) and Acetic acid, glacial $C_2H_4O_2$ (Merck) was chosen for the production of ZnO as precursor material, chelating agent and surfactant, respectively.

Yttrium(III) nitrate hexahydrate $Y(NO_3)_3 \cdot 6H_2O$ (Sigma-Aldrich), Aluminum nitrate nonahydrate $Al(NO_3)_3 \cdot 9\ H_2O$ (Sigma-Aldrich), citric acid monohydrate ($C_6H_8O_7 \cdot H_2O$) (Sigma-Aldrich) and Ethylene Glycol $C_2H_6O_2$ (Sigma-Aldrich) was used to synthesize photoluminescent components. All chemicals were used as received without any further purification.

Table 3.1 lists the chemical materials employed for the production of photocatalytic metal oxide nanoparticles and photoluminescent particles, including the chemical types, names, formulas, and purity percentages of precursor materials.

Table 3.1 All chemicals used for the production of ZnO nanoparticles, Y_2O_3 and YAG powders

Material	Chemical Type	Chemical	Formula	Purity
Photocatalyst	**Precursor**	Zinc Nitrate Hexahydrate	$Zn(NO_3)_2 \cdot 6H_2O$	99 %
	Solvent	Ethanol	C_2H_5OH	100 %
	Chelating Agent	Acetic acid, glacial	$C_2H_4O_2$	99.90 %
	Surfactant	Triethanolamine	$N(CH_2CH_2OH)_3$	98%
Photoluminescence	**Precursor**	Yttrium(III) Nitrate Hexahydrate	$Y(NO_3)_3 \cdot 6H_2O$	99 %
		Aluminum Nitrate Nonahydrate	$Al(NO_3)_3 \cdot 9\ H_2O$	99 %
		Europium (III) nitrate pentahydrate	$Eu(NO_3)_3 \cdot 5H_2O$	99 %
		Cerium (III) nitrate hydrate	$Ce(NO_3)_3 \cdot H_2O$	99 %
	Solvent	Distilled Water	H_2O	99 %
	Chelating Agent	Citric Acid Monohydrate	$C_6H_8O_7 \cdot H_2O$	99.90 %
	Surfactant	Ethylene Glycol	$C_2H_6O_2$	98%

3.3 Synthesis of ZnO Nanoparticles

Precursors were weighted in appropriate amounts in the defined molar ratio to prepare Zn based solutions. Firstly, 0.3 M of Zinc nitrate hexahydrate (($Zn(NO_3)_2 \cdot 6H_2O$) was hydrolyzed in 300 ml of absolute ethanol (C_2H_5OH). After stirring the solution for 30 min, 3 ml glacial acetic acid ($C_2H_4O_2$) was added into the solution. The stirring was kept for 30 min in order to obtain a homogeneous and transparent solution. Then 0.1 mol of triethanolamine ($N(CH_2CH_2OH)_3$) was added to the solution as an agent under vigorous solution for 30 min more. The solution was left to age for 24 hours at 70 °C. Once gelation occurred, the gel was subjected to drying at 120 °C for 18 hours to form xerogel. To ensure a smaller particle size, the ZnO powders, derived from the sol-gel process, were ground in an agate mortar for 10 minutes after drying. With this respect. dried xerogel structure was prepared for further analysis and production processes such as heat treatment. During the heat treatment, Protherm box furnace temperature was gradually raised to 275 °C at a rate of 10 °C/min and held for 30 minutes. the temperature was then gradually increased to 500 °C at the same rate, after which samples were held at this temperature for 3 hours in an air environment. Following this period, a self-cooling process inside the furnace was initiated. Figure 3.1 illustrates the heating regime of ZnO nanoparticles.

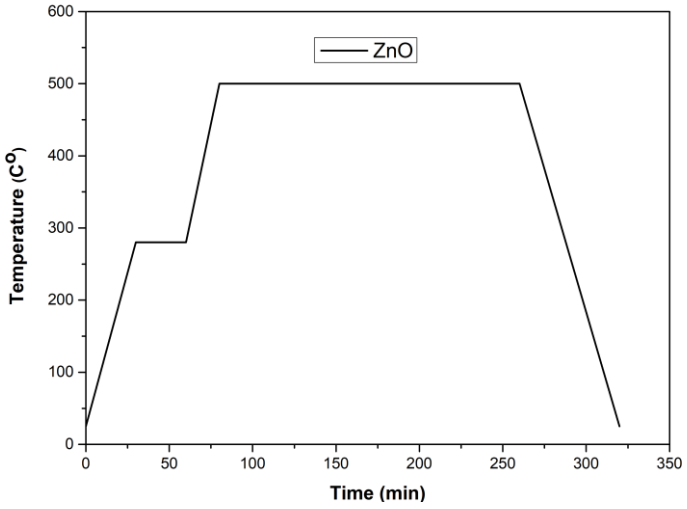


Figure 3.1 Heat treatment regime for ZnO

The milling process was repeated following heat treatment, as the particles tend to aggregate into submicron-sized clusters post heating Flow chart of ZnO production is

shown in Figure 3.2. Chemical reactions of ZnO synthesis is given below (Barhoum et al., 2017; Siswanto, Rochman & Akwalia, 2017; Toyoda, Watanabe & Matsumiya, 1999).

The first step is to dissolve zinc nitrate hexahydrate in absolute ethanol. The zinc precursor dissociates into zinc ions (Zn^{2+}) in the solvent:

$$Zn(NO)_3 \cdot (6H_2O) \rightarrow Zn^{2+} + NO_3^- + 6H_2O \qquad \text{Eq. (3.1)}$$

In the chelation and hydrolysis steps, glacial acetic acid is added to the solution to act as a chelating agent. Acetic acid coordinates with the zinc ions to form a complex, stabilizing the metal ion and slowing down the hydrolysis reaction:

$$Zn^{2+} + 2CH_3COOH \rightarrow [Zn(CH_3COO)_3]^{2-} \qquad \text{Eq. (3.2)}$$

Upon adding water or humidity in the air, hydrolysis occurs, where the zinc acetate complex undergoes hydrolysis, producing hydroxyl groups that will participate in the gelation process:

$$[Zn(CH_3COO)_3]^{2-} + 6H_2O \rightarrow Zn(OH)_2 + 2CH_3COO \qquad \text{Eq. (3.3)}$$

The hydrolyzed zinc hydroxide undergoes a condensation reaction, leading to the formation of a metal-oxygen-metal (Zn–O–Zn) bond and the release of water. This results in the formation of a gel:

$$Zn(OH)_2 \rightarrow ZnO + H_2O \qquad \text{Eq. (3.4)}$$

The resulting gel is dried to remove ethanol and excess water. This step is crucial for removing the solvent and obtaining a solid structure. The dried gel is then calcined at 500 ^{o}C to convert the zinc hydroxide to crystalline ZnO.

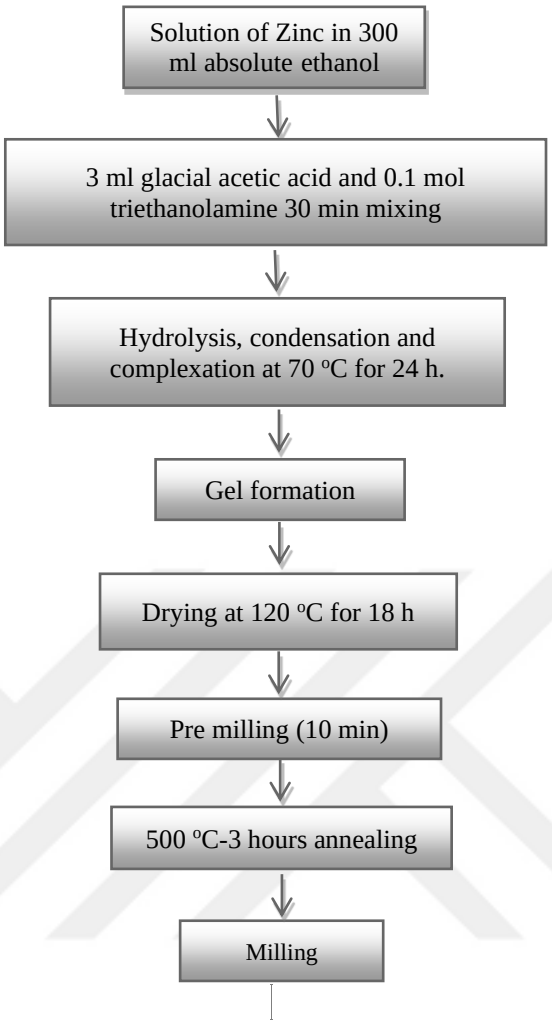


Figure 3.2 Flow chart of ZnO production

3.4 Synthesis of undoped and doped Y_2O_3 Particles

Y_2O_3 particles were prepared by using Yttrium(III)nitrate hexahydrate ($Y(NO_3)_3 \cdot 6H_2O$) as a precursor and citric acid monohydrate ($C_6H_8O_7 \cdot H_2O$) as a chelating agent by sol-gel technique. In order to investigate the effect of acid concentration on the final product, the molar ratios of citric acid to the total metal metallic ions (MRCM) were chosen as 0.5, 1 and 2. 0.2 M precursor solution was prepared by using ($Y(NO_3)_3 \cdot 6H_2O$) and distilled water. Then the solution was divided into 3 equal amounts for different acid concentrations. Citric acid was added to each solution at a concentration of 0.005, 0.01 and 0.02 mol. 2 ml Ethylene glycol was added to each solution. MRCM ratios, pH values, amount of ethylene glycol for each solution are given in Table 3.2

Table 3.2 MRCM ratios, pH values, amount of ethylene glycol for Y_2O_3 each solution

Sample Designation	MRCM	pH	EG
Y_2O_3 0.5 MRCM	0.005/0.01	4	2 ml
Y_2O_3 1 MRCM	0.01/0.01	2	2 ml
Y_2O_3 2 MRCM	0.02/0.01	1	2 ml

All solutions were stirred for 1 hour at room temperature. In order to remove the excess water, the solution was heated to a temperature of 70°C, causing it to become increasingly viscous. During this stage, the interaction between CA and metal ions took place. All chemicals dissolved in a total 0.025 L of distilled water. To create the gel, the solution was heated at a temperature of 120 °C for 18 hours. The resulting gel was then placed in an oven at a temperature of 200°C for five hours, during which the esterification of citric acid and ethylene glycol took place resulting in voluminous, brown porous foam as depicted in Figure 4.13. The foam structure was pre- for 10 minutes. Finally, heat treatment was carried out. To ensure full combustion of organic content, the samples were held at 450 °C for 1 hour. Subsequently, the furnace temperature was increased at a rate of 10 °C/min to 1000 °C, where it was maintained for an additional 3 hours to facilitate phase transformation. The samples were then left to cool within the furnace. Given the similarity in DTA-TG data for the Y_2O_3 and YAG samples, the same heat treatment regime was applied to both materials. The annealing process of Y_2O_3 is shown in Figure 3.3

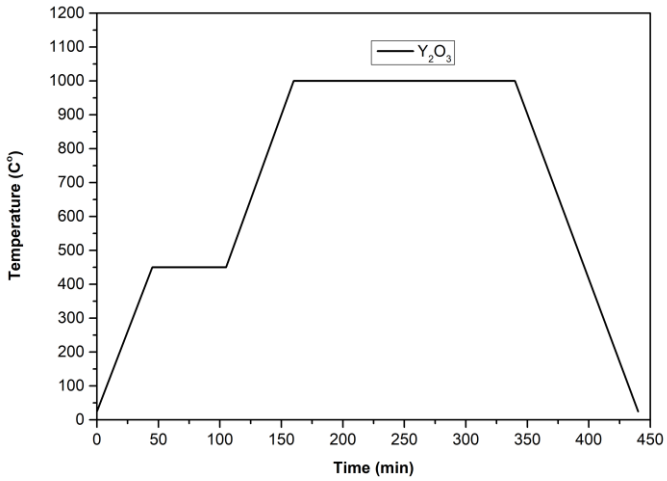


Figure 3.3 Heat treatment regime for Y_2O_3

The chemical reaction during the sol-gel synthesis process of Y_2O_3 involves several steps (Dupont, Parent, Le Garrec & Heintz, 2003; Loembe, Fu, Wang & Wang, 2015; Sim, Keller & Mah, 2000). First, Yttrium(III)Nitrate Hexahydrate is dissolved in distilled water. This dissociates the yttrium nitrate into yttrium ions (Y^{3+}) and nitrate ions $(NO_3)^-$, forming the sol:

$$Y(NO)_3 \cdot (6H_2O) \rightarrow Y^{3+} + NO_3^- + 6H_2O \qquad \text{Eq. (3.5)}$$

Citric acid is added to the solution as a chelating agent. The citric acid coordinates with the yttrium ions to form a complex. This chelation process prevents the rapid precipitation of yttrium hydroxide and helps control the hydrolysis reaction

$$Y^{3+} + C_6H_8O_7 \rightarrow [Y(C_6H_8O_7)]^{3-} \qquad \text{Eq. (3.6)}$$

Citric acid provides both carboxylate groups (–COOH) and hydroxyl groups (-OH) that can form stable complexes with the yttrium ion. This results in a chelate complex that stabilizes the yttrium ion in solution, reducing unwanted side reactions.

Water is then added, leading to hydrolysis, where the yttrium complex undergoes hydrolysis to form yttrium hydroxide ($Y(OH)_3$) along with the release of citric acid:

$$[Y(C_6H_8O_7)]^{3-} + 3H_2O \rightarrow Y(OH)_3 + 3\,C_6H_8O_7 \qquad \text{Eq. (3.7)}$$

Upon further processing (e.g., heating), the yttrium hydroxide undergoes condensation, leading to the formation of Y_2O_3 through the elimination of water. This

step is part of the gelation process, where the sol transforms into a gel structure. The reactions during this step are as follows:

$$2Y(OH)_3 \rightarrow Y_2O_3 + 3H_2O \qquad \text{Eq. (3.8)}$$

This reaction involves the loss of water and results in the formation of the yttrium oxide phase. The gel is dried to remove residual water, and it is then calcined at 1000°C to crystallize the Y_2O_3 and remove any remaining organic material, such as residual citric acid.

Doped Y_2O_3 particles were synthesized similarly to undoped Y_2O_3. Different molar ratios of Europium (III) nitrate pentahydrate were dissolved in distilled water, with the molar ratio of Eu to Y ranging between 0.25% to 2% (0.25, 0.5, 1, and 2%). After adding the Eu precursor solution to the Y precursor solution, 1 hour of stirring was performed. Eu-doped samples were designated Y_2O_3 0.25%Eu, Y2O3 0.5%Eu, Y_2O_3 1%Eu, and Y_2O_3 2%Eu, respectively, according to the amount of Eu addition.

Ce doped Y_2O_3 nanoparticles were synthesized by using a similar preparation route as Eu doped Y_2O_3 particles. Whereas, only 1% dopant concentration was prepared. Ce doped Y_2O_3 samples designated Y_2O_3 1%Ce. The flow chart of Y_2O_3 production is illustrated in Figure 3.4. The designated name of all samples is given in Table 3.3.

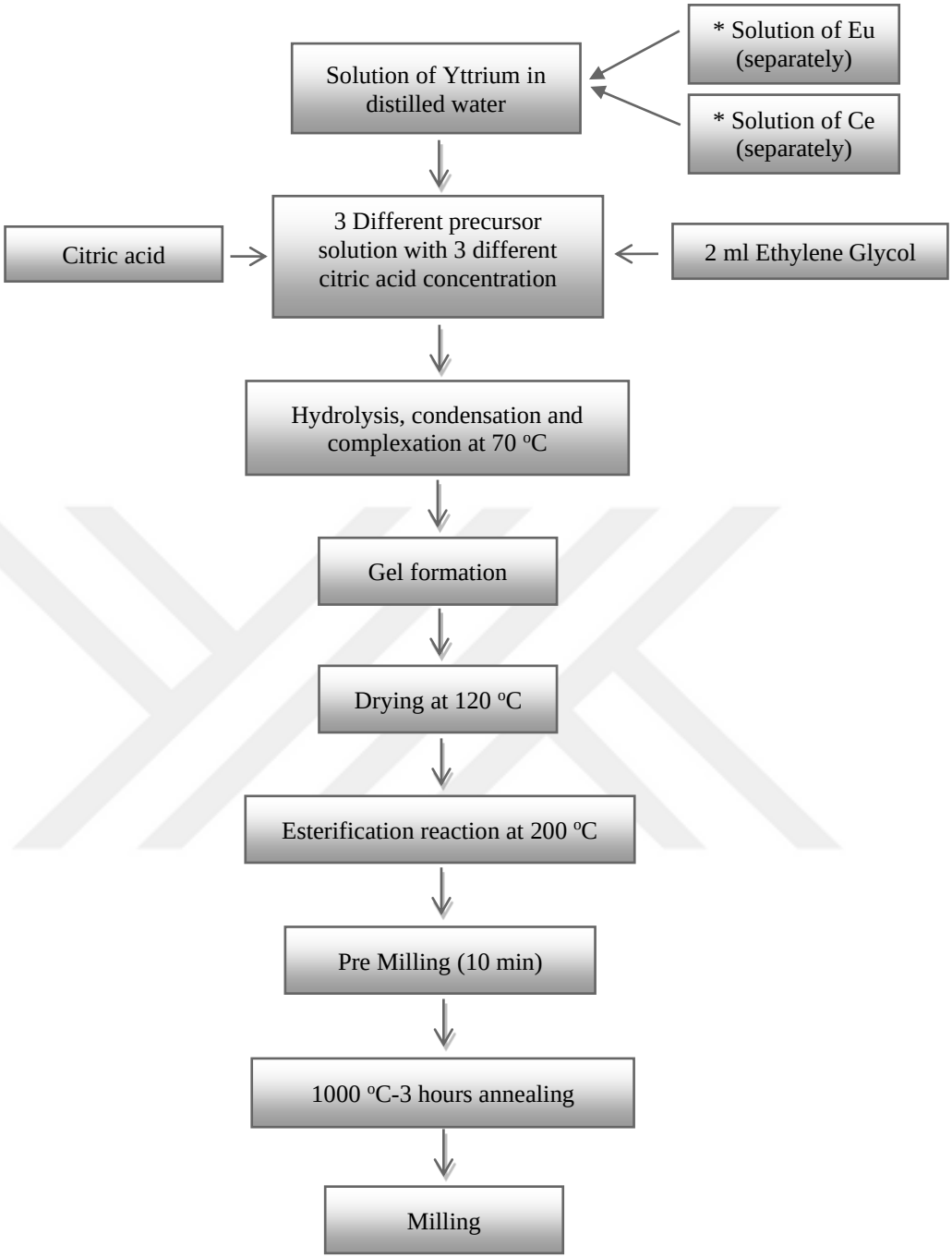


Figure 3.4 Flow chart of pure, Eu doped, Ce doped Y_2O_3 production

*: Eu and Ce dopant materials were used only for the solution containing 2 MRCM because of high surface area of it.

Table 3.3 Content of doped Y_2O_3 samples

Sample Designation	MRCM	Molar Ratio of Eu or Ce Dopant to Y
Y_2O_3 %0.25 Eu	2	0.25/100
Y_2O_3 %0.5 Eu	2	0.5/100
Y_2O_3 %1 Eu	2	1/100
Y_2O_3 %2 Eu	2	2/100
Y_2O_3 %1 Ce	2	1/100

3.5 $Y_3Al_5O_{12}$ (YAG) production

In the study, YAG particles were prepared by using Yttrium (III) nitrate hexahydrate $Y(NO_3)_3 \cdot 6H_2O$ and aluminum nitrate nonahydrate $Al(NO_3)_3 \cdot 9H_2O$. Citric acid monohydrate $C_6H_8O_7 \cdot H_2O$ is preferred as chelating agent. Total solution contains 0.02 Mol metal ion. With this respect 0.4 molar citric acid solution (MRCM:2) by prepared by means of dissolving citric acid monohydrate in distilled water. 0.2 molar precursor solution was prepared by mixing Y and Al solution in 0.1 L distilled water. The solution was stirred for 1 hour at room temperature. In order to remove the excess water, the solution was heated to a temperature of 70 °C, causing it to become increasingly viscous. During this stage, the interaction between CA and metal ions took place. To create the gel, the solution was heated at a temperature of 120 °C for 18 hours. The resulting gel was then placed in an oven at a temperature of 200°C for five hours to complete the esterification reaction between ethylene glycol and citric acid. Finally dried powders were calcined in a furnace at a temperature of 1000°C for 3 hours and allowed to cool to room temperature. Figure 3.5 gives the heat treatment regime of YAG particles

Eu and Ce doped YAG particles were also prepared using a similar route. Molar ratio of Eu and Ce to Y ion is 1%. 0.2 molar total precursor solution was prepared by mixing the Y, Al, and Eu (or Ce) solution in 0.1 L distilled water. The total solution contains 0.02 Mol metal ions. Figure 3.6 illustrates a flow chart of the production of pure YAG, YAG 1%Eu, and YAG 1%Ce preparations. Table 3.4 gives the content of

undoped and doped YAG samples. Table 3.5 provides a detailed recipe for the production of pure, Eu doped, and Ce doped YAG powders.

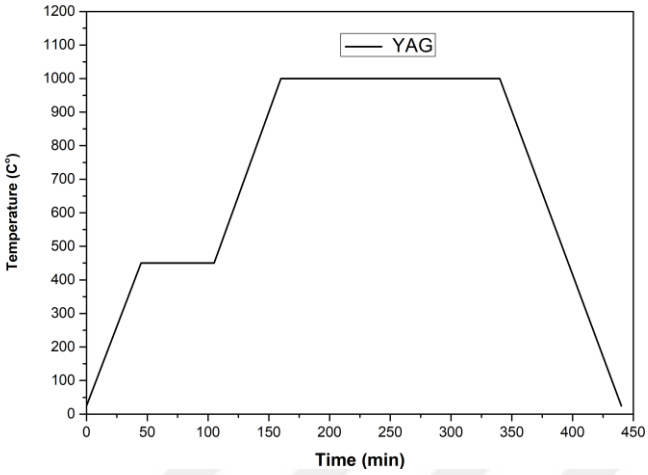


Figure 3.5 Heat treatment regime for YAG

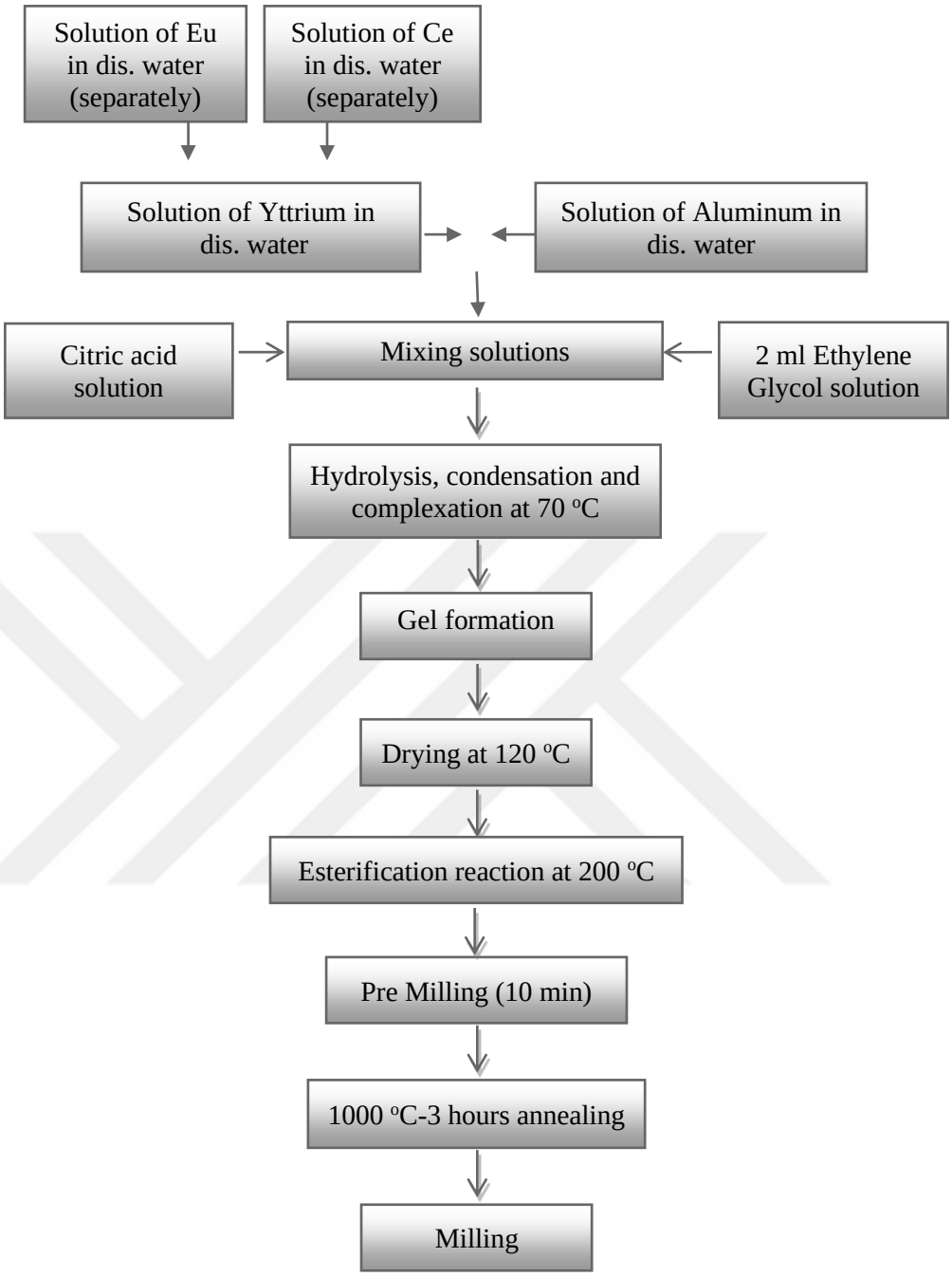


Figure 3.6 Flow chart of pure, Eu doped and Ce doped YAG production

Table 3.4 Content of doped and undoped YAG samples

Sample	MRCM	Molar Ratio of Eu or Ce Dopant to Y
YAG	2	0/100
YAG %1 Eu	2	1/100
YAG %1 Ce	2	1/100

Table 3.5 Recipe for pure, Eu doped, Ce doped YAG powders

	Formula	**$Y(NO_3)_3$ $6H_2O$**	**$Al(NO_3)_3$ 9 H_2O**	**$C_6H_8O_7.H_2O$**	**$C_2H_6O_2$**
0.0025 mol $Y_3Al_5O_{12}$	**Molecular Weight (g/mol)**	383.01	375.13	210.14	62.07
	Element	Y	Al		
	Stochiometric constant	3	5	16	
	For 0.0025 Mol product (g)	2.84	4.68	8.40	2 ml

	Formula	**$Y(NO_3)_3$ $6H_2O$**	**$Al(NO_3)_3$ 9 H_2O**	**$Eu(NO_3)_3$ $5H_2O$**	**$C_6H_8O_7.$ H_2O**	**$C_2H_6O_2$**
0.0025 mol $Y_{2.97}Al_5O_{12}$:0.03Eu	**Molecular Weight (g/mol)**	383.01	375.13	428.06	210.14	62.07
	Element	Y	Al	Eu		
	Stochiometric constant	2.97	5	0.03	16	
	For 0.0025 Mol product (g)	2.84384925	4.689125	0.0321045	8.4056	2 ml

	Formula	**$Y(NO_3)_3$ $6H_2O$**	**$Al(NO_3)_3$ 9 H_2O**	**$Ce(NO_3)_3$ H_2O**	**$C_6H_8O_7.$ H_2O**	**$C_2H_6O_2$**
0.0025 mol $Y_{2.97}Al_5O_{12}$:0.03Ce	**Molecular Weight (g/mol)**	383.01	375.13	344.15	210.14	62.07
	Element	Y	Al	Ce		
	Stochiometric constant	2.97	5	0.03	16	
	For 0.0025 Mol product (g)	2.84384925	4.689125	0.02581125	8.4056	2 ml

3.6 Composite ZnO-Y_2O_3 Production

Experimental studies were performed in order to find the optimum amount of luminescent material to be used. This was accomplished by creating ZnO-Y_2O_3 composites with four distinct Y_2O_3 concentrations.

Pure ZnO and pure Y_2O_3 were also synthesized for comparison. Figure 3.7 shows the production of composite ZnO-Y_2O_3 samples. It is worth noting that the composite materials, synthesized by mechanical mixing, were not subject to an additional heat treatment following the initial thermal process.

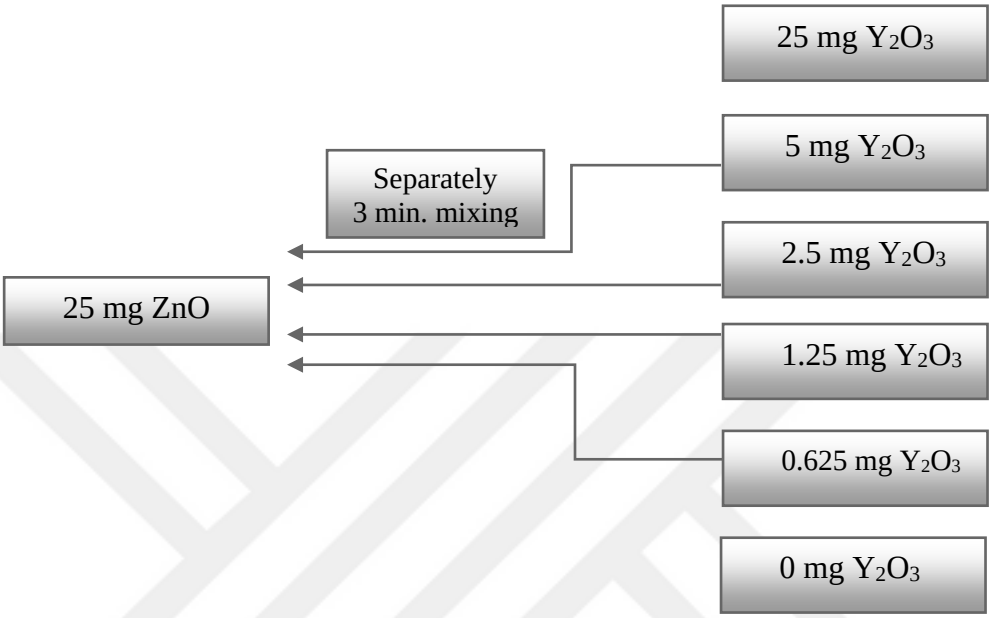


Figure 3.7 Composite ZnO-Y_2O_3 samples preparation

3.7 ZnO-Y_2O_3 Production by Precipitation

A combination of ZnO-Y_2O_3 structures was generated using the precipitation method. The amount of starting Zn precursor ($Zn(NO_3)_2{\cdot}6H_2O$) and previously prepared Y_2O_3 was adjusted according to ratio of 100/5, respectively. Our goal was to produce a photocatalytic ZnO product with a 5% phosphorus concentration by weight of ZnO. 5% phosphorus including ZnO is abbreviated as ZnO-5Y_2O_3.

Y_2O_3 particles were dispersed in an acidic environment prior to the addition of NaOH to a 200 ml distilled water solution. Citric acid was used to bring the pH value down to 2. Zn precursor was completely dissolved in an acidic solution, including Y_2O_3 particles. The temperature of the solution was set at 80 ^oC. 3 mg PEG was also added to the total solution to increase the effectiveness of ZnO-Y_2O_3 combination.

The precipitation starts as soon as NaOH is introduced to the solution. Continuous additions of NaOH were made until the pH value reached 8. The final solution was stirred for 2 hours. Then dried at 120 ^{o}C for 24 hours. During the heat treatment, furnace temperature was gradually raised to 275 °C at a rate of 10 °C/min and held for 30 minutes. The temperature was then gradually increased to 500 °C at the same rate, after which samples were held at this temperature for 3 hours in an air environment. Notably, the combined ZnO-Y_2O_3 and materials were not milled at any stage of the process to prevent any distortion of their structural shape. The heat treatment regime of ZnO-5Y_2O_3 is given in Figure 3.8. the flow chart for the synthesis of it is shown in Figure 3.9.

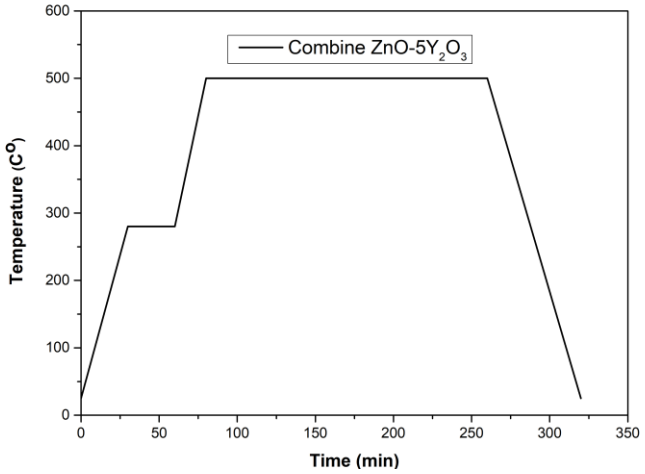


Figure 3.8 Heat treatment regime for Combine ZnO-5Y_2O_3 produced by precipitation

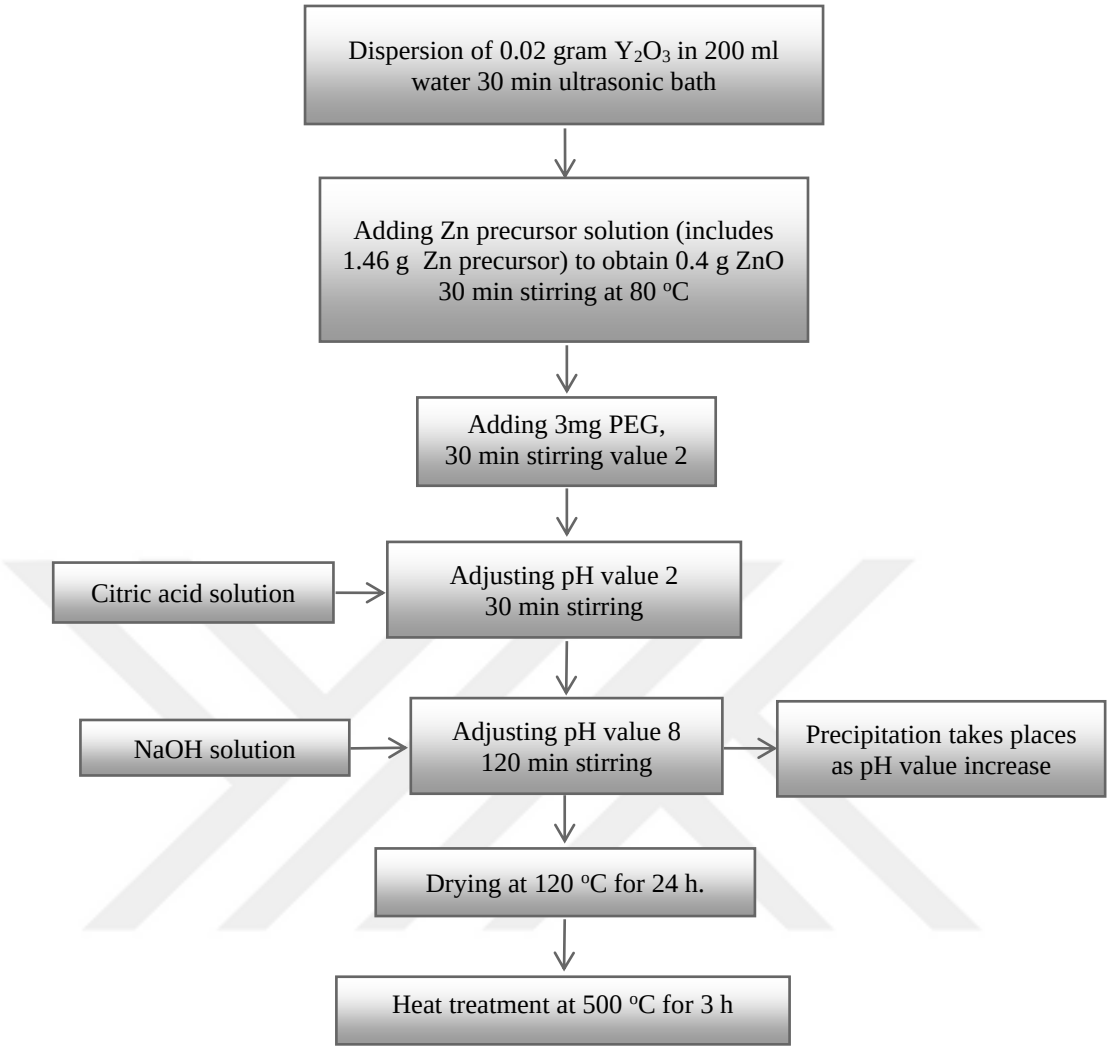


Figure 3.9 Flow chart of combine ZnO-5Y_2O_3 production by precipitation

3.8 Characterization

3.8.1 Solution Characterization

3.8.1.1 Ph Measurement

The pH measurement is a way to determine the concentration of hydrogen ions in a solution. pH can affect the acidity of a solution, as well as the speed and solubility of various chemical processes and compounds. pH measurement holds paramount significance in the sol-gel production process as it profoundly influences the chemical reactions and properties of the resulting materials. The pH level plays a crucial role in

controlling precursor molecules' hydrolysis and condensation reactions, influencing the formation of stable sols and gels. The pH of the solution affects the size, structure, and uniformity of the nanoparticles formed during the sol-gel synthesis. Additionally, it governs the stability of colloidal suspensions and the subsequent gelation process. Precise pH control is essential for tailoring the morphology, particle size, and overall characteristics of the final sol-gel products, ensuring the desired material properties are achieved. Deviations in pH can lead to variations in gelation kinetics, crystallinity, and surface chemistry, making pH measurement a key parameter for quality control and reproducibility in the synthesis of sol-gel materials. This study investigates the effect of solution pH on the surface area of Y_2O_3 particles. Hanna HI83141 pH meter was used to measure pH values.

3.8.1.2 Turbidity Measurement

Turbidity is a measure of the clarity or cloudiness of a liquid. It is determined by shining light through the liquid and measuring the amount of light that is scattered at a 90° angle to the incident light. The greater the number of suspended particles in the liquid, the more light will be scattered and the higher the turbidity value will be. In this experiment, the turbidity of the prepared precursor solutions was measured using a VELP TB1 Turbidimeter, which converts the scattered light detected by a photodiode into a linearized signal displayed as a value in Nephelometric Turbidity Units (NTU).

3.8.1.3 Fourier Transform Infrared Spectroscopy (FT-IR)

Fourier Transform Infrared (FTIR or IR) spectroscopy is a method employed to investigate the absorption of infrared radiation by both organic and inorganic substances. The distinct absorption bands correspond to specific molecular features or structures, and the infrared radiation induces vibrations in the chemical bonds of the material at characteristic frequencies within the infrared range. The IR spectrum is conventionally categorized into three regions based on frequency: far IR (10-400 cm^{-1}), mid IR (400-4000 cm^{-1}), and near IR (4000-14000 cm^{-1}). In this study, the Perkin Elmer Spectrum BX instrument equipped with ATR apparatus was used to analyze spectra in the range of 4000 to 650 cm^{-1} with a resolution of 1 cm^{-1}. 25 scans were recorded with a resolution of 4 cm^{-1} for each sample.

3.8.2 Material Characterization

3.8.2.1 Differential Thermal Analysis- Thermal Gravimetric Analysis (DTA-TGA)

Thermal analysis can provide information on chemical and physical changes in a sample, such as phase transitions, reductions, oxidations, and decompositions, as well as boiling, melting, and sublimation. Differential Thermal Analysis (DTA) can be used to study any process involving the absorption or evolution of heat. The DTA curve can also be used for qualitative identification of substances. In this study, thermal analysis was performed on ZnO, Y_2O_3, and YAG using a Shimadzu 60H Model Differential Thermal Analysis-Thermal Gravimetry. The analysis range was 25-1200°C and the heating rate was 10°C/min.

3.8.2.2 X-Ray Diffractometer (XRD)

X-ray diffraction (XRD) is a common technique used to identify and analyze the crystalline structure of materials such as powders and crystals. An XRD device produces X-rays that pass through a sample and are diffracted when they encounter the sample. The diffraction pattern that results is a map of the crystal's reciprocal lattice and can be used to determine the structure of the crystal using Bragg's law, which states that the diffraction angle is related to the spacing between lattice planes in the crystal. In this study, an XRD device was used to analyze the crystalline structure of the samples.

$$n.\,\lambda = 2.\,d.\,(\sin\theta) \qquad \text{Eq. (3.9)}$$

When considering a lattice with a spacing denoted by d, and an incident plane wave with a wave vector k making an angle θ with the lattice planes, along with a wavelength λ and an integer n representing the reflection order, this setup corresponds to the diffraction condition in reciprocal space. It also aligns with the Laue equations (Figure 3.10) (Callister & Rethwisch, 2007).

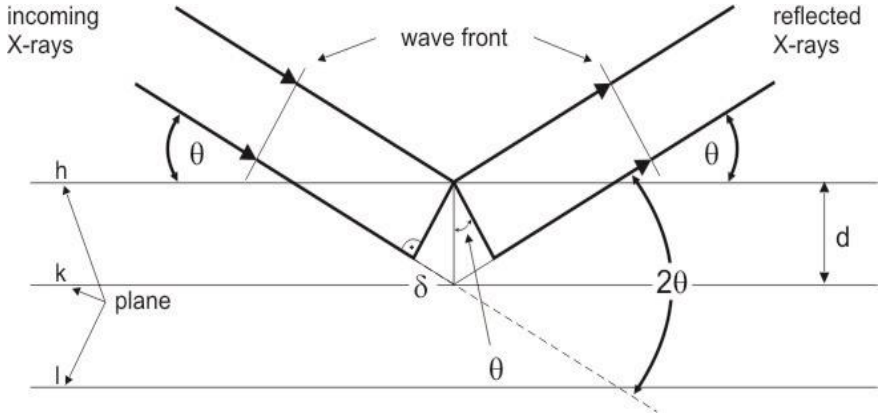


Figure 3.10 X-Ray Diffraction (Callister & Rethwisch, 2007)

The crystalline structure of ZnO, Y_2O_3, YAG particles and their composites was determined by using Rigaku, D/Max-2200/PC X-Ray diffractometer. X-Ray radiation with wavelength λ= 0.15418 nm of Cu Kα was set at 40 kV and 36 mA with a scanning speed of 2° 2θ/min, from 10° to 90°.

3.8.2.3 Scanning Electron Microscopy (SEM)

Scanning Electron Microscopy (SEM) is a high-resolution imaging technique used to examine the surface morphology and composition of solid specimens. Unlike optical microscopes, SEM uses a focused beam of high-energy electrons rather than visible light. This method allows for detailed imaging at much higher magnifications. SEM's high resolution and depth of field make it a valuable tool for precise surface analysis in research and industry, providing detailed information on specimen morphology and composition. In SEM, an electron gun generates and accelerates a beam of electrons, which is then focused and scanned across the specimen's surface. Various signals are produced as the beam interacts with the sample, including secondary and backscattered electrons. Secondary electrons, ejected from the specimen due to inelastic scattering, provide detailed images of surface topography with high resolution. These electrons originate from a few nanometers below the surface. Backscattered electrons, which result from elastic scattering, help highlight compositional differences in the sample. Heavier elements scatter these electrons more effectively, appearing brighter in the image. The collected signals are processed to produce images that reveal both surface details and compositional contrasts. SEM is used for analyzing materials, biological samples, and semiconductor devices, offering insights into surface structure and

chemical composition (Lawes, 1987). In our study Scanning Electron Microscope (FE-SEM) Gemini 500, Zeiss Corp is used

3.8.2.4 Brunauer–Emmett–Teller (BET)

The BET (Brunauer-Emmett-Teller) surface area measurement technique is a pivotal method in the field of surface science, providing a quantitative approach to assess the specific surface area of materials. Developed in 1938 by Brunauer, Emmett, and Teller, the technique is based on the adsorption of gas molecules onto a solid surface, with a primary focus on the formation of a monolayer. The cornerstone of the BET method is the BET equation, which relates the equilibrium pressure of the adsorptive gas to the quantity of gas required to form a complete monolayer. By analyzing the resulting adsorption isotherm data, researchers can extract crucial information about the monolayer capacity and the volume of gas adsorbed in a complete monolayer. This data is then utilized to calculate the specific surface area of the material (Brunauer, Emmett & Teller, 1938; Rouquerol, Rouquerol, Llewellyn, Maurin & Sing, 2013).

The plot of $\frac{1}{X}\left(\frac{P_0}{P}-1\right)$ versus P/P_0 is commonly known as a BET plot. This type of plot is derived from the BET equation, a fundamental equation in gas adsorption isotherm analysis, especially when studying monolayer adsorption on a solid surface. The specific form of the BET equation that leads to this plot is:

$$\frac{1}{X}\left(\frac{P_0}{P}-1\right)=\frac{1}{V_mC}\left(\frac{C-1}{V_mC}\right)\text{ x }P+\frac{C-1}{V_mC}$$

X is the weight of absorptive gas $\frac{P}{(V_m-V_B)P_0}$

P is the equilibrium pressure of the adsorptive gas.

P_0 is the saturation pressure of the gas.

V_m is the volume of gas adsorbed at monolayer coverage.

V_b is the volume of gas adsorbed in a complete monolayer.

C is a constant related to the energy of multilayer adsorption.

When you plot of $\frac{1}{X}\left(\frac{P_0}{P}-1\right)$ versus $P/P_{0,}$ the resulting graph is typically linear. The slope and y-intercept of this line can be used to extract important parameters from the BET equation, such as the monolayer capacity (V_m) and the constant (C). These parameters are essential for calculating the specific surface area of the material under investigation. Interpreting the BET plot is a crucial step in BET surface area analysis, and researchers can use the information derived from the plot to understand the adsorption behavior of gases on the material's surface and quantify its specific surface area (Brunauer et al., 1938).

3.8.3 Photocatalytic Characterization

Absorbance measurement methods were used in our study to perform photocatalytic performance testing. For this technique, the chosen pollutant should exhibit distinct absorbance peaks in the UV-visible spectrum, facilitating easy concentration monitoring. We used methylene blue (MB) solutions, which have distinct absorbance peaks at 663 nm. It is needed to prepare a photocatalyst suspension in a solvent or aqueous solution, optimizing its concentration based on experimental conditions and assay sensitivity. The organic pollutant is dissolved to create a stock solution of known concentration, which is then diluted to the desired initial concentration for the photocatalytic test. The experiment is set up by transferring a measured volume of the pollutant solution into a reaction vessel, typically a quartz cuvette, for UV-visible spectroscopy, ensuring the light path is perpendicular to the incident light. A baseline absorbance spectrum of the pollutant solution is recorded to establish a reference point. The reaction vessel containing the pollutant solution is then illuminated with an appropriate light source, such as UV lamps, solar simulators, or LEDs, matching the absorption spectrum of the photocatalyst and the pollutant.

The photocatalytic tests of the materials were carried out in a custom-designed reactor containing a MB solution and illuminated with UV light from an Osram UltraVitalux E27 (300 W) light source starting with a 10^{-5} M concentration of MB and an absorbance value of 0.754. The photocatalytic materials were submerged in beakers of MB solution and stirred vigorously in the dark to allow adsorption-desorption equilibrium between the dye and the catalyst surface. The light source was positioned

at a consistent 30 cm distance from each beaker in all experiments. Once equilibrium was reached, the UV light source was activated to irradiate the photocatalytic materials-MB solution.

At specific intervals during irradiation, samples were collected by centrifuging at 5000 rpm for 10 minutes to separate the catalyst from the solution. 3 ml of the MB solution was extracted for absorbance measurements using a Shimadzu UV-1240 spectrophotometer, focusing on the MB's characteristic peak at 663 nm. These absorption measurements provided a detailed assessment of the photodegradation process over time. Absorbance values were converted to concentration values using the Beer-Lambert law, which assumes a linear relationship between absorbance and concentration in dilute MB solutions (Fernández-Pérez & Marbán, 2022; Li Puma & Brucato, 2007).

The photocatalytic efficiency was calculated using the formula $[(C_0 - C)/C_0] \times 100$, where C_0 represents the initial MB concentration and C represents the concentration after UV exposure. This calculation provides a clear measure of the composite's effectiveness in breaking down MB, essential for evaluating the catalyst's potential for device integration and industrial-scale applications.

Control experiments, including dark control experiments and blank experiments, were performed to validate photocatalytic activity and exclude interfering factors. Experimental parameters, such as catalyst loading, light intensity, and solution pH, are optimized to maximize photocatalytic efficiency. Results are validated through reproducibility tests and comparison with literature data or standard references, enabling researchers to assess photocatalytic effectiveness in degrading organic pollutants and understand underlying reaction mechanisms.

3.8.4 Photoluminescence Characterization

Photoluminescence is a technique used to study the emission of light from a material after it has absorbed photons. When a substance absorbs electromagnetic radiation, it excites electrons to a higher energy state. As these electrons return to their ground state, they emit light, which can be measured to provide information about the material's electronic structure and properties. This emission, known as

photoluminescence, is commonly used in materials science, chemistry, and biology to analyze semiconductors, organic compounds, and biological molecules. The process begins by exciting the sample with a light source, typically ultraviolet or visible light. This light source provides the necessary energy to elevate electrons in the sample to higher energy levels. After excitation, the electrons eventually return to their ground state, releasing energy in the form of light. This emitted light is known as photoluminescence. The wavelength and intensity of this emitted light provide insights into the sample's properties. The emitted light is collected and analyzed using a spectrometer (Kulmala & Suomi, 2003; Shinde et al., 2012). This analysis involves measuring the intensity of light as a function of wavelength, which helps to identify various characteristics of the sample. In our study, Edinburgh Instruments FLS920 was employed for Photoluminescence Analysis. This device is a sophisticated photoluminescence spectrometer designed for detailed analysis of luminescent materials.

The FLS920 uses high-intensity light sources, such as Xenon lamps or solid-state lasers, to provide the excitation energy required for photoluminescence. The choice of excitation source can be tailored to match the specific requirements of the sample under investigation. The instrument is equipped with monochromators or optical filters that select specific wavelengths of light for excitation and detection. This allows for precise control over the excitation and emission wavelengths, ensuring accurate measurement of the photoluminescence. The emitted light is collected by a sensitive detector, such as a photomultiplier tube or a charge-coupled device. The detector measures the intensity of the emitted light and converts it into an electrical signal, which is then analyzed to produce a photoluminescence spectrum.

CHAPTER FOUR
RESULTS AND DISCUSSION

4.1 Structural Characterization of ZnO Nanoparticles

To optimize the production parameters and understand the synthesis processes, various analyses were conducted at different stages of ZnO nanoparticle production process. Figure 4.1 presents the TG-DTA curves for the dried ZnO gel, revealing a distinct thermal phenomenon. The analysis shows an initial weight loss of 31%, which is primarily due to the evaporation of solvents such as ethanol and moisture, along with the decomposition of zinc oxalate complexes. This transformation occurs between 200 and 300 °C, where these complexes convert to zinc hydroxide. As the temperature rises between 360 and 460 °C, a subsequent weight loss is observed, indicating the decomposition of zinc hydroxide and the formation of ZnO. (Ba-Abbad, Kadhum, Bakar Mohamad, Takriff & Sopian, 2013; Demirci et al., 2020; Yang, Wang, Tang, Wang & Zhang, 2005)

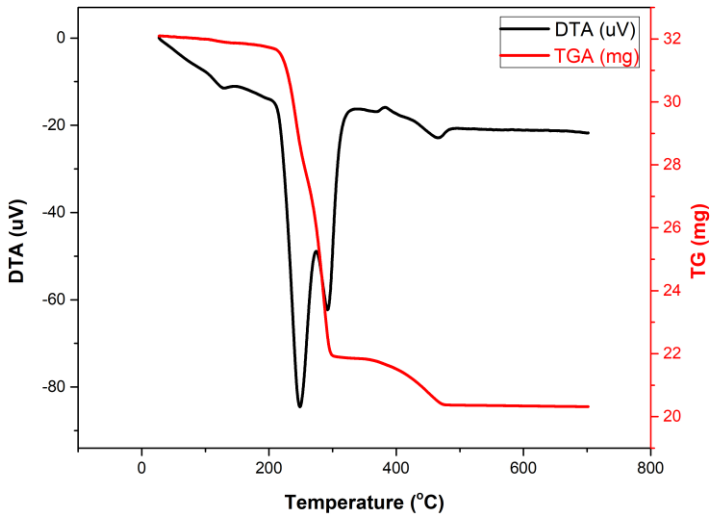


Figure 4.1 DTA-TG analysis of dried ZnO xerogel powders

FTIR spectra of dried ZnO xerogel was showed in Figure 4.2. Peak observed around 3000-3500 cm^{-1} is indicative of the stretching vibrations of hydroxyl groups. In sol-gel derived ZnO, this peak often represents hydroxyl groups that are either physically adsorbed on the surface or incorporated within the gel network due to residual water or incomplete hydrolysis of precursors.

The broad band around 3400 - 3500 cm^{-1} indicates the presence of O-H stretching from water or hydroxyl groups (Lopez, Sanchez, Bosch, Meas & Gomez, 1992; Sammon et al., 1998). Stretching vibration of H-O-H absorption peaks appeared at about 1650 cm^{-1}(Ma & Wu, 2023) Peaks in regions between 1000 - 1500 cm^{-1} could correspond to C-H bending vibrations or C-O stretching vibrations from residual organic compounds (Amoriello, Bianco, Eusebio & Gronchi, 2011; Lopez et al., 1992). The presence of carbonate groups can be indicated by around 1350 - 1500 cm^{-1}(Dobson & McQuillan, 1997; López, Bosch, Asomoza, Gómez & Ramos, 1997). They can form if CO_2 from the air reacts with the ZnO precursors or intermediates.

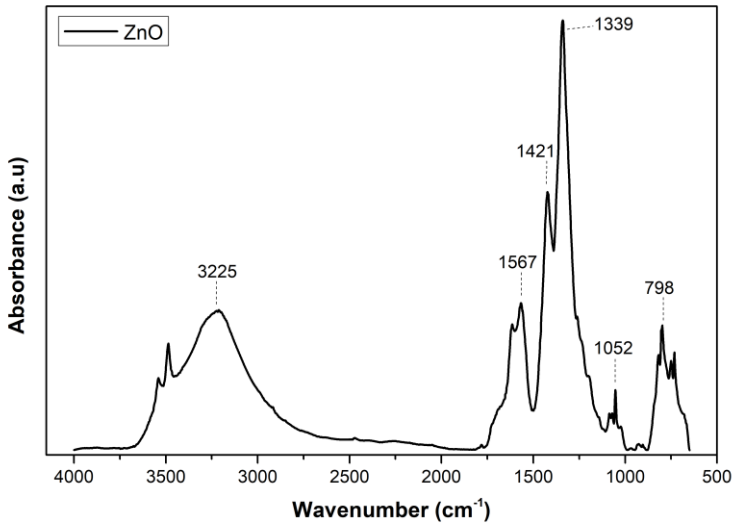


Figure 4.2 FTIR spectra of dried ZnO xerogel

The XRD pattern of pure ZnO was illustrated in Figure 4.3, displays distinct diffraction peaks characterized by strong intensity and clarity. These peaks are attributed solely to the hexagonal wurtzite structure of ZnO (JCPDS 01-079-0206, P63mc), confirming the lack of any additional phases (Dobrozhan et al., 2024; Lahewil, Zyoud, Ahmed, Omar & Azman, 2022). Notably, the diffraction peaks appear at 2θ values of 31.72º, 34.43º, 36.32º, 47.64º, 56.67º, 62.99º, 66.47º, 68.01º, 69.13º, 72.58º, 77.62º, 81.48º, and 89.64º, corresponding to various crystal planes including (100), (002), (101), (102), (110), (103), (200), (112), (201), (004), (202), (104), and (203). Among these, the peak at 2θ = 36.32º, associated to the (101) plane, stands out with the highest intensity, indicating its role as a prominent feature in the synthesized ZnO material.

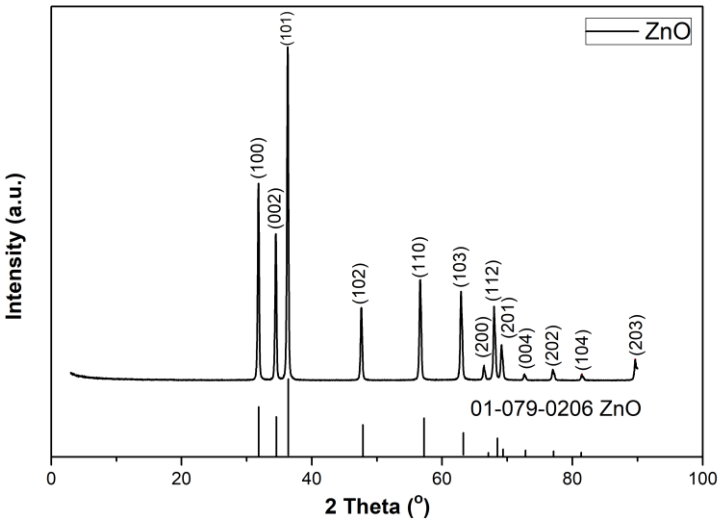


Figure 4.3 XRD pattern of ZnO nanoparticles

Figure 4.4 displays SEM images of ZnO nanoparticles, which show a range of shapes, including rounded, granular and spherical, along with occasional larger particles. The particles are distributed within a size range of 50 nm to 300 nm. Unlike Y_2O_3 particles, ZnO nanoparticles have a more rounded and oval structure. Since no esterification reaction occurs during the production of ZnO, it is expected that the final particle shape would differ from that of Y_2O_3.

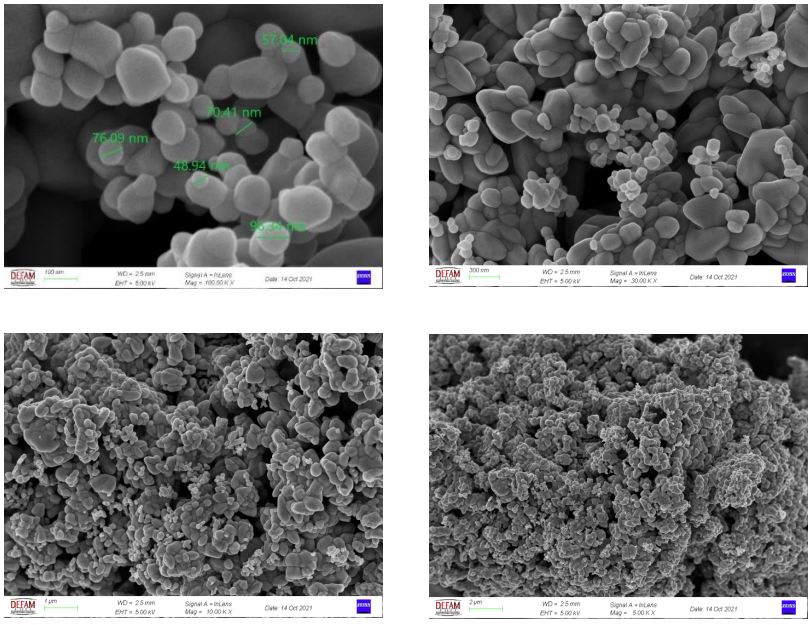


Figure 4.4 SEM micrographs of pure ZnO

4.2 Structural Characterization of Y_2O_3 powders

To better understand and optimize the processes during the synthesis stage, the prepared samples were analyzed at various stages using several techniques such as DTA, FTIR, XRD, SEM, and BET. The results of these analyses are presented in the following sections.

Figure 4.5 depicts the DTA-TG curves for the Y_2O_3 powder xerogel. The thermal analysis reveals an initial weight loss of about 8% occurring between 100 and 200 °C, which is likely due to the evaporation of water molecules adsorbed during the esterification process. This is followed by a significant weight reduction, approximately 50%, between 250 and 500 °C. This substantial loss can be attributed to the combustion of organic substances, including citric acid, and the breakdown of ethylene glycol within the polymeric structure (S. Ghorbani, R. Shoja Razavi, M. R. Loghman-Estarki & A. Alhaji, 2017; Keyvani, Bahamirian & Esmaeili, 2020). An exothermic peak at 600 °C signifies a phase transformation of Y_2O_3. To ensure thorough crystallization and achieve a more crystalline structure, the heat treatment was extended to 1000 °C, as supported by literature suggesting that temperatures above 600 °C enhance crystallinity in the resulting material. (Boukerika & Guerbous, 2014; Zhang, Zhang, Tang, Lin & Zheng, 2002).

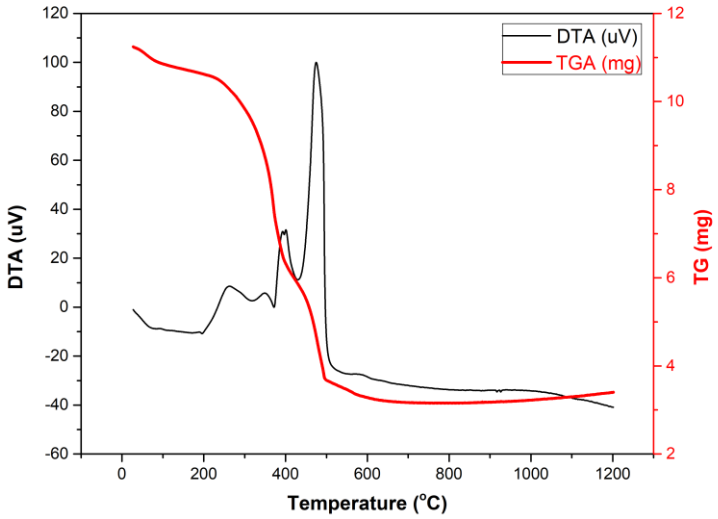


Figure 4.5 DTA-TG analysis of dried Y_2O_3 xerogel powders

Optimization studies were carried out for Y_2O_3 and its Eu doped samples in terms of efficient use of consumables. Therefore, firstly different amounts of acid were used during production to determine the optimum acid concentration. After the optimum acid concentration was determined, the following material synthesis was carried out with those parameters. Figure 4.6 displays the FTIR spectra of Y_2O_3 xerogels produced with 3 different acid concentrations (0.5, 1 and 2 MRCM). Within the spectra, a broad band located around 3400 cm^{-1} was observed, indicating the O-H stretching of adsorbed water. The amorphous sample shows two bands at 2924 and 2903 cm^{-1}, which correspond to the asymmetric and symmetric stretching of $-CH_2$ (Guo, Zhang, Lou, Brioude & Mugnier, 2004). Most importantly, the peaks present around 1420-1700 cm^{-1} could be associated with the asymmetric and symmetric stretching vibrations of COO^-. This could be interpreted as proof of the formation of complexes of citric acid cations (S. Ghorbani et al., 2017). The intensity of peaks present around 1420-1500 cm^{-1} increased with increasing citric acid.

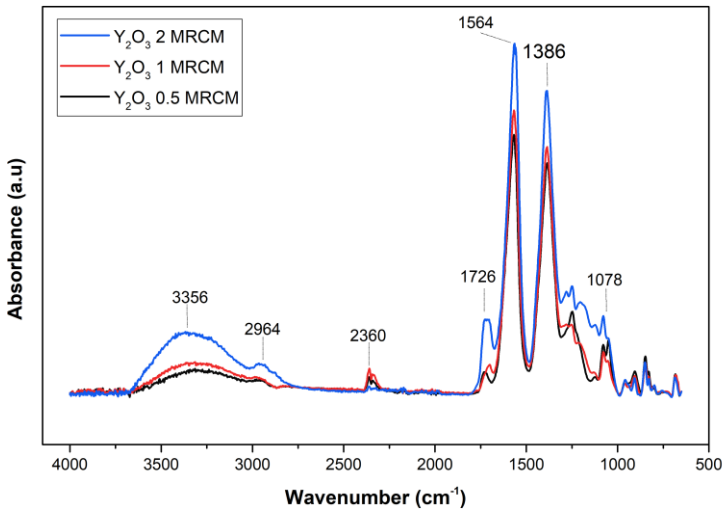


Figure 4.6 FTIR spectra of dried Y_2O_3 gel with different acid concentration

XRD patterns of Y_2O_3 with 0.5, 1 and 2 MRCM are illustrated in Figure 4.7. It has been observed that variations in acid concentration do not result in significant changes to the crystal structure of Y_2O_3. The XRD patterns of Y_2O_3 samples produced with different acid concentrations are nearly identical. However, it is important to note that XRD analysis does not provide information about the surface morphology of the

material. The implications of changes in acid concentration will be discussed in subsequent sections.

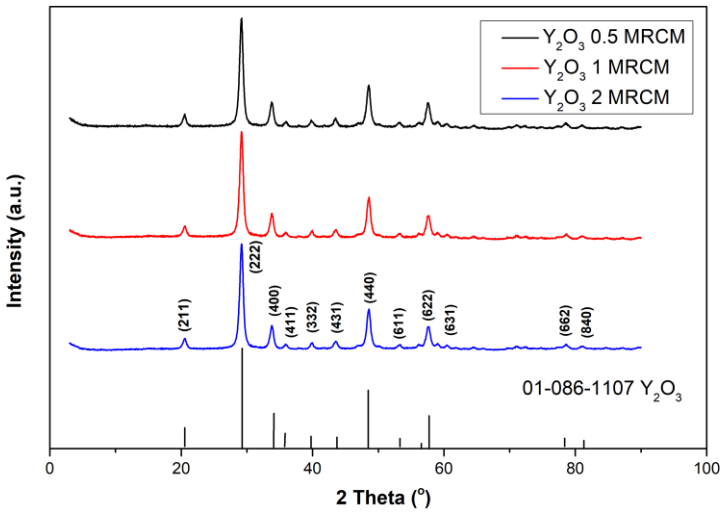


Figure 4.7 XRD patterns of Y_2O_3 with 0.5, 1 and 2 MRCM

Planes of (211), (222), (400), (411), (332), (431), (440), (611), (622), (631), (662) and (840) of Y_2O_3 corresponded by peaks are observed at 20.58°, 29.22°, 33.82°, 35.86°, 39.98°, 43.54°, 48.58°, 53.38°, 57.68°, 59.06°, 78.70° and 81. 02° respectively showed in Figure 4.7. The peak at $2\theta = 29.22°$ with (222) plane had the highest intensity, which is the main peak for all the samples. All diffraction peaks are attributed to the pure body-centered cubic (bcc) structure for Y_2O_3. It is worthwhile to note that there was no remarkable change in terms of the intensity of produced doped and pure Y_2O_3 particles. This result is also matched with pdf card number 01-086-1107 with space group Ia-3 (Aleshin et al., 2023; Mendoza-Núñez et al., 2022). There are no other impurity phases for any samples. Additionally, no difference was observed in the peak intensities due to the different acid concentrations.

After the optimum acid concentration (2 MRCM) was determined, samples with different amounts of Eu doped were produced and their characterizations were carried out. Figure 4.8 (a) presents the XRD pattern of both pure and Eu-doped Y_2O_3 materials. It can be observed that the Eu doping process does not induce a phase transition. However, as shown in Figure 4.8 (b), a shift to the left in the peak corresponding to the (222) plane at $2\theta = 29.22°$ occurs, which is attributed to the distortion of the crystal

lattice caused by the increasing concentration of Eu dopant. This shift is due to the altered distance between atomic layers within the lattice. The primary cause of this shift is the fact that the atomic radius of Eu is slightly larger than that of the Y atom. (Khachatourian et al., 2016; Kumar, Pal, Herrera & Mathew, 2016)

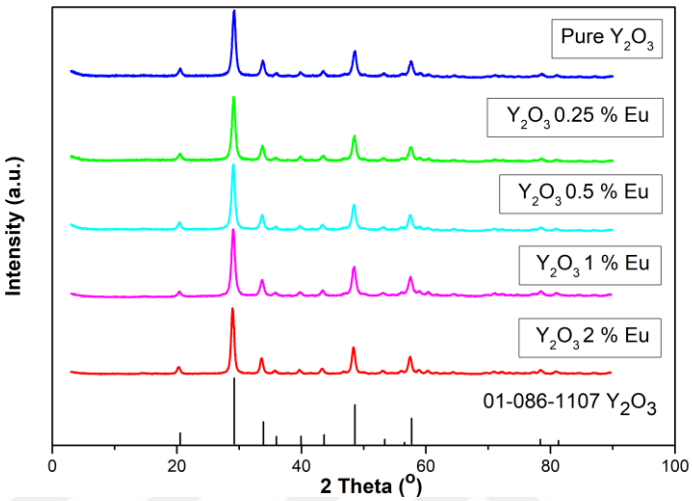


Figure 4.8 (a) XRD patterns of pure and Eu doped Y_2O_3

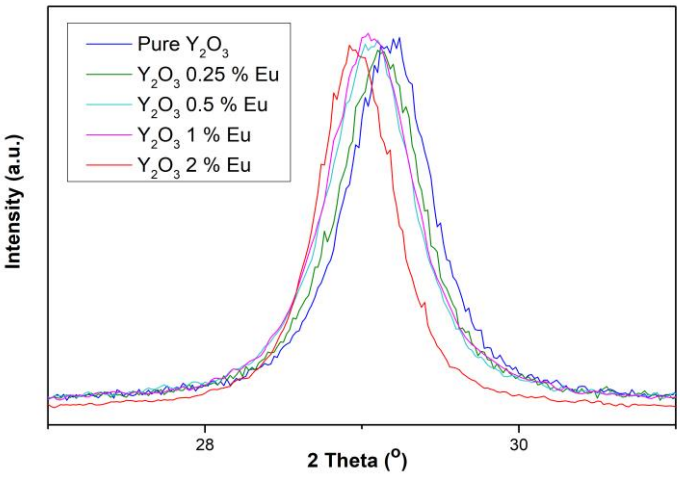


Figure 4.8 (b) Detailed XRD patterns of pure and Eu doped Y_2O_3

For comparison purposes, Ce doped Y_2O_3 was synthesized following the same parameters used for the production of Eu doped Y_2O_3. As discussed in later sections of this study, it was observed that higher doping concentrations did not lead to increased efficiency; therefore, a 1% concentration was selected for Ce doping. Figure 4.9 presents the XRD analysis results for pure Y_2O_3, 1% Eu doped Y_2O_3, and 1% Ce

doped Y_2O_3. For comparison, the XRD results of both pure and Eu doped samples have been added to the graph. Post-heat treatment, no additional phases appeared, indicating that Ce doping did not induce any structural changes in the Y_2O_3 crystal lattice.

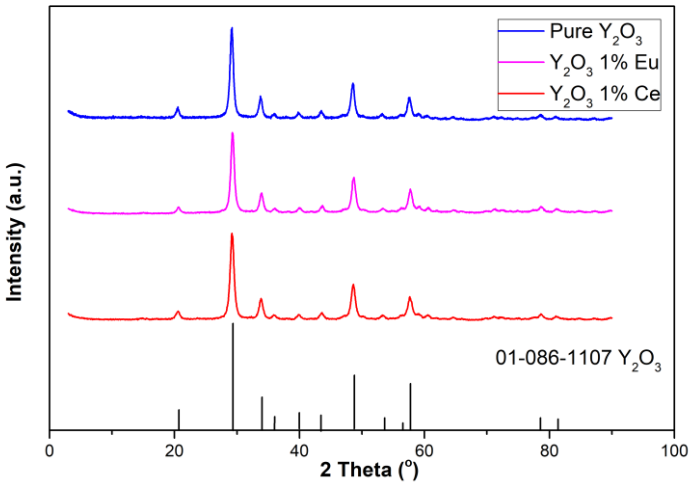


Figure 4.9 XRD patterns of pure, 1% Eu and 1% Ce doped Y_2O_3

Electron microscopy analyses were conducted to observe the morphology and grain structure of Y_2O_3. Figures 4.10, 4.11 and 4.12 display the SEM images of Y_2O_3 materials produced with parameters of 0.5 MRCM, 1 MRCM, and 2 MRCM, respectively. As evidenced by the images, materials synthesized with higher acid levels exhibit thinner, more distinct, plate-like structures, indicating an increase in surface area with acid concentration. This increase is likely because of the esterification reaction between ethylene glycol (EG) and citric acid (CA), which depends on factors such as the specific composition of the reaction mixture, reactant concentrations, reaction temperature, and catalyst presence.

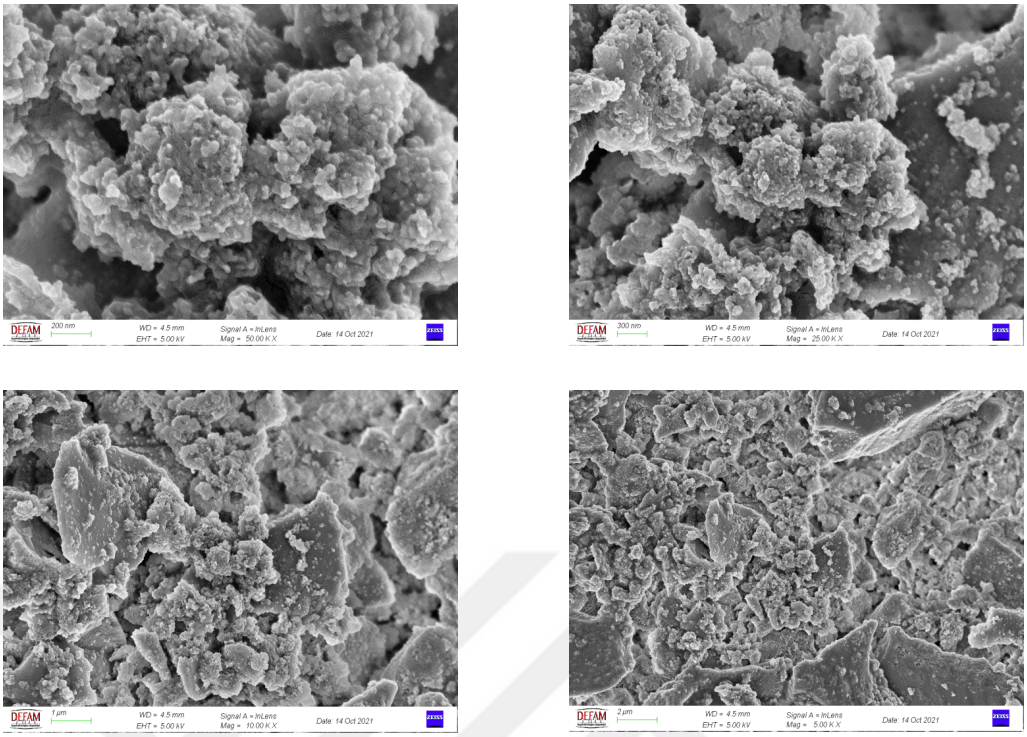


Figure 4.10 SEM micrographs of Y_2O_3 0.5 MRCM

Metal ions readily form stable chelating complexes with CA, which are further stabilized when EG is present. EG, with its two alcoholic hydroxyl (-OH) groups, exhibits a strong affinity for complexing with metal ions (S. Ghorbani et al., 2017). The reaction between citric acid and ethylene glycol yields a complex product mixture, including esters, glycols, and water. Esterification occurs as a chemical reaction between the hydroxyl group of ethylene glycol (-OH) and the carboxyl group of citric acid (-COOH), resulting in ester and water formation (Park, Lee, Lee & Kang, 2014).

Y_2O_3 particles are clearly different from ZnO particles in appearance, which is represented in the previous section. Unlike the spherical shape of ZnO, the Y_2O_3 particles are characterized by a flat, layered, and angular structure. This morphology is not a drawback, but rather a result of the esterification process between CA and EG during synthesis. The expansion that occurs during esterification leads to the formation of a porous structure with low density, thin walls and an increased surface area. In our photocatalytic setup, the high surface area of Y_2O_3 plays a crucial role in boosting the activity of ZnO, thereby enhancing its catalytic performance.

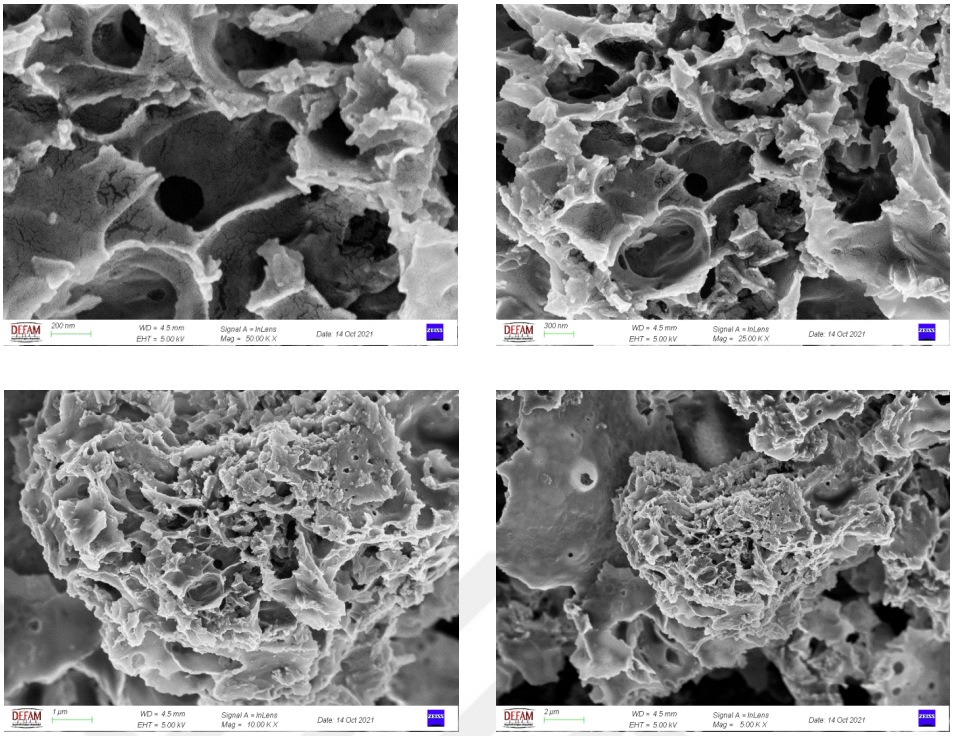


Figure 4.11 SEM micrographs of Y_2O_3 1 MRCM

The images obtained from SEM analysis are consistent with the surface area (BET) analysis results, showing that increasing the acid amount during synthesis correlates with a greater surface area in the final product. The volumetric expansion observed during drying also explains the surface area increase in the material. Figure 4.13 illustrates the post-drying states of materials synthesized with three different acid concentrations at 200 ^{o}C. A marked volumetric expansion is evident with higher acid amounts, which can be attributed to the esterification reaction discussed above.

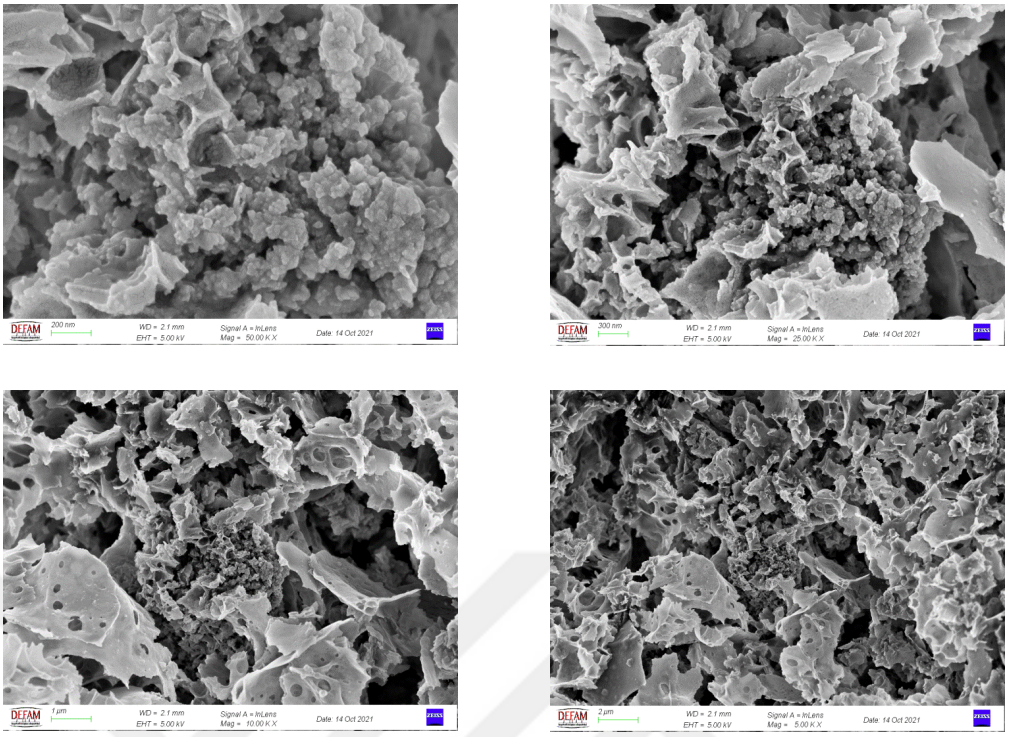


Figure 4.12 SEM micrographs of Y_2O_3 2 MRCM

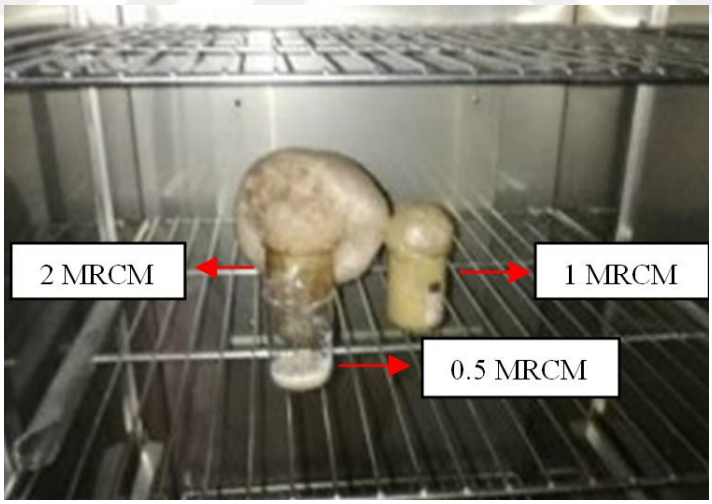


Figure 4.13 Post-drying states of Y2O3 materials synthesized with three different acid concentrations

Brunauer-Emmett-Teller (BET) analysis was carried out to investigate how the concentration of citric acid used during the solution preparation affects the morphology and surface area of the final product. 2 mg of Y_2O_3 with 0.5, 1 and 2 MRCM powder was weighted individually. Evacuation rate 60 set mmHg/min

Equilibration time was 10 s. The surface area of synthesized Y_2O_3 powders was measured by the Brunauer-Emmett-Teller (BET) method and analyzed using nitrogen adsorption in a Micromeritics Gemini 2390T. Prior to the analysis, the samples were degassed at 30°C. The BET surface area was determined by using the multipoint BET method, based on the adsorption data in the range of relative pressure (P/P_0) between 0.05 and 0.2 mg powder was weighted for each sample, evacuation rate 60 set mmHg/min, and equilibration time was 10 s for measurements.

It's necessary to consider the linearity of the isotherm and the interaction between the adsorbent and adsorbate to obtain the surface area from a gas adsorption isotherm, In the case of SBET, the correlation coefficient of the BET transform plot is used as a reference, which is calculated by performing linear regression over the range of relative pressures applied to the data. Figure 4.14 shows BET transform plots of samples degassed at 30 °C. A correlation coefficient of greater than 0.999 is considered sufficient for a suitably linear transform plot within the selected range of relative pressures (Lapham & Lapham, 2019). In our study, the minimum correlation coefficient was 0.9999944.

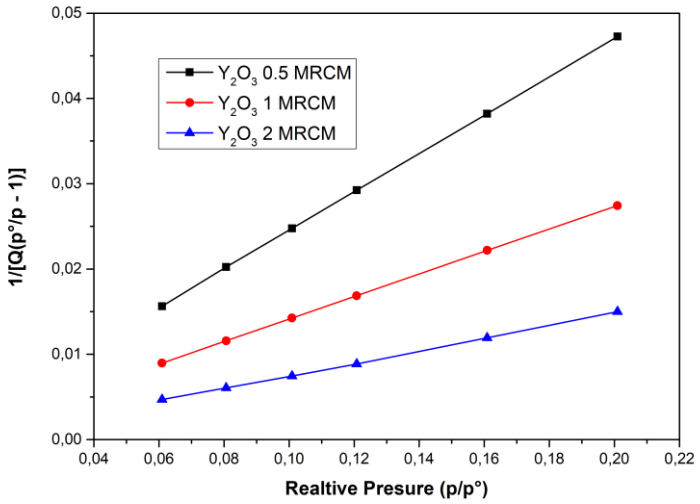


Figure 4.14 BET transform plot of Y_2O_3 with 0.5, 1 and 2 MRCM

As seen in Figure 4.15 the amount of adsorbed gas increases with increasing relative gas pressure (p/p^o) for all three samples. The adsorbed gas amounts for Y_2O_3 with 0.5, 1 and 2 MRCM samples at 0.10 p/p^o are 4.53, 7.86 and 12.82, respectively. This result showed that the amount of gas adsorbed by the samples increased due to the increase

in the amount of acid used during synthesis. Thus, it can be said that the surface area also increases with the increasing amount of acid. We think that this is the result of an esterification reaction between citric acid and ethylene glycol. The specific composition of the reaction mixture depends on several factors such as the concentration of the reactants, the reaction temperature, and the presence of catalysts. Metal ions can form highly stable chelating complexes with CA, and these metal-CA complexes can be further strengthened in the presence of EG, which has two alcoholic hydroxyl functional groups (-OH) that possess a strong affinity for complexation with the metal ions (S Ghorbani, R Shoja Razavi, MR Loghman-Estarki & A Alhaji, 2017; S. Ghorbani et al., 2017). The reaction between EG and CA results in the formation of a complex mixture of products that include esters, glycols and water. Esterification is a chemical reaction between the hydroxyl group of EG and a carboxyl group of CA that results in the formation of an ester and water (Park et al., 2014).

Thanks to the swelling that occurs during the esterification reaction, the volume of the starting materials in the xerogel form increases. It is worth noting that the swelling observed during the reaction is not necessarily a negative outcome. In fact, swelling can be a desirable characteristic for some applications. As a result, Y_2O_3 particles with a larger surface area are formed. During the reaction, the CA and EG monomers react to form ester bonds, which link the monomers together to form a polymer. As the polymer chains grow, they become increasingly soluble in the ethylene glycol solvent, leading to the observed swelling. Additionally, the reaction may also generate heat, which can further contribute to swelling (S Ghorbani et al., 2017; S. Ghorbani et al., 2017).

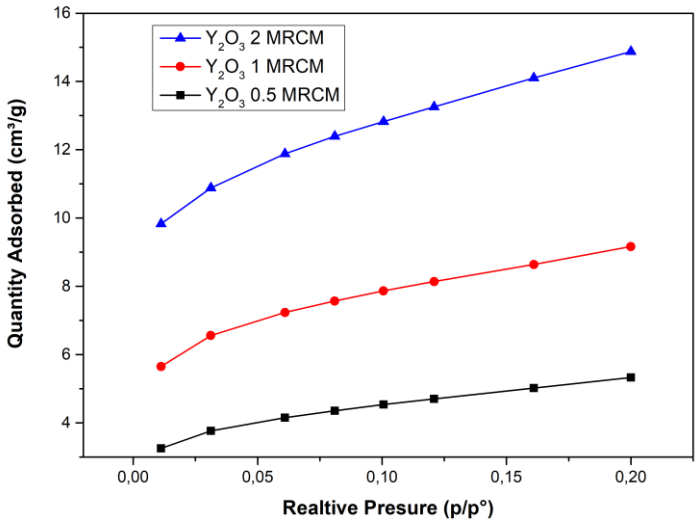


Figure 4.15 Isotherm Linear plot of Y_2O_3 with 0.5, 1 and 2 MRCM

Table 4.1 gives the molar ratios of citric acid concentration to the total metal ions (MRCM) in each sample solution and their BET surface areas. According to the results obtained from the graphs above, the BET surface area of Y_2O_3 0.5 sample was 19.1648 m^2/g, while this value was 32.7610 and 53.4836 m^2/g for Y_2O_3 1 and Y_2O_3 2 samples, respectively. The surface area increased with increasing acid concentration.

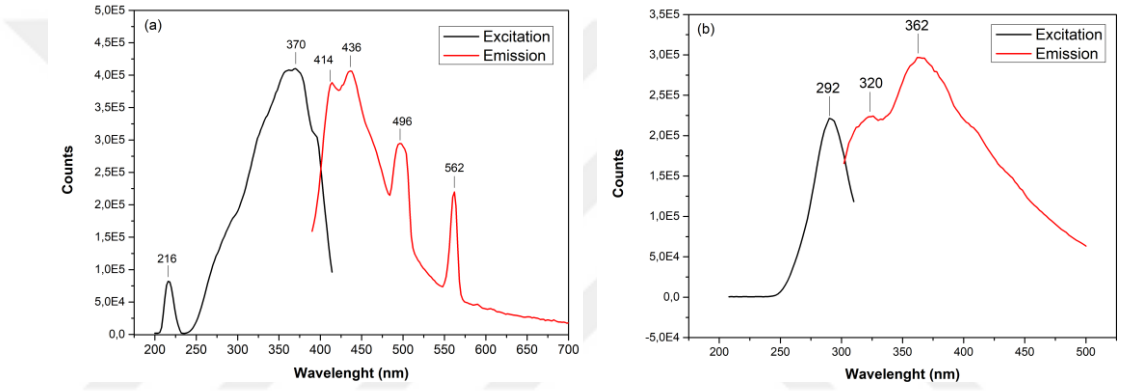
Table 4.1 BET surface area of each sample prepared with different acid concentrations.

Sample	MRCM	BET Surface area (m^2/g)
Y_2O_3 0.5	0.005/0.01	19.1648
Y_2O_3 1	0.01/0.01	32.7610
Y_2O_3 2	0.02/0.01	53.4836

4.3 Luminescent Characterization of Y_2O_3 powders

Y_2O_3 material radiates at different wavelengths depending on the wavelength at which it is excited. In this context, luminescence measurement studies have started to determine the excitation wavelength that gives the most suitable emission wavelength. The luminescence of Y_2O_3 varies with the excitation wavelength, prompting measurements to identify the optimal excitation wavelength for maximum emission. Figure 4.16 (a) and (b) illustrate the excitation and emission spectra of pure Y_2O_3,

λ_{max}^{ex}:370 nm and λ_{max}^{ex}:292 nm respectively. Exciting Y_2O_3 at 370 nm results in emissions at 414, 436, 496, and 562 nm. While these emission wavelengths indicate that Y_2O_3 exhibits strong luminescence, they do not align well with the requirements of our specific setup. In our research, it is vital that the luminescence of the material can effectively excite ZnO. This ability is key to enhancing the photocatalytic performance of ZnO. When Y_2O_3 is excited with light at 292 nm, it exhibits its strongest luminescence at 362 nm and relatively weaker intensity at 320 nm. This emission spectrum is particularly well suited for exciting photocatalytic ZnO. Given this promising finding, we proceeded with further investigations in this concept.



(a) (b)

Figure 4.16 Excitation and emission spectrum of pure Y_2O_3 (a); λ_{max}^{ex}:370 nm, λ_m (b) λ_{max}^{ex}:292 nm

Figure 4.17 (a) and (b) display the spectrum of Eu doped Y_2O_3 when excited at 370 nm and 292 nm, respectively. In contrast to pure Y_2O_3, 1% Eu doped Y_2O_3 is not suitable for photocatalytic studies. When excited at 370 nm, it shows distinct emission at different wavelengths. Intense emission at 612 nm corresponds to the $^5D_0 \rightarrow ^7F_2$ transition of Eu^{+3}. It gives a bright red emission and is the signature peak for Y_2O_3; Eu^{+3}. Emission at 628 is also assigned $^5D_0 \rightarrow ^7F_2$ transition. Emission at 595 nm comes from $^5D_0 \rightarrow ^7F_1$ transition (Boukerika & Guerbous, 2014; de Andrade Gomes, Ernesto Giroldo Valerio & Soares Macedo, 2011; Lamiri, Guerbous, Samah, Boukerika & Ouhenia, 2015). While these emissions are advantageous for certain applications, they are not favorable for photocatalytic effectiveness in our research. When Y_2O_3;Eu^{+3} was excited at 292 nm (optimum excitation wavelength for pure Y_2O_3) the results deteriorated, leading to the disappearance of the previously observed emissions. A

distinct excitation peak is also observed at 216 nm; however, we did not focus on this excitation wavelength. The primary goal of our study is to enhance the efficiency of ZnO as a photocatalytic material under daylight conditions. Since the 216 nm wavelength is not present in the daylight spectrum, excitation studies at this wavelength were not conducted (Stamnes, 2003; Wang & Yu, 2023). Consequently, Eu doping was not found to have a beneficial effect on Y_2O_3.

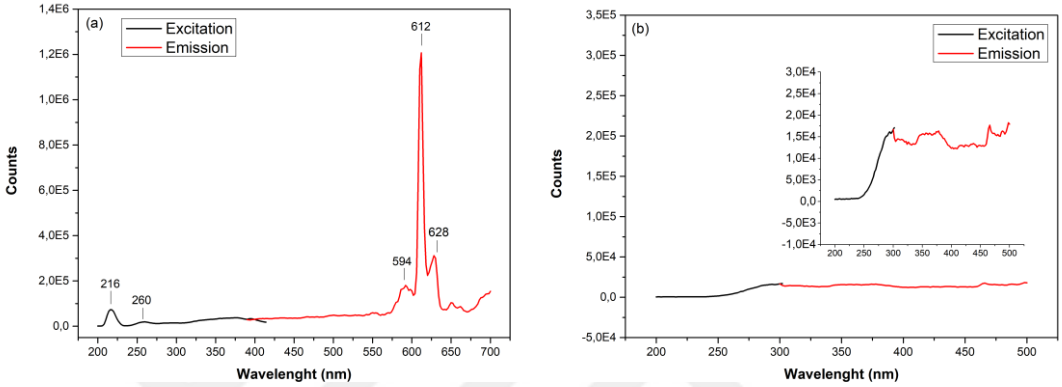


Figure 4.17 Excitation and emission spectrum of Eu doped Y_2O_3 (a); λex:370 nm, (b) λex:292 nm

Figure 4.18 (a) and (b) displays the luminescence spectrum of 1% Ce doped Y_2O_3 when excited at 380 nm and 292 nm respectively. The luminescence results for Ce doped Y_2O_3 indicated that doping did not produce a positive effect. The excitation and luminescence spectra differ due to the distinct nature of the dopant. Notably, there is a very strong excitation peak at 216 nm. However, since this wavelength is not present in the daylight spectrum, further photocatalytic studies would be ineffective (Stamnes, 2003; Wang & Yu, 2023). As a result, we did not focus on excitation studies at this wavelength.

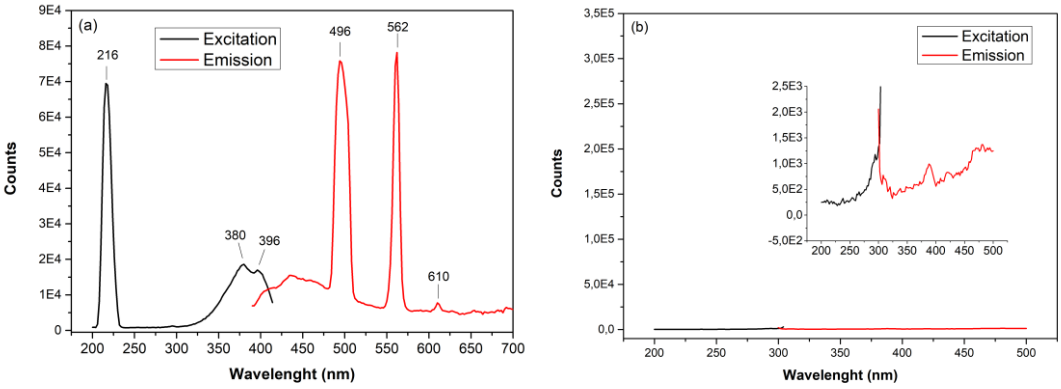


Figure 4.18 Excitation and emission spectrum of Ce doped Y_2O_3 (a); λ_{ex}:380 nm, (b) λ_{ex}:292 nm

4.4 Structural Characterization of ZnO-Y_2O_3 Composite Produced by Mechanical Mixing

As mentioned in the experimental section, since the composite ZnO-Y_2O_3 structure was obtained through mechanical mixing, DTA and FTIR analyses were not performed for the composite materials during the synthesis phase.

Figure 4.19 (a) displays the XRD patterns of a composite structure composed of ZnO and varying weight percentages of Y_2O_3. Notably, the composite with the highest Y_2O_3 content consists of only 20% by weight, while the lowest contains just 2.5% Y_2O_3. Given this minimal amount, the Y_2O_3 presence in the XRD pattern for the 2.5% composite is almost undetectable on a larger scale. However, Figure 4.19 (b) shows a detailed XRD pattern of ZnO-2.5Y_2O_3 between 20-40 2θ degrees. The content of Y_2O_3 can easily be distinguished in a detailed pattern. As the Y_2O_3 content increases beyond 10%, the primary peak at 2θ = 29.22° becomes significantly more pronounced. The characteristic peaks of ZnO, which are predominant in the composite, remain clearly visible, indicating that neither ZnO nor Y_2O_3 has experienced any phase transitions. This suggests that both materials remain homogeneously mixed within the composite structure.

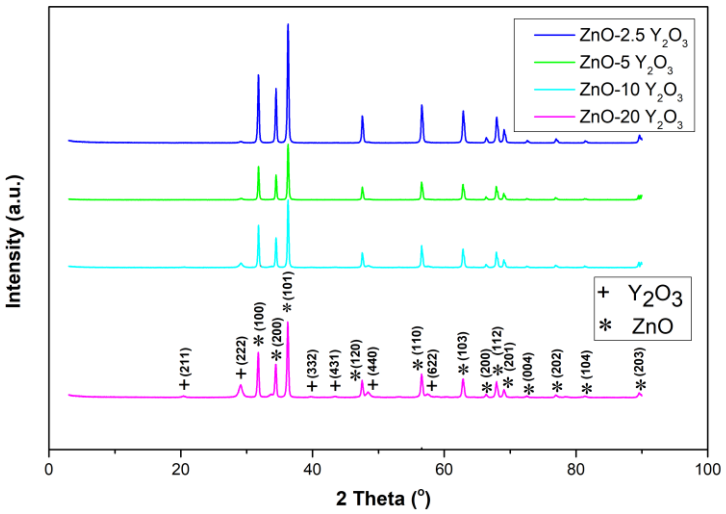


Figure 4.19 (a) XRD pattern of composite ZnO-Y_2O_3

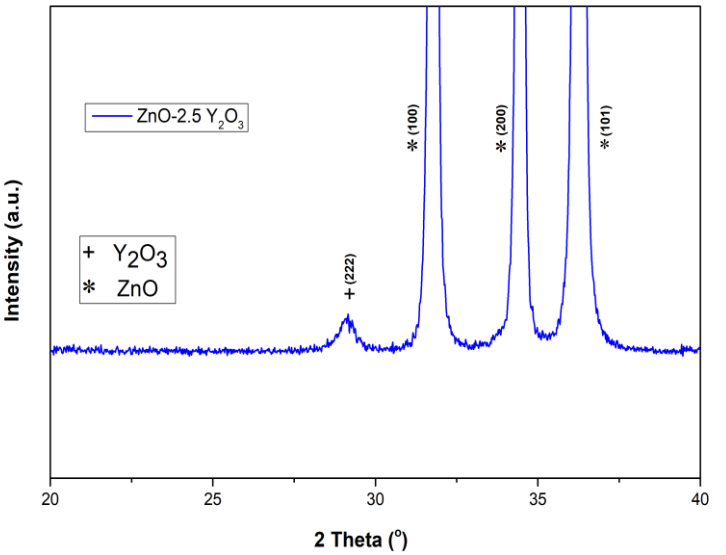


Figure 4.19 (b) Detailed XRD pattern of composite ZnO-2.5Y_2O_3

SEM and mapping analysis were conducted for each composite ZnO-Y_2O_3 sample, as depicted in Figure 4.20. In these images, the Y component of the composite is depicted in yellow, Zn is shown in green, and O is represented in blue. It is observed that as the amount of Y increases from ZnO-2.5Y_2O_3 to ZnO-20Y_2O_3, there is a corresponding decrease in the amount of Zn. Additionally, Figure 4.21 shows the region marked with a red square, which indicates the area where the elemental analysis was conducted. This analysis reveals that the plate-like structures are primarily

composed of Y_2O_3, while the rounded spherical structures correspond to ZnO, confirming the distinct composition of the materials within the composite. When comparing data from mapping images with the XRD results, it was observed that the information obtained from both techniques is in agreement. Both analytical methods confirmed the presence of increasing Y_2O_3 content within the ZnO-Y_2O_3 composite structure.

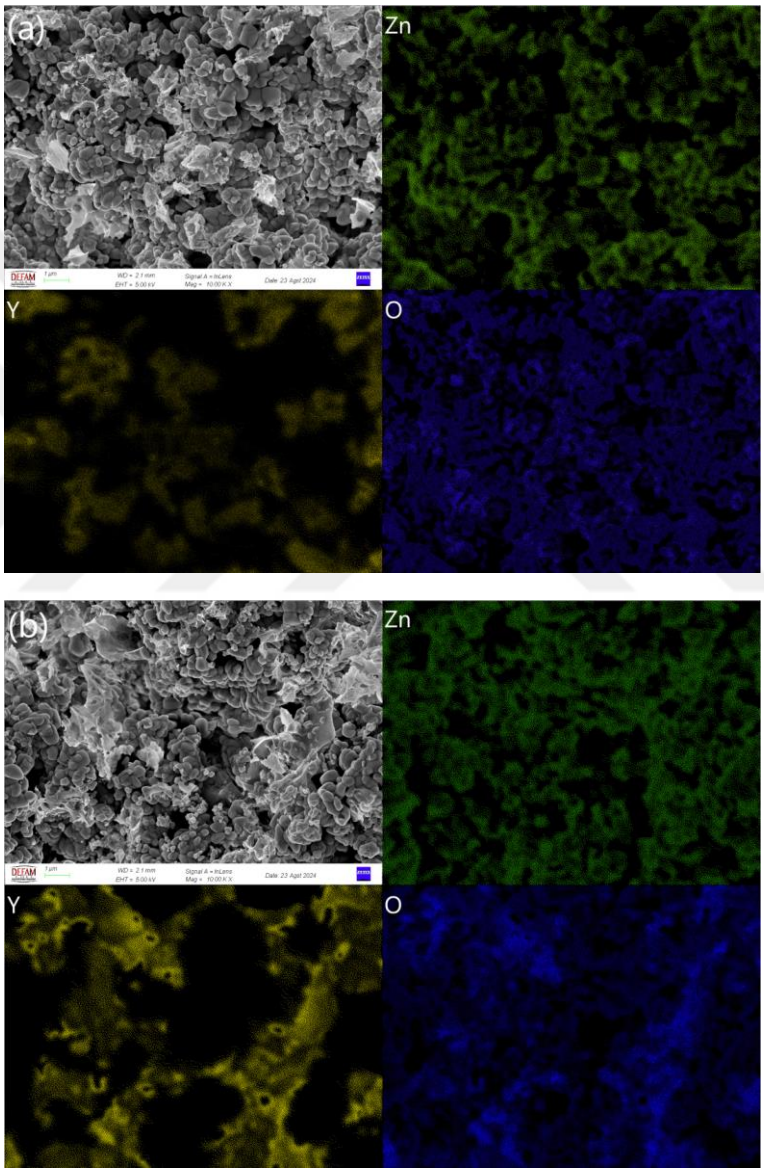


Figure 4.20 EDX mapping micrographs of **(a)** ZnO-2.5Y_2O_3, **(b)** ZnO-5Y_2O_3,**(c)** ZnO-10Y_2O_3 and **(d)** ZnO-20Y_2O_3 composites.

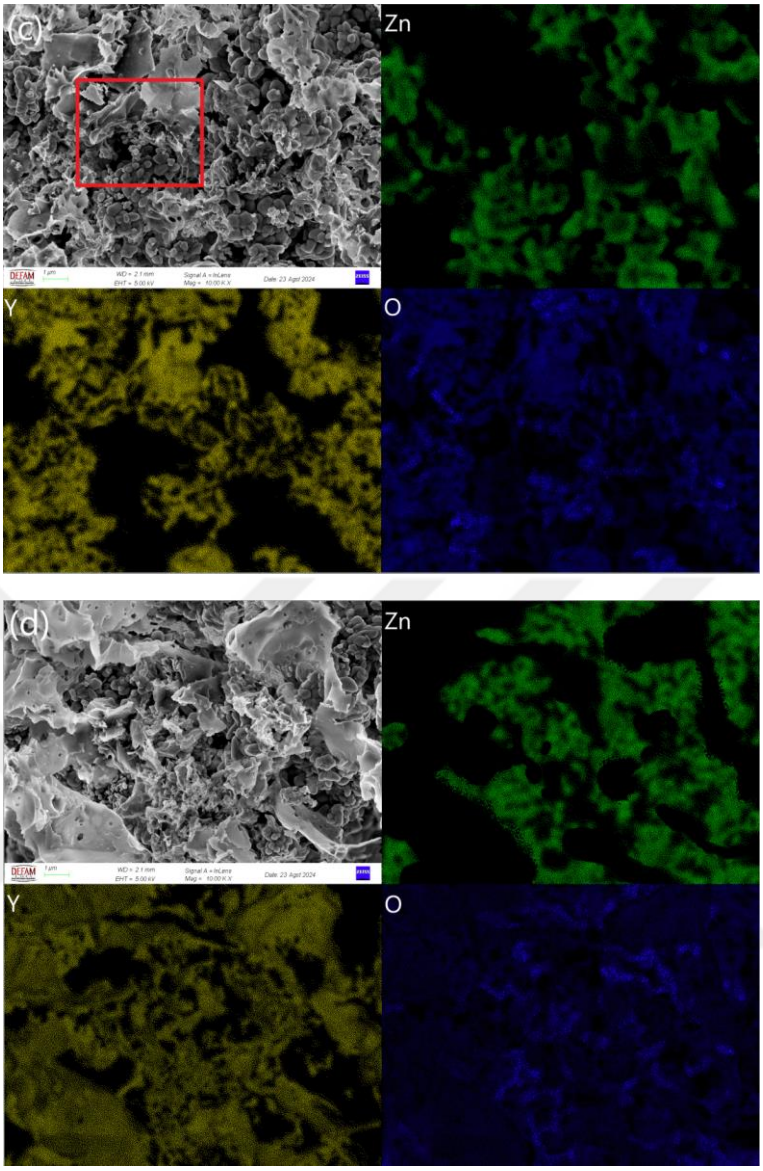


Figure 4.20 EDX mapping micrographs of **(a)** ZnO-2.5Y_2O_3, **(b)** ZnO-5Y_2O_3,**(c)** ZnO-10Y_2O_3 and **(d)** ZnO-20Y_2O_3 composites (continued)

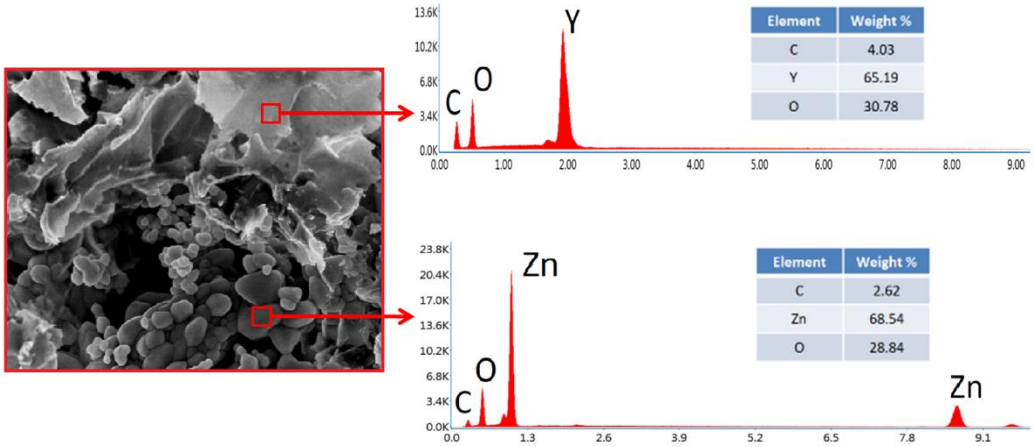


Figure 4.21 EDX elemental analysis of marked regions

The reflectance spectra of the ZnO-Y_2O_3 composite samples were analyzed across a wavelength range of 225 to 525 nm, as shown in Figure 4.22 (a). Using UV-Vis reflectance measurements, we derived the optical band gap energy (E_g) of the composites. Each sample's diffuse reflectance spectrum was converted into the Kubelka-Munk (K-M) function, allowing us to calculate the band gap energy through the appropriate equation, where (R) represents reflectance and F(R) denotes the K-M function. (Jubu et al., 2022; Landi et al., 2022).

$$F\,(R) = \frac{(1-R)^2}{2R}$$

This process enabled the construction of a Tauc plot, where $(F(R)h\nu)^2$ was plotted against photon energy ($h\nu$), as depicted in Figure 4.22 (b). The band gap energies (E_g) were determined by extending the linear portion of the plot until it intersects the x-axis. The band gap values for the composites ranged between 3.26 and 3.31 eV. In particular, ZnO-5Y_2O_3 had the smallest band gap with an energy value of about 3.26 eV, whereas ZnO-20Y_2O_3 exhibited the largest at 3.31 eV. ZnO-2.5Y_2O_3 and ZnO-10Y_2O_3 displayed band gap energies of around 3.28 eV and 3.29 eV, respectively. The observed reduction in band gap energy for ZnO-5Y_2O_3 is linked to the donor-acceptor interaction between ZnO and Y_2O_3, already further elaborated in section 4.3.2. A reduction in band gap energy is beneficial for improving photocatalytic performance by enhancing the material's light absorption capacity.

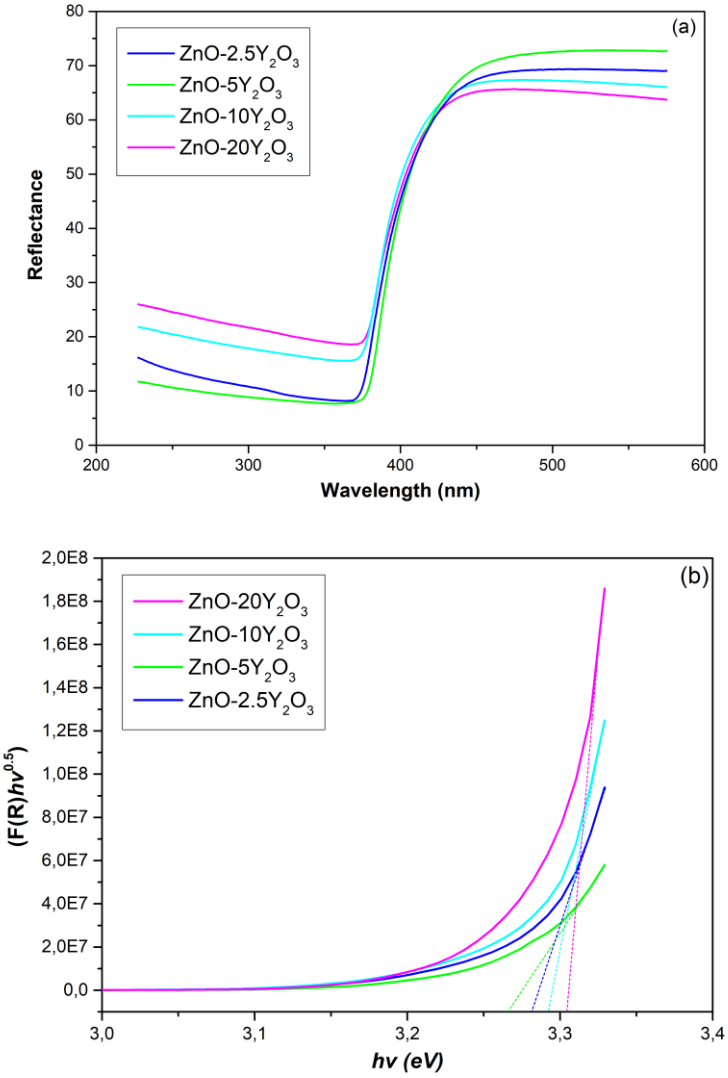


Figure 4.22 (a); Reflectance spectra of ZnO-Y_2O_3 vs. wavelength, (b); $(F(R)h\nu)^{0.5}$ plot vs. photon energy (eV)

4.5 Luminescent Characterization of ZnO-Y_2O_3 Composite Produced by Mechanical Mixing

ZnO and Y_2O_3 both exhibit luminescence independently, but when combined in a specific ratio, they demonstrate increased luminescent properties. This enhancement suggests a potential energy transfer between these two materials. To investigate this interaction further, we analyzed the emission and excitation spectra of ZnO and Y_2O_3 separately.

The absorption spectrum of ZnO and the emission spectrum of Y_2O_3 closely overlap. Y_2O_3 shows strong absorption in the 200 to 300 nm range and emits light

within the 300 to 500 nm spectrum. ZnO displays significant absorption in the 300 to 450 nm range (Figure 4.23). This overlap supports the possibility of energy transfer between particles of Y_2O_3 and ZnO. This phenomenon can be explained by Förster resonance energy transfer (FRET), which involves non-radiative dipole-dipole interactions between two closely situated fluorophores (Demchenko, 2015). In this context, Y_2O_3 acts as the donor, emitting energy, while ZnO functions as the acceptor, capturing that energy. The transfer occurs without photon emission, and the efficiency of this process is determined by the extent of spectral overlap between the emission of Y_2O_3 and the absorption of ZnO. In addition to FRET, the presence of surface states and defects in both materials may contribute to their interaction. These defects can introduce additional energy levels that modify the emission behavior (Zeng et al., 2010). The synergistic combination of Y_2O_3 and ZnO is anticipated to enhance photocatalytic activity by improving charge separation and increasing the efficiency of photogenerated carriers, which is vital for effective photocatalysis.

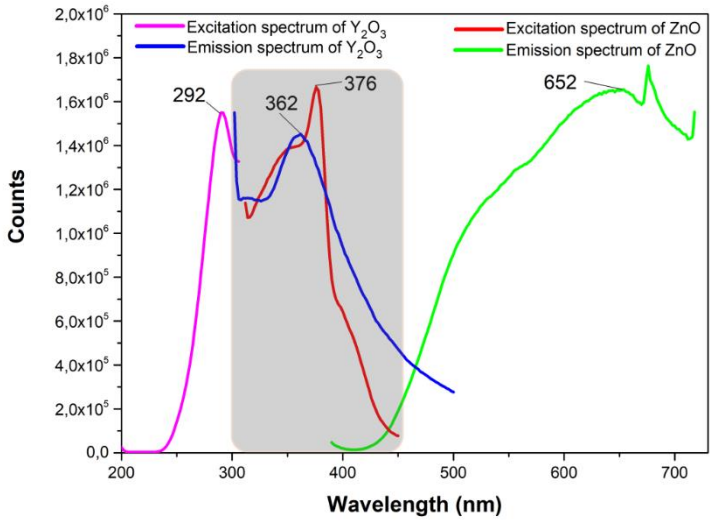


Figure 4.23 Excitation and emission spectrum of Y_2O_3 (λmax^{ex}:292 nm, λmax^{em}:362 nm) and ZnO (λmax^{ex}:376 nm, λmax^{em}:652 nm) recorded in powder form.

Techniques such as time-resolved photoluminescence are essential for confirming the occurrence of Förster resonance energy transfer (FRET) and gaining insights into the energy transfer dynamics. In this study, we investigated the excited-state lifetimes of donor-acceptor pairs, where ZnO acts as an acceptor and Y_2O_3 serves as a donor. We hypothesize that when both the donor and acceptor emit particles, energy transfer

will result in enhanced emission from the acceptor, accompanied by a shortened fluorescence lifetime and a decrease in the donor's fluorescence. Decay time measurements were taken using an excitation wavelength of 292 nm for the donor. Table 4.2 presents the decay times for various donor-acceptor pairs in different composites, with the acceptor content gradually increased while the donor concentration remained constant. As energy transitions from Y_2O_3 to ZnO, we observe a reduction in the excited state lifetime of the Y_2O_3 emission. This effect occurs due to non-radiative energy transfer to the ZnO nanoparticles, which decreases the time Y_2O_3 remains in its excited state.

Table 4.2 Decay times of the composites prepared by the donor; Y_2O_3 and their blends including increasing amounts of the acceptor counterpart; ZnO.

Donor	**Acceptor**	**λ_{max}^{ex} (nm)**	**λ_{max}^{em} (nm)**	**τ_O**	**Decay Time (μs)**	**Std. Dev. (μs)**	**Rel. (%)**
Y_2O_3 (2.5 mg)	ZnO (25 mg)	292	362	τ_1	0.57	0.0047	55.54
				τ_2	5.37	0.1220	30.05
				$\tau 3$	29.30	1.5946	14.40
				τ_{avr}	**6.15**		
Y_2O_3 (2.5 mg)	ZnO (50 mg)	292	362	τ_1	0.59	0.0046	55.66
				τ_2	5.41	0.1174	30.52
				$\tau 3$	28.19	1.4652	13.83
				τ_{avr}	**5.87**		
Y_2O_3 (2.5 mg)	ZnO (100 mg)	292	362	τ_1	0.55	0.0061	57.58
				τ_2	5.04	0.1402	30.30
				$\tau 3$	27.93	1.9396	12.12
				τ_{avr}	**5.23**		

The decay profiles of the composite blends followed a tri-exponential pattern on the microsecond scale, with distinct components for short, intermediate, and long lifetimes. As seen in Table 4.2, the trend of decreasing average excited-state lifetimes with increasing acceptor concentrations supports the occurrence of FRET. With higher ZnO concentrations, the proximity between Y_2O_3 and ZnO enhances FRET efficiency, facilitating more effective energy transfer from Y_2O_3 to ZnO. Consequently, increased ZnO concentrations correlate with shorter excited state lifetimes for Y_2O_3. In addition to FRET, variations in decay times may also arise from direct interactions between Y_2O_3 and ZnO, including changes in surface states, charge transfer mechanisms or defect-related effects. Optimizing FRET-related processes and carrier dynamics can

significantly influence the total photocatalytic performance of the composite. Effective charge separation are critical for photocatalytic systems, and the observed changes in decay times indicate an interaction and energy transfer between Y_2O_3 and ZnO.

4.6 Structural Characterization of Combine ZnO-Y_2O_3 Produced by Precipitation

According to the photocatalytic analysis, the best photocatalytic results were obtained from the composite sample containing 5% Y_2O_3 by weight. Therefore, the combined ZnO-Y_2O_3 material synthesized by the precipitation method was prepared to contain only 5% Y_2O_3 by weight, and all analyses were carried out exclusively on this material.

Figure 4.24 illustrates FTIR spectra of heat-treated and dried combine ZnO-5Y_2O_3 gel. The organic content of Zn precursor and solution after drying at 120 °C is easily seen. This is because of the precipitation of Zn precursor components. In order to obtain the desired ZnO phase, the precipitation also needs to be heated at the proper temperature. As seen in FTIR spectra organic components disappear after heat treatment. The band around 1650 cm^{-1} is attributed to the bending vibration of H-O-H (water) (Lopez et al., 1992; Sammon et al., 1998). Even after the drying process, the powder materials can absorb water molecules from the ambient air. Occasionally, Bands around 1350–1500 cm^{-1} attributed carbonate groups (CO_3^{2-}) might form if CO_2 from the air reacts with the hydroxides or other components. The presence of such bands indicates that carbonate species may be present in the precipitated material. Peak 2800–3000 cm^{-1} corresponds to C-H stretching (Amoriello et al., 2011; Lopez et al., 1992). Following heat treatment, most of the peaks belonging to organic content cannot be seen.

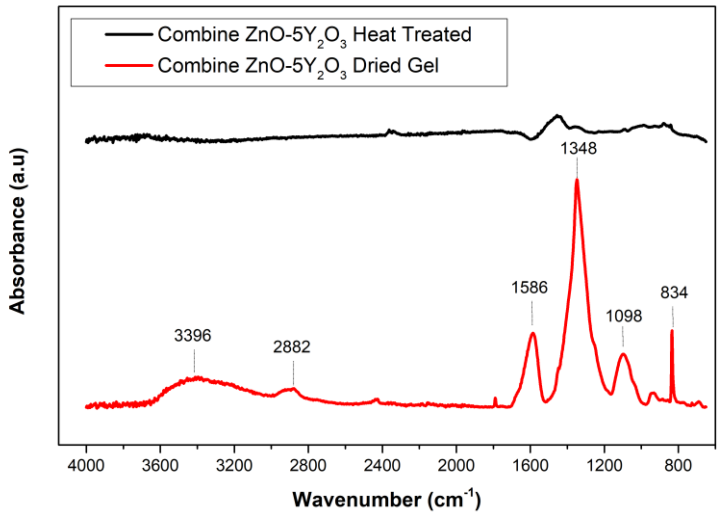


Figure 4.24 FTIR spectra of dried and heat treated combine ZnO-5Y_2O_3

Figure 4.25 shows the XRD pattern of a combined ZnO-5Y_2O_3 gel that was dried at 120 °C and subsequently heat treated at 500 °C. Despite the relatively low drying temperature of 120 °C, characteristic peaks of the ZnO structure are evident in the combined structure XRD pattern. This phenomenon is attributed to the 18-24 hour aging process. Additionally, ZnO particles that are subject to partial phase transformation may have formed in the precipitate due to the decrease in pH caused by the addition of alkali to the solution. We think that the prolonged aging process initiated the phase transformation of ZnO. Peaks corresponding to Y_2O_3 are also present, but due to the low concentration of Y_2O_3, distinguishing all its characteristic peaks is challenging. Before drying, the Y_2O_3 peaks are not clearly visible due to the high organic content in the structure. However, the peak at 29° confirms the presence of Y_2O_3. After heat treatment, the ZnO phase becomes more prominent.

Figure 4.26 shows SEM micrographs of combine ZnO-5Y_2O_3. Combined ZnO-Y_2O_3 structures have been obtained by the method of depositing Y_2O_3 material on top of ZnO. As seen in the SEM images, the deposition process was not homogeneous. Instead, more sharpened and elongated structures emerged. Since the combined ZnO-5Y_2O_3 obtained by this method showed worse performance in photocatalytic analysis than the composite ZnO-Y_2O_3, studies to improve the synthesis of the combined structure were not continued and instead focused on composite structures. Photocatalytic result of combine ZnO-5Y_2O_3 structure was given following section.

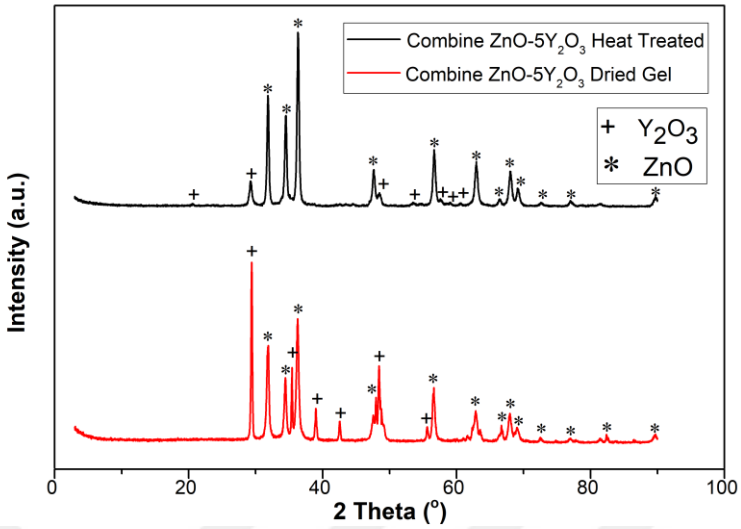


Figure 4.25 XRD pattern of combine ZnO-$5Y_2O_3$ dried and heat treated gel

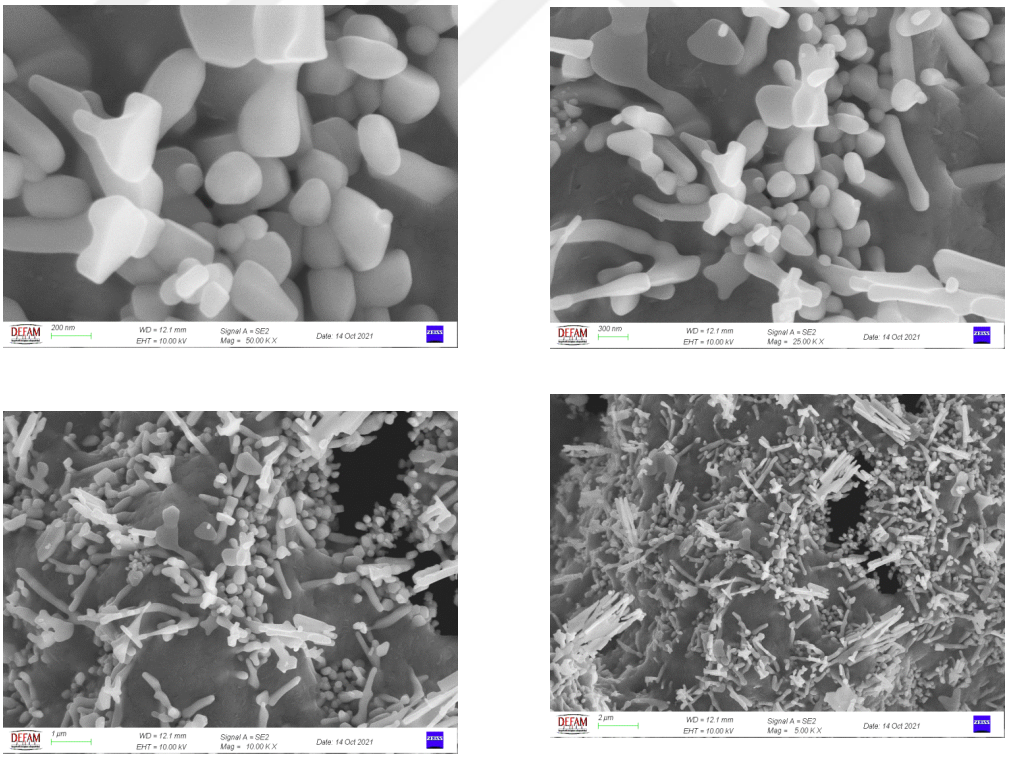


Figure 4.26 SEM micrographs of combine ZnO-Y_2O_3.

4.7 Structural and Luminescent Characterization of YAG powders

Figure 4.27 presents the DTA-TG curves for the dried YAG xerogel. The sample shows a minor endothermic peak at temperatures below 200 °C, corresponding to the removal of absorbed water and solvents. Initial weight loss of about 7.5 % is attributed to this absorption (Gowda, 1986; Sun et al., 2004). Broad and intense exothermic peaks between approximately 250 and 600 °C indicate the decomposition and pyrolysis of organic compounds, along with the removal of hydroxyl groups from the gel structure (Manalert & Rahaman, 1996; Ruan et al., 1998; Veith et al., 1999). These endothermic and exothermic events contribute to a 60% weight loss up to 600 °C. Additionally, a weak exothermic peak at 900 °C marks the onset of powder crystallization (Lu, Dong, Wang & Wang, 2002; Manalert & Rahaman, 1996; Ruan et al., 1998; Veith et al., 1999).

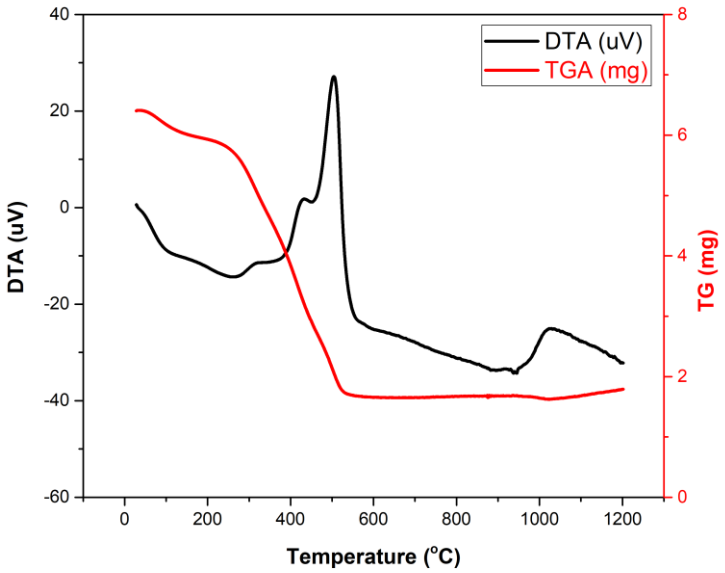


Figure 4.27 DTA-TG analysis of dried YAG xerogel powders

Figure 4.28 shows FTIR spectra of dried 2 MRCM YAG. The presence of broad absorption bands around 3400–3600 cm^{-1} is indicative of hydroxyl (OH) stretching vibrations (Hassanzadeh-Tabrizi, Taheri-Nassaj & Sarpoolaky, 2008; Qiu et al., 2005). These peaks are often attributed to the residual hydroxyl groups or water molecules that are still present in the xerogel after the drying process. Because organic precursors and solvents such as alcohol and citric acid were used during the sol-gel process, their

residual peaks are observed in the FTIR spectrum. These appear as peaks in the regions corresponding to C-H stretching (2800–3000 cm^{-1}) and C-O stretching (1000–1700 cm^{-1}) (Boyer, Bertrand-Chadeyron & Mahiou, 2004; Hassanzadeh-Tabrizi et al., 2008; Qiu et al., 2005).

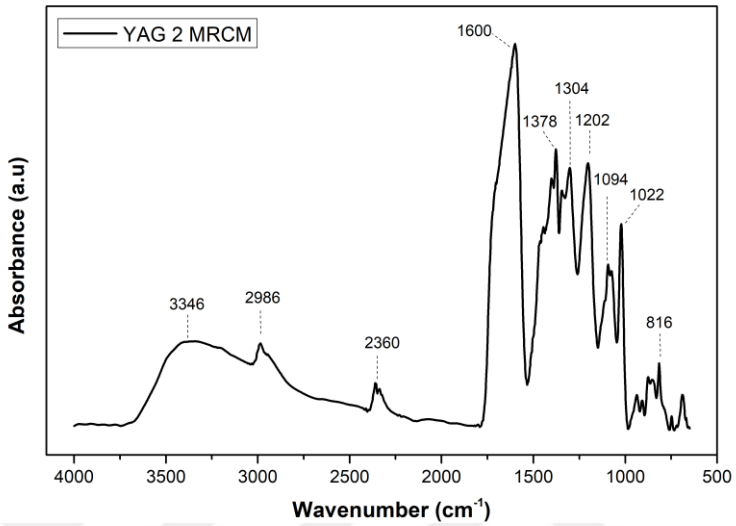


Figure 4.28 FTIR spectra of dried YAG 2 MRCM gel

XRD results of doped and pure YAG particles are exhibited in Figure 4.29. Results revealed highly crystalline structures were obtained for all samples. Pure, Eu and Ce doped YAG particles were synthesized successfully. YAG phase was in good agreement with JCPDS Card (00-033-0040) (Hassanzadeh-Tabrizi, 2011; Kosyanov et al., 2021; Zhang & Yu, 2009). The diffraction peaks appear at 2θ values of 18.14º, 20.96º, 27.86º, 29.78º, 33.4º, 36.68º, 38.26º, 41.22º, 42. º, 46.68º, 52.86º, 55.22º, 57.42º, 60.66º, 61.8º, 70.16º and 72.06º corresponding to crystal planes (211), (220), (321), (400), (420), (422), (431), (521), (440), (532), (444), (644), (642), (651), (800), (840) and(842). Based on the diffraction spectrum of the prepared YAG particles, it is worthwhile to note that there was no remarkable change in terms of the intensity of produced doped and pure YAG particles. There is also no other phase because of doping elements which are Eu and Ce. These results showed that dopant elements are totally embedded into the YAG host lattice.

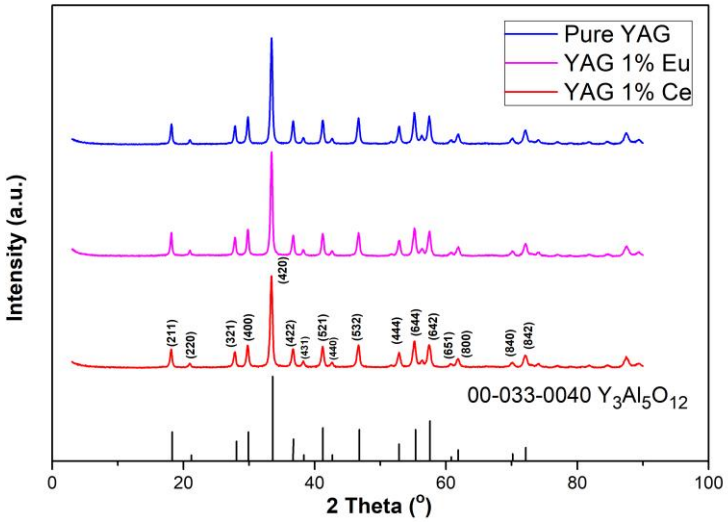


Figure 4.29 XRD patterns of pure, 1% Eu and 1% Ce doped YAG

Figure 4.30 shows the XRD pattern of the ZnO-5YAG sample containing 5% YAG by weight. Due to the significantly higher proportion of ZnO compared to YAG in the composite structure, there is a noticeable reduction in the intensity of the YAG peaks. Nonetheless, the characteristic peaks of both phases are clearly distinguishable. This indicates that the materials within the composite structure are homogeneously mixed, without formation of any intermediate phases.

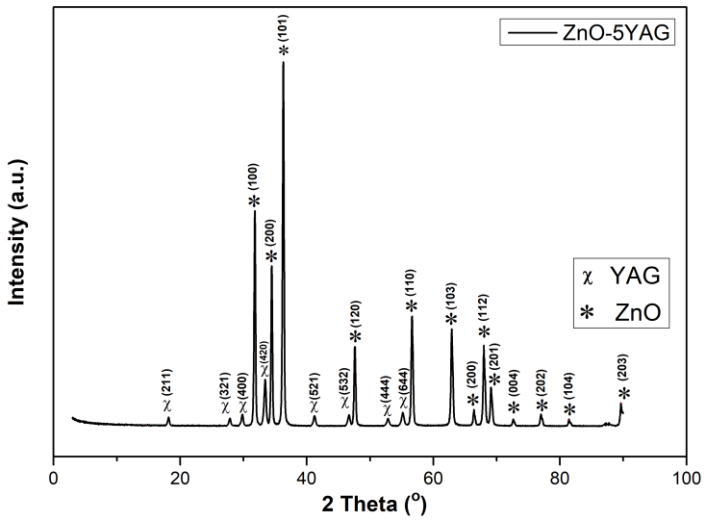


Figure 4.30 XRD pattern of composite ZnO-5YAG

Luminescence analyses were initially conducted on pure YAG. The aim of these studies was to determine whether pure YAG emits radiation capable of exciting ZnO.

As seen in Figure 4.31, the pure YAG sample did not exhibit any excitation in the 200-300 nm range. It is clear that, as a result, it did not produce any emission either. Consequently, the findings indicate that pure YAG is not a suitable material for exciting ZnO.

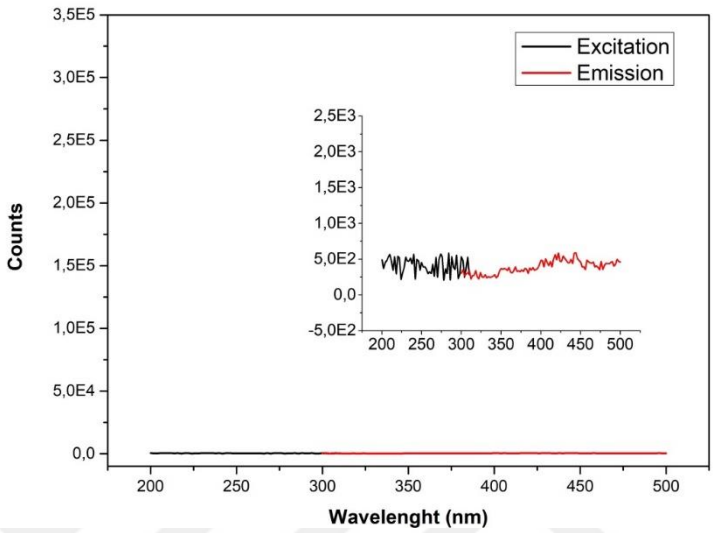


Figure 4.31 Excitation and emission spectra of pure YAG between 200 and 500 nm

The YAG sample was doped with 1% Eu to enhance its luminescent characteristics, leading to a series of experiments. In Figure 4.32 (a), the excitation and emission spectra for this material are displayed, revealing a maximum excitation wavelength of 366 nm and an emission peak at 554 nm. The main absorption peaks for the YAG;Eu sample were identified at 254 nm and 366 nm, with a notable emission peak at 554 nm. The spectra consist of a strong band centered at 254 nm, attributed to charge transfer related $^4F_7$ ground state to $^4F_{6,}$ $^5D_1$ exited state. Additionally, the expected transitions for Eu^{3+} are observed at 366 nm, corresponding to the $^7F_0 \rightarrow ^5D_4$ transition (Santos et al., 2019). The luminescent spectra display the distinctive emission of Eu^{2+}, primarily featuring transitions associated with $^4F_6{}^5D_1 \rightarrow ^4F_7$ at 498 and emission of Eu^{3+} centered 554 nm, $^5D_0 \rightarrow ^7F_1$ at 592 nm, $^5D_0 \rightarrow ^7F_2$ at 610, and $^5D_0 \rightarrow ^7F_3$ at 654 nm (Fadlalla, Tang, Elssfah & Shi, 2008; Hassanzadeh-Tabrizi, 2011; Santos et al., 2019; Zhu et al., 2013). Unfortunately, as previously mentioned, the emitted light at these wavelengths is not effective for exciting ZnO material.

To determine if the YAG;Eu material could emit at suitable wavelengths, the excitation wavelength was modified to explore higher energy levels. However, no positive results were observed for excitations below 300 nm. Consequently, it was concluded that the YAG;Eu material also fails to generate the necessary emissions to excite ZnO. Figure 4.32 (b) provides the excitation and emission spectra of the Eu doped YAG within the 200 to 450 nm range.

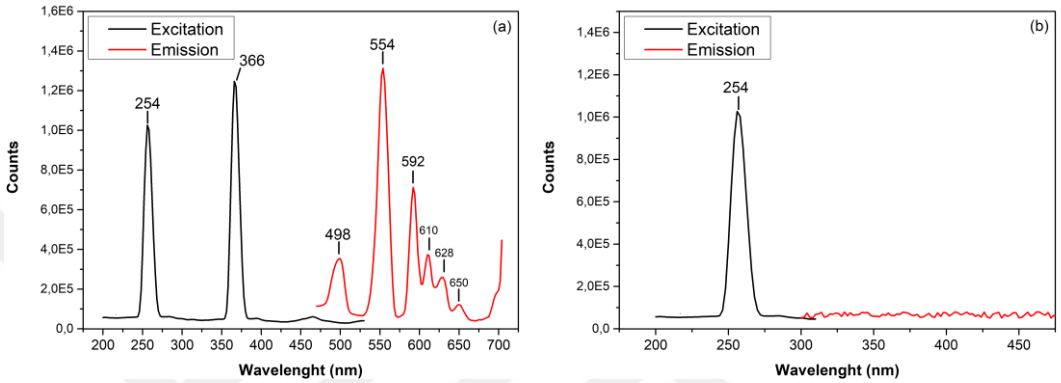


Figure 4.32 (a): Excitation and emission spectra Eu doped YAG (λ_{max}^{ex}:366 nm, λ_{max}^{em}:554 nm) (b): Excitation and emission spectra of Ce doped YAG between 200 and 450 nm

The YAG sample was doped with Ce in an effort to enhance its luminescent properties. Various luminescence experiments were conducted on the Ce doped YAG sample. Figure 4.33 (a) excitation and emission spectra 1% Ce doped YAG (λ_{max}^{ex}:460 nm, λ_{max}^{em}:540 nm. It was found that the main absorption peaks of the YAG;Ce sample occurred at 340 nm and 460 nm. Correspondingly, a significant emission peak was observed at 540 nm. The emission is attributed to the transition from the 5d excited state to the 4f ground state of the Ce^{+3} ion in the YAG crystal. These peaks represent the characteristic energy levels associated with the ^{5}d and ^{4}f states (Chao, Wu & Wu, 2010; Yan et al., 2008). However, as previously mentioned, the emitted light at these wavelengths is unfortunately not suitable for exciting ZnO material. To assess whether the YAG;Ce material could emit at suitable wavelengths, the excitation wavelength was varied to include higher energy levels. Excitations below 300 nm did not produce positive results. As a result, it was concluded that the YAG;Ce material is also incapable of generating the necessary emissions to excite ZnO. Figure 4.33 (b) shows excitation and emission spectra of Ce doped YAG between 200 and 500 nm.

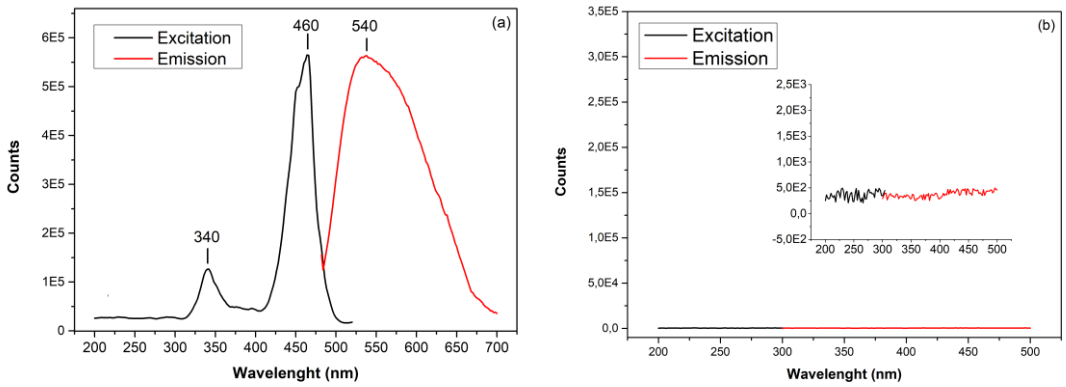


Figure 4.33 (a): Excitation and emission spectra Ce doped YAG (λ_{max}^{ex}:460 nm, λ_{max}^{em}:540 nm), (b) Excitation and emission spectra of Ce doped YAG between 200 and 500 nm.

4.8 Photocatalytic Analyzes

The photocatalytic activity of pure Y_2O_3, YAG, ZnO, and ZnO-Y_2O_3 and ZnO-YAG composite and combine structures was evaluated in a custom-designed reactor using a methylene blue (MB) solution, which was irradiated with the Osram, UltraVitalux E27, 300 W UV light. The initial concentration of MB was set at 10^{-5} M, corresponding to an absorbance of 0.754. For each trial, 25 mg of the ZnO-Y_2O_3 composites were introduced into 50 mL of the MB solution, which was stirred intensively in the dark for 10 minutes to allow adsorption-desorption equilibrium to be reached., corresponding to an absorbance of 0.754. For each experiment, 25 mg of the ZnO-Y_2O_3 composites were added to 50 ml of the MB solution, which was stirred vigorously in the dark for 10 minutes to establish adsorption-desorption equilibrium.

Throughout the experiments, the distance between the UV lamp and the beaker was kept constant at 30 cm. Once the lamp was activated, the MB solution containing the ZnO-Y_2O_3 and ZnO-YAG composites was subjected to irradiation. At predetermined intervals, the solutions were centrifuged at 5000 rpm for 10 minutes to separate the catalysts, and 3 ml of the supernatant was collected for absorbance analysis using a spectrophotometer (Shimadzu, UV-1240), specifically monitoring the peak at 663 nm. This process enabled a thorough assessment of the photocatalytic reaction's progress. After collecting the absorbance data, the values were converted to concentration using the Beer-Lambert law, which describes the linear relationship between absorbance and

concentration in dilute MB solutions (Fernández-Pérez & Marbán, 2022; Li Puma & Brucato, 2007).

The photocatalytic degradation efficiency was quantified using the formula $[(C_0 - C)/C_0] \times 100$, where C_0 is the initial concentration of MB and C is the concentration measured after the reaction terminated. This method offers a clear indication of the effectiveness of catalyst in decomposing MB, which is crucial for assessing its potential for practical applications.

4.8.1 Photocatalytic Analyzes of Pure Y_2O_3, YAG and ZnO

For a reliable comparison, the absorbance of the pure MB solution, absent of any metal oxide particles, was recorded under UV irradiation prior to the experiment. Figure 4.34 illustrates the absorbance spectrum of this solution over time.

Initially, the absorbance value of the MB solution without any metal oxide was 0.754. After 30 and 60 minutes total of UV light irradiation, this value decreased to 0.733 and 0.71, respectively. These indicate a 0.5% of decrease. The same measurements were conducted for MB solutions containing only Y_2O_3, YAG, or ZnO. No significant changes were observed when Y_2O_3 and YAG were tested alone, and the reduction remained around 0.5%. Figures 4.35 and 4.36 present the absorbance spectra for MB solutions with pure Y_2O_3 and YAG, respectively.

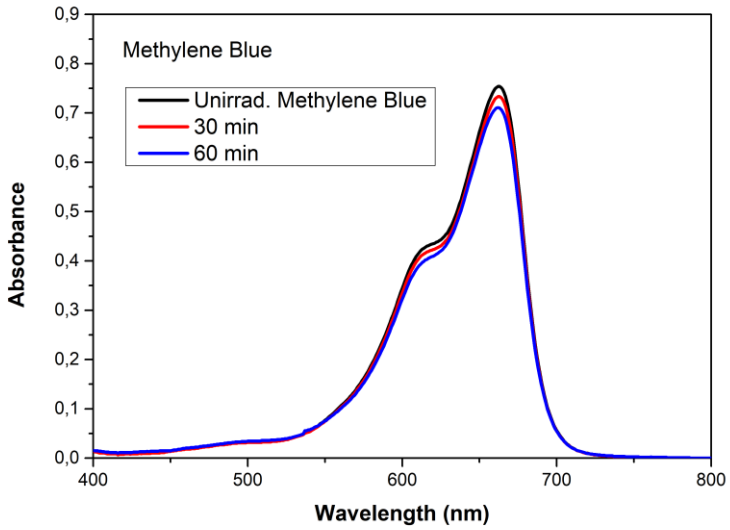


Figure 4.34 Absorbance spectrum of MB solution versus irradiation time

These results indicate that without a catalyst, MB is not substantially degraded. Furthermore, using Y_2O_3 or YAG individually in the MB solution did not result in any notable photocatalytic activity. Consequently, it can be concluded that both Y_2O_3 and YAG do not contribute to the photocatalytic decomposition reaction when used independently, and any slight changes in absorbance are likely attributable to external environmental factors rather than their direct influence.

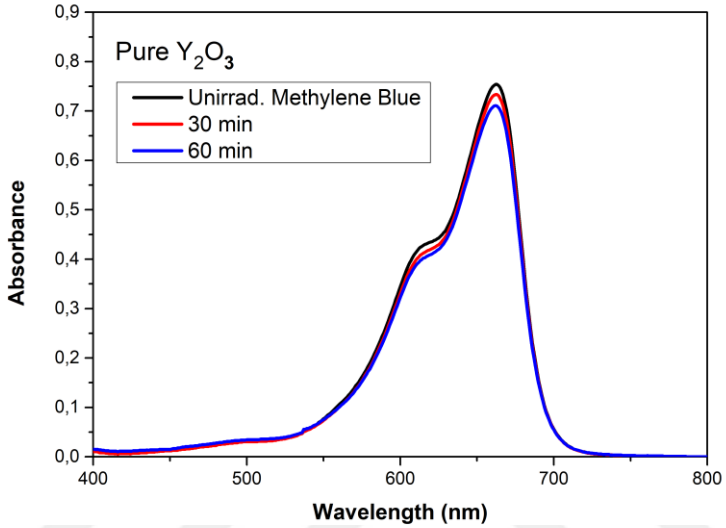


Figure 4.35 Absorbance spectrum of MB solution versus irradiation time for pure Y_2O_3

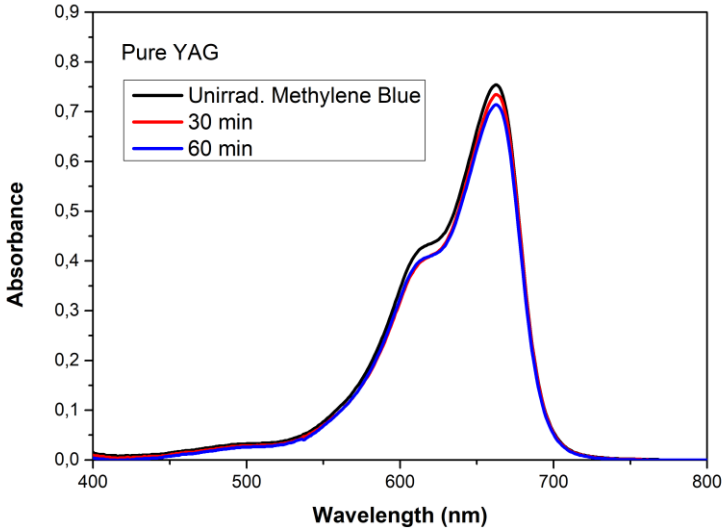


Figure 4.36 Absorbance spectrum of MB solution versus irradiation time for pure YAG

Figure 4.37 presents the absorbance spectrum of the MB solution over time of irradiation for pure ZnO. Unlike Y_2O_3 and YAG, the addition of ZnO to the MB

solution triggered the expected photocatalytic process, resulting in a gradual reduction in absorbance values, which were measured at 30-minute intervals. The initial absorbance of 0.754 decreased to 0.542 after 30 minutes and to 0.395 after 60 minutes. Photocatalytic tests for ZnO continued for up to 150 minutes to facilitate further comparisons.

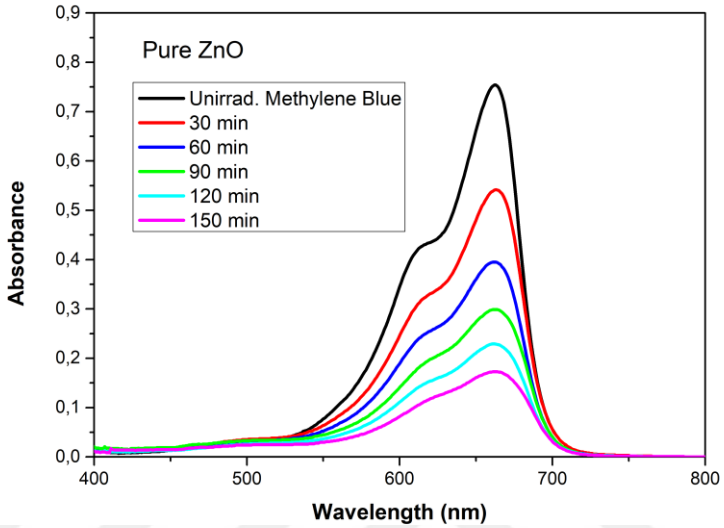


Figure 4.37 Absorbance spectrum of MB solution versus irradiation time for pure ZnO

4.8.2 Photocatalytic Analyzes of Composite ZnO-Y_2O_3, ZnO-Y_2O_3;Eu, ZnO-Y_2O_3;Ce

The photocatalytic performance of ZnO-Y_2O_3 composite structures containing varying amounts of Y_2O_3 can be observed for irradiations lasting 30 and 150 minutes in Figures 4.38 (a) and (b), respectively. As mentioned earlier, Y_2O_3 independently does not demonstrate any photocatalytic effectiveness. The primary objective of the experimental photocatalytic studies was to assess whether the addition of Y_2O_3, when combined with ZnO, influences its catalytic performance. The results of the analysis indicated that incorporating a specific amount of Y_2O_3 with ZnO notably enhances its catalytic efficiency. To identify the optimal amount, composite samples prepared previously were each exposed to irradiation under the same conditions., followed by measurements. According to the measurement results, it was found that the sample containing 5% Y_2O_3 (ZnO-5Y_2O_3) compared to pure ZnO exhibited the highest catalytic performance.

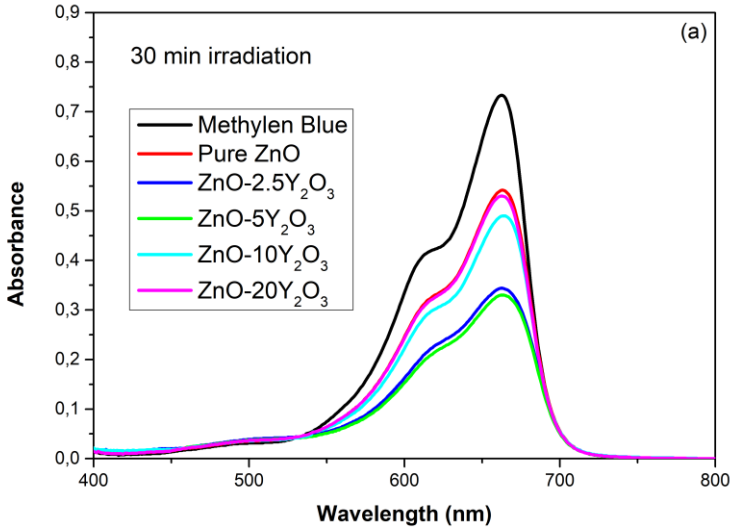


Figure 4.38 Absorbance spectrum of MB solution versus irradiation time for pure ZnO and composite ZnO-Y_2O_3 samples after (a) 30 min. and (b) 150 min. irradiation

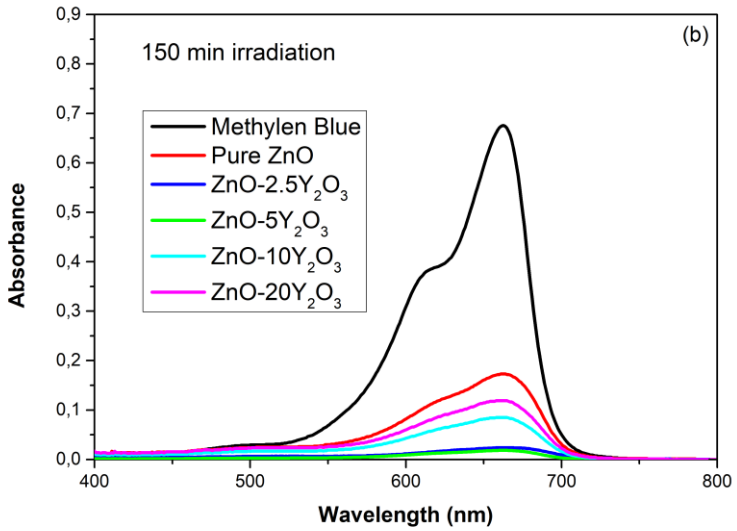


Figure 4.38 Absorbance spectrum of MB solution versus irradiation time for pure ZnO and composite ZnO-Y_2O_3 samples after (a) 30 min. and (b) 150 min. irradiation

After a duration of 150 minutes, the results showed no notable alterations, with the composite structure incorporating 5% Y_2O_3 demonstrating the most effective performance. Following an initial 30 minutes of excitation, the absorbance of the MB solution with pure ZnO diminished from 0.733 to 0.542. In contrast, the introduction of 5% Y_2O_3 by weight to create the ZnO-5Y_2O_3 composite resulted in a further reduction of absorbance to 0.33, reflecting an improvement exceeding 100% in performance. When the UV-Vis light excitation was prolonged for an additional 2 hours, the impact of Y_2O_3 became increasingly evident, revealing a substantial

difference. At the conclusion of the 150-minute irradiation period, the absorbance of the MB solution with pure ZnO fell to 0.173, while the ZnO-5Y_2O_3 composite exhibited a significantly lower absorbance of 0.018.

An increase of up to 5% in Y_2O_3 content improved the catalytic performance of ZnO; however, higher concentrations beyond 5% began to negatively affect ZnO's efficiency. The supporting role of Y_2O_3 in this process is further explained through luminescence analyses. It has been previously established that Y_2O_3 alone does not contribute to catalytic reaction. We propose that when the Y_2O_3 content exceeds 5%, it may obstruct the interaction between ZnO, the primary catalyst, and the light required for photocatalysis, thus reducing the overall efficiency.

For ZnO to function as a photocatalyst, it must absorb energy that is equal to or greater than its band gap energy, which excites electrons from the valence band to the conduction band. This excitation leads to the separation of charge, creating positively charged holes in the valence band (Carp et al., 2004; Mills & Le Hunte, 1997). In addition to the photocatalytic mechanism described in Section 2.1, the emission from Y_2O_3 within the composite structure also contributes to the photocatalytic process. In our investigation, the luminescent Y_2O_3 incorporated into the composite serves as a secondary stimulus center alongside the external light source. Thanks to its luminescent characteristics, Y_2O_3 emits radiation that is capable of exciting ZnO. This emission enhances the efficiency of the initial phase of the photocatalytic reactions, as stated in Equation 2.1. Schematic illustration of ZnO-Y_2O_3 photocatalytic system is illustrated in Figure 4.39. The process promotes the efficient transfer of electrons from ZnO's valence band to its conduction band. We further substantiate this hypothesis through decay time analysis. As demonstrated in Figure 4.23, the emission spectrum of Y_2O_3 closely aligns with the excitation spectrum of ZnO.

$$ZnO + h\vartheta \rightarrow e^- + h^+ \qquad \text{Eq. (2.1)}$$

$$ZnO + h\vartheta + emission\ of\ Y_2O_3 \rightarrow e^- + h^+ \qquad \text{Eq. (2.1.1)}$$

$$h^+ + H_2O \rightarrow H^+ + OH\cdot \qquad \text{Eq. (2.2)}$$

$$O_2^- + e^- \rightarrow O_2\cdot^- \qquad \text{Eq. (2.3)}$$

$$H_2O \rightarrow H^+ + OH^- \quad \text{Eq. (2.4)}$$

$$O_2 \cdot^- + H^+ \rightarrow HOO \cdot \quad \text{Eq. (2.5)}$$

$$HOO \cdot + e^- \rightarrow HOO^- \quad \text{Eq. (2.6)}$$

$$HOO^- + H^+ + e^- \rightarrow H_2O_2 \quad \text{Eq. (2.7)}$$

$$OH \cdot + organic\ compound \rightarrow CO_2 + H_2O \quad \text{Eq. (2.8)}$$

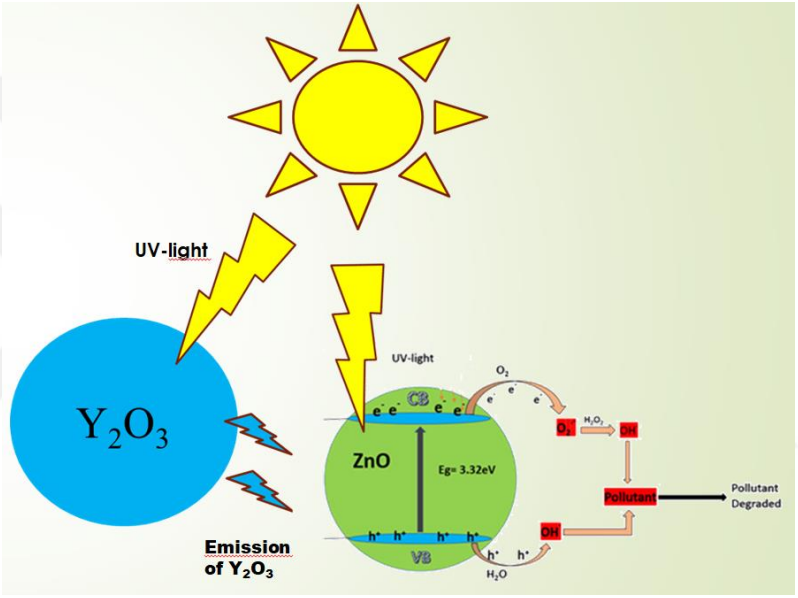


Figure 4.39 Illustration ZnO-Y_2O_3 photocatalytic system

To observe the effect of Eu doping to Y_2O_3 host lattice on photocatalytic results, ZnO-Y_2O_3 composite samples containing various amounts of Eu dopant were prepared and analyzed. According to the results, the addition of the dopant did not have a positive impact on photocatalytic performance; in fact, as the dopant concentration increased, losses in photocatalytic efficiency also increased. As shown in Figure 4.40 (a) and (b), the best results were obtained with the ZnO-Y_2O_3 structure containing pure Y_2O_3 It is suggested that the emission around 320 nm from pure Y_2O_3 is negatively affected as the dopant concentration increases. We observed that the decreased emission at this wavelength led to a reduction in ZnO excitation. Consequently, we

think that this decrease in excitation contributed to a reduction in the efficiency of the photocatalytic reaction.

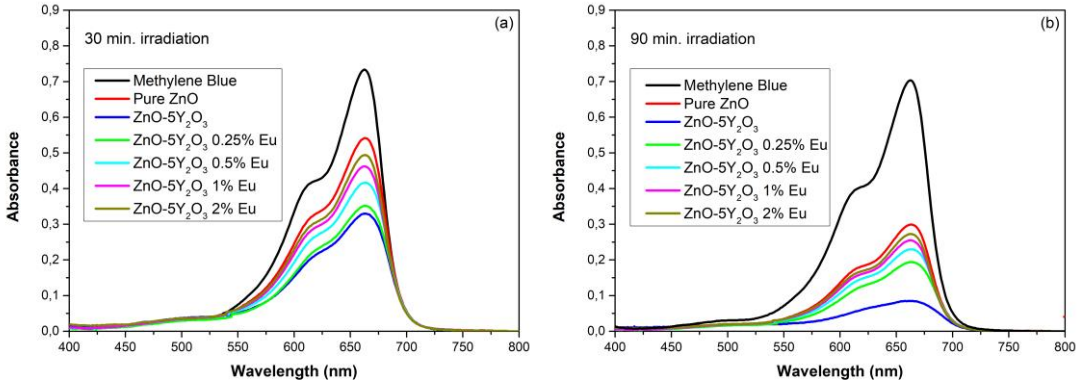


Figure 4.40 Absorbance spectrum of MB solution versus irradiation time for pure ZnO , composite ZnO-$5Y_2O_3$, and ZnO-$5Y_2O_3$ with different amount of Eu such 0.25%, 0.5%, 1% and 2% samples after (a) 30 and (b) 90 min. irradiation

To test the photocatalytic performance of Ce doped Y_2O_3, only 1% Ce doped Y_2O_3 was synthesized, unlike the different amounts of Eu doped samples, to minimize the waste of consumable materials during synthesis. Figure 4.41 displays the comparative photocatalytic analysis results of the Eu and Ce doped composite samples. Similar to the Eu doped samples, the Ce dopant does not have a positive effect on the photocatalytic performance of the ZnO-Y_2O_3 composite structure. It is suggested that the negative impact of the dopant on the emission around 320 nm from pure Y_2O_3 contributes to the deterioration of photocatalytic performance. These results indicate that neither the Eu nor the Ce dopant positively influences the photocatalytic performance of the ZnO-Y_2O_3 composite material.

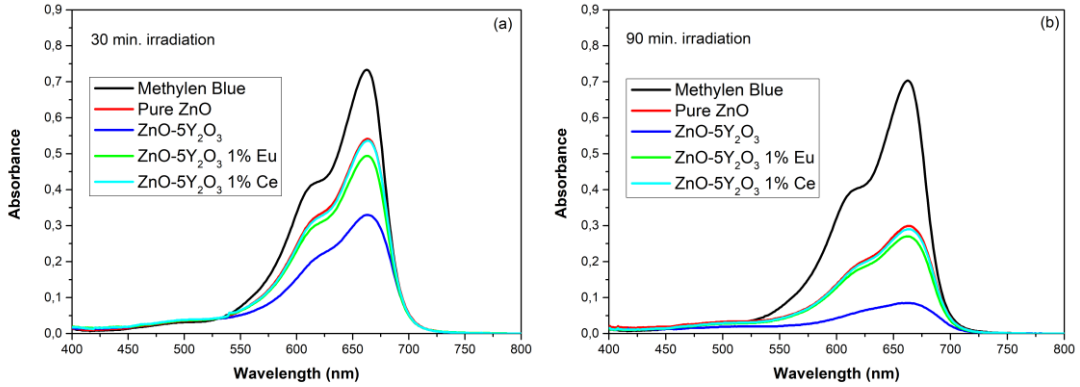


Figure 4.41 Absorbance spectrum of MB solution versus irradiation time for pure ZnO and composite ZnO-$5Y_2O_3$, ZnO-$5Y_2O_3$ % 1 Eu, ZnO-$5Y_2O_3$ % 1 Ce samples after (a) 30 and (b) 90 min. irradiation

4.8.3 Photocatalytic Analyzes of Combine ZnO-Y_2O_3

Based on the analysis results, the highest photocatalytic efficiency was achieved with the ZnO-Y_2O_3 composite containing 5% Y_2O_3. Therefore, both the Eu and Ce doped samples, as well as the combined ZnO-Y_2O_3 samples prepared using an alternative production method, were prepared to contain 5% Y_2O_3 and subsequently analyzed.

Figure 4.42 presents the photocatalytic results of the combined and composite ZnO-Y_2O_3 samples. As evident from the graphs, the ZnO-Y_2O_3 composite samples exhibit significantly superior photocatalytic performance compared to the combined samples. The poorer results of the combined ZnO-Y_2O_3 structure compared to the composite structures are thought to be due to the non-homogeneous distribution of ZnO and Y_2O_3 within the material. Additionally, the needle-like structure observed in SEM analyses of the combine ZnO-Y_2O_3 (Section 4.6) is believed to negatively impact the energy transfer between ZnO and Y_2O_3.

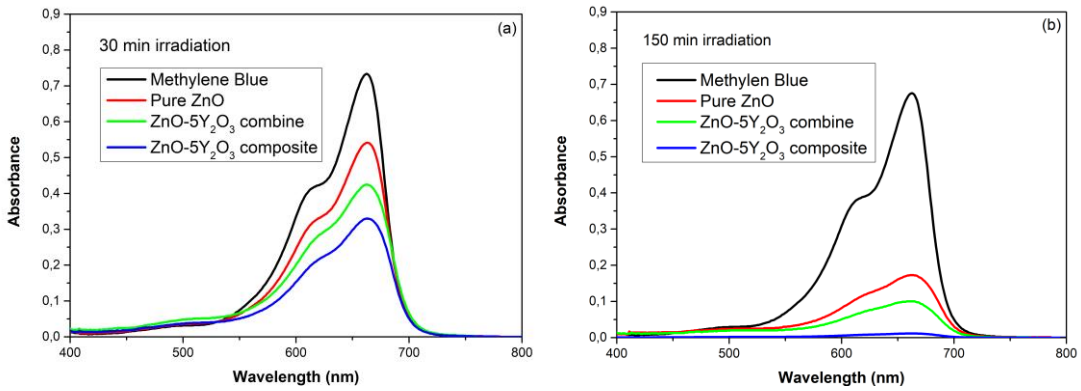


Figure 4.42 Absorbance spectrum of MB solution versus irradiation time for pure ZnO, composite ZnO-Y_2O_3 and combine ZnO-Y_2O_3 samples after (a) 30 min. and (b) 150 min. irradiation

4.8.4 Photocatalytic Analyzes of Composite ZnO-YAG, ZnO-YAG;Eu and ZnO-YAG;Ce

Figure 4.43 illustrates the photocatalytic results of ZnO-YAG composites prepared with 1% Eu doped and 1% Ce doped YAG materials. As anticipated from the luminescence results, the ZnO-YAG composite materials did not contribute to the photocatalytic mechanism in any significant way. These composite samples exhibited

worse photocatalytic performance compared to pure ZnO. This finding aligns with the luminescence results of the pure and Eu, Ce doped YAG samples. Since the YAG samples did not emit light capable of exciting ZnO, no improvement in photocatalytic results was observed. Furthermore, the presence of YAG material created a shading effect, obstructing the contact between ZnO and the exciting light, which led to a decrease in the efficiency of the photocatalytic reaction.

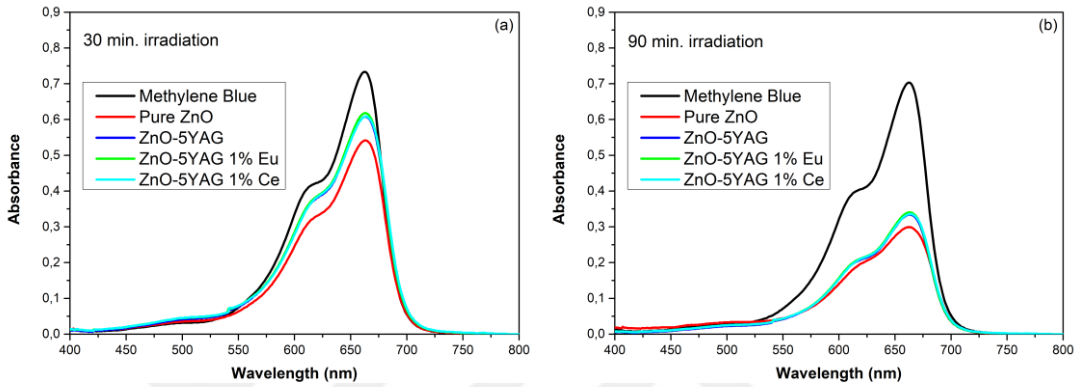


Figure 4.43 Absorbance spectrum of MB solution versus irradiation time for pure ZnO and composite ZnO-5YAG, ZnO-5YAG % 1Eu, ZnO-5YAG % 1Ce samples after (a) 30 and (b) 90 min. irradiation

4.8.5 Detailed photocatalytic studies of ZnO-Y_2O_3 composites

In Figure 4.44, the graph illustrates the changes in concentration of MB solutions containing different composites over various time intervals. To enable precise comparison, the absorbance values for the pure MB solution were measured under the same irradiation conditions. The initial concentration is represented by C_0, while C refers to the concentration after exposure to irradiation. It is clear from the graph that the ZnO-5Y_2O_3 composite shows the lowest concentration among the samples.

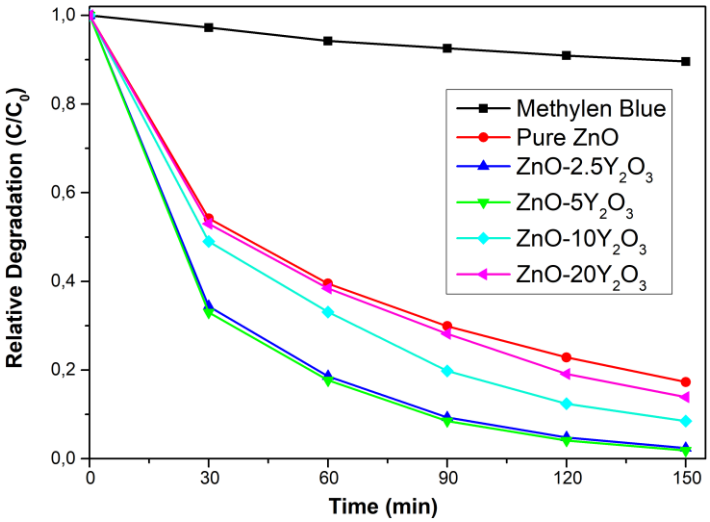


Figure 4.44 Relative concentration changes (C/C_0) of MB solutions

Figure 4.45 illustrates that the photocatalytic degradation process adheres to the pseudo-first-order kinetic model, represented by the equation:.

$$\ln\frac{C_O}{C} = (k_{app})t$$

Here, (t) refers to the time of exposure, and (k_{app}) represents the apparent rate constant for the degradation reaction. The values of (k_{app}) can be determined from the slope of the linear fits of the curves (Lidija V Trandafilović, Dragana J Jovanović, X Zhang, S Ptasińska & MD Dramićanin, 2017). The degradation rate constant is notably highest for ZnO-5Y_2O_3, whereas pure ZnO powder displays the lowest rate constant. This value for the samples pure ZnO, ZnO-2.5Y_2O_3, ZnO-5Y_2O_3, ZnO-10Y_2O_3 and ZnO-20Y_2O_3 are $0.9\text{x}10^{-2}$ $2.27\text{x}10^{-2}$, $2.42\text{x}10^{-2}$, $1.48\text{x}10^{-2}$ and $1.12\text{x}10^{-2}$.

Figure 4.46 illustrates the photocatalytic degradation efficiencies of both pure ZnO and ZnO-Y_2O_3 composite photocatalysts. Upon examining the results, it became evident that the ZnO-5Y_2O_3 composite achieved the highest efficiency, as expected. It was concluded that composites with less than 5% Y_2O_3 by weight were not effective in sufficiently exciting ZnO. Additionally, when the Y_2O_3 content exceeded 5%, such as in the 10% and 20% composites, the effectiveness of UV light in exciting ZnO was reduced. The higher concentrations of Y_2O_3 cause a shading effect, which hinders the penetration of UV light to the ZnO. Therefore, the ZnO-5Y_2O_3 composition, where the

energy transfer between ZnO and Y_2O_3 is optimized, demonstrated the most efficient photocatalytic performance.

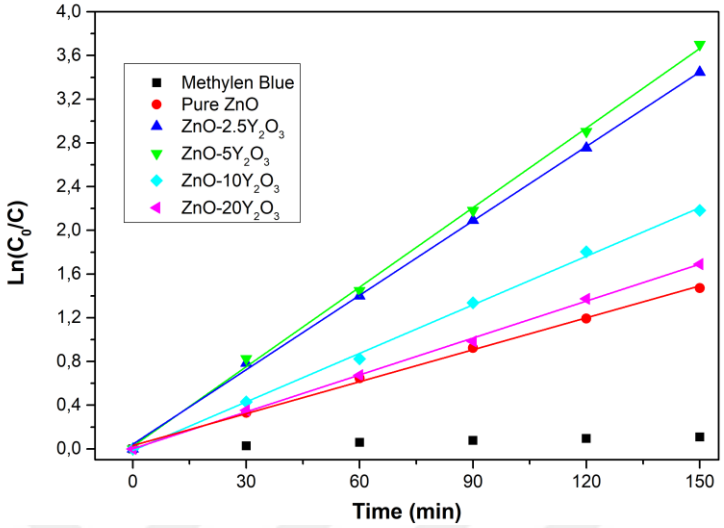


Figure 4.45 Photocatalytic degradation kinetic constant of ZnO photocatalysts

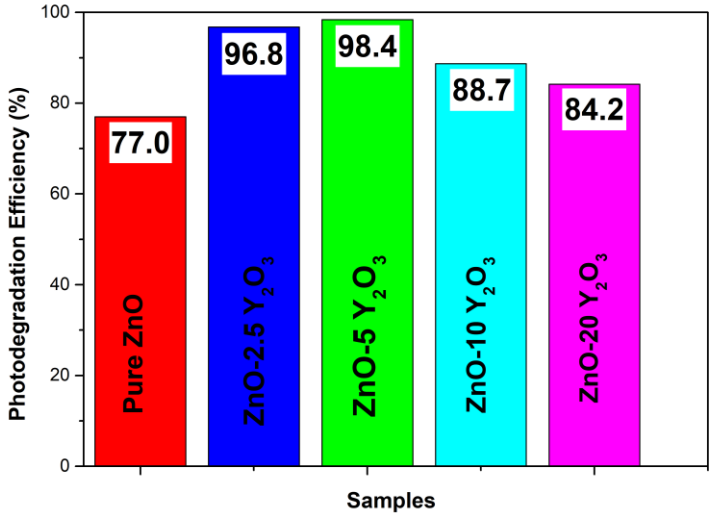


Figure 4.46 Photocatalytic degradation efficiency of pure ZnO and ZnO-Y_2O_3 composites photocatalysts

The reusability of the ZnO-$5Y_2O_3$ composite photocatalyst was evaluated through multiple cycles using an MB dye solution, as shown in Figure 4.47. After five cycles of reuse, no significant changes in degradation efficiency were detected. This clearly indicates that the synthesized ZnO-$5Y_2O_3$ photocatalyst demonstrates excellent

reusability and stability, making it suitable for potential industrial and environmental applications. Table 4.3 compares all samples in terms of photocatalytic degradation performances.

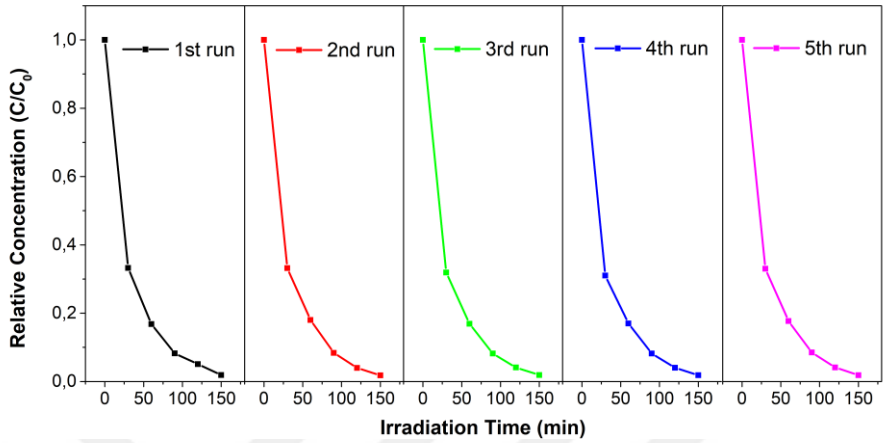


Figure 4.47 Stability and reusability study of ZnO-Y_2O_3 composite photocatalyst powders in the MB degradation process under irradiation for five runs.

Table 4.3 Photocatalytic degradation performances of pure ZnO, pure Y_2O_3, and ZnO-Y_2O_3 composites

Sample	**Degradation efficiency (%)**	**Degradation Rate k_{app} (min^{-1})**
Pure ZnO	77	0.009
ZnO-2.5Y_2O_3	96.8	0.0227
ZnO-5Y_2O_3	98.4	0.0242
ZnO-10Y_2O_3	88.7	0.0148
ZnO-20Y_2O_3	84.2	0.0112
Pure Y_2O_3	-	-

The efficiency of MB photodegradation is highly dependent on various experimental factors, including the amount of catalyst used, light intensity (which is influenced by the distance between the light source and the solution) and the type of light source. Despite the limitations of our testing conditions, we have provided data on the photodegradation of MB using different ZnO-based materials in Table 4.4 for comparative purposes. As highlighted earlier, studies that simultaneously explore the combination of ZnO and Y_2O_3 materials to enhance photocatalytic performance are scarce in the literature. To address this, we have included all relevant studies on these

materials, along with several other ZnO-based photocatalysts, in the table. From the comparison of the photodegradation rate constant (k_{app}), it is clear that our ZnO-5Y_2O_3 sample exhibited superior photocatalytic activity in comparison to other photocatalysts.

Table 4.4 Comparison of the photocatalytic performance of composite ZnO-5Y_2O_3 with reported studies in the literature

Photocatalyst	**Synthesis technique**	**Dye**	**Light source and time (min)**	**Efficiency of improved ZnO (%)**	**k_{app} value of pure ZnO (min^{-1})**	**k_{app} value of improved ZnO (min^{-1})**	**Ref.**
ZnO-Y_2O_3 Nanocomposite	Mechanical mixing	MB	UV 150	98.4	0.009	0.0242 (2.68-fold improvement)	This study
ZnO-Y_2O_3 Nanocomposite	Coprecipitation	MB	Xenon 120	96	0.013	0.0161 (1.23-fold improvement)	(Nachimuthu et al., 2023)
Y_2O_3 coated ZnO	Mechano-thermal	Sulfamethazine	UV 180	97.1	0.014	0.017 (1.21-fold improvement)	(Belghiti et al., 2023)
Y_2O_3 coated ZnO	Mechano-thermal	Basic yellow 28	UV 90	94.5	0.019	0.038 (2-fold improvement)	(Belghiti et al., 2023)
ZnO-Y_2O_3	Precipitation	2,4 - dinitrophenol	Xenon 100	81.2	0.0086	0.0164 (1.9-fold improvement)	(Su, Qin, Ji & Jiang, 2014)
ZnO/Cu-DPA	Mechanical grinding	MB	Visible 80	87	0.016	0.023 (1.43-fold improvement)	(Berehe et al., 2023)
Nb doped ZnO	Hydrothermal.	MB	UV 30	93.8	0.085	0.145 (1.7-fold improvement)	(Silva et al., 2024)
Cu doped ZnO	Green synthesis hydrothermal	MB	UV 75	91.3	0.015	0.025 (1.88-fold improvement)	(Karthik et al., 2022)
Ag doped ZnO	Sol-gel and chemical reduction	MB	UV 240	82.6	0.0043	0.007 (1.62-fold improvement)	(Abdel Messih, Ahmed, Soltan & Anis, 2019)
Cd doped ZnO	Wet chemical dip coating	MB	UV 360	-	0.0056	0.0085 (1.51-fold improvement)	(Shouqin Tian et al., 2019)
Sm doped ZnO	Sol-gel spin coating	MB	Sunlight 200	60	0.0027	0.0043 (1.59-fold improvement)	(Ali et al., 2019)

CHAPTER FIVE
CONCUSLUSION

Within the scope of this thesis, ZnO, Y_2O_3, YAG particles were successfully synthesized via the sol-gel method, and various combinations were obtained through mechanical mixing and precipitation methods to form the desired materials. The structural, optical, and photocatalytic properties of the synthesized materials were investigated, leading to the following conclusions:

1. FTIR and DTA-TG devices were utilized for process optimization and accurate determination of heat treatment temperatures. According to the analysis results, the heat treatment temperature for ZnO was determined to be 500^{o}C. For Y_2O_3 and YAG, it was deemed appropriate for this temperature to be 1000^{o}C. According to the FTIR results of the combined ZnO-Y_2O_3 structure formed by the precipitation method and dried 80^{o}C, organic content was observed in the dried product of the Zn precursor solution before heat treatment. However, after heat treatment, it was observed that the organic content was removed from the structure.

2. XRD analyses were conducted to determine the crystal structures of the desired phases for all pure (ZnO, Y_2O_3, YAG) and combined ZnO-Y_2O_3, ZnO-YAG, and composite ZnO-Y_2O_3, ZnO-YAG materials. It was observed that the phase structures of independently Eu and Ce doped Y_2O_3 and YAG materials were not affected by the doping process, and all final products exhibited pure and crystalline structures. Additionally, it was determined that the phase structure of Y_2O_3 produced using different amounts of acid remained unchanged with varying acid concentrations. It was observed that all materials were obtained with the desired phases. The increased amount of Y_2O_3 in the composite ZnO-Y_2O_3 samples obtained by the mechanical mixing method was demonstrated through XRD analysis. Since it is known that the composite structure contains at least 2.5% Y_2O_3 by weight, it is expected that no distinct Y_2O_3 peaks are observed in the XRD analysis of the ZnO-5Y_2O_3 material. However, along with the increasing ratio, the Y_2O_3 content in the structure was clearly observed. In the dried form of the combined ZnO-Y_2O_3 structure prepared via the precipitation method, Y_2O_3 is noticeably present, which can be attributed to the presence of crystalline Y_2O_3 already existing in the solution during the solution

preparation stage. During the precipitation process, performed using NaOH, crystalline ZnO has partially formed. However, after heat treatment, the crystallinity increased, and the dominant ZnO structure became more pronounced in the composition. Additionally, it was determined that the phase structure of Y_2O_3 produced using different amounts of acid remained unchanged with varying acid concentrations.

3. The surface morphology of the synthesized materials was observed using FE-SEM microscopy. It was observed that pure ZnO particles generally exhibit a spherical structure and possess nano sized dimensions. The morphology of Y_2O_3 material was found to be plate-like and flat, varying depending on the amount of acid used during solution preparation. The increase in surface area of Y_2O_3 with increasing acid content could be observed from SEM analyses, which was further supported by BET analysis. The combined ZnO-Y_2O_3 material prepared via precipitation method was found to have a dendritic and branched structure. It was determined that these structures are ZnO which was formed around Y_2O_3. However, it was observed through UV analysis that the photocatalytic results of the structure formed in this sharp and dendritic manner did not positively influence as much as composite ZnO-Y_2O_3.

4. Surface area analyses for the Y_2O_3 material were conducted using the BET technique. It was determined that as the amount of citric acid used during solution preparation increased, the surface area of the final Y_2O_3 material also increased. It is considered that the variation in surface area arises from the esterification reaction occurring between citric acid and ethylene glycol. It was determined that the surface area of Y_2O_3 material with an MRCM value of 0.5 was 19.1648 m^2/g, while the surface area of Y_2O_3 with an MRCM value of 2 was found to be 53.4836 m^2/g.

5. Luminescence properties were examined to elucidate the effects of phosphor materials on photocatalytic performance. It was observed that pure Y_2O_3 material emitted light in a wide range of 300-450 nm when excited at 292 nm. This emission is well fitted within the appropriate range of radiation for initiating the photocatalytic reaction of ZnO. Therefore, the emission range of Y_2O_3 overlaps with the absorption range of ZnO. In this case, energy transfer between nanoscale ZnO and Y_2O_3 particles is made possible by Y_2O_3's strong absorption from 200 to 300 nm and broad emission

from 300 to 500 nm, which covers the excitation band of ZnO. In our setup, ZnO acts as the acceptor, while Y_2O_3 acts as the donor. The energy transfer between these two materials has been confirmed with the Decay Time analyses. When energy transfer takes place from Y_2O_3 to ZnO, it is expected that the decay time of Y_2O_3 emission would decrease. This reduction occurs due to non-radiative energy transfer to ZnO, resulting in a shorter duration of Y_2O_3 in the excited state. Higher ZnO (acceptor) concentration brings Y_2O_3 (donor) and ZnO into closer proximity, potentially enhancing FRET efficiency. Consequently, more efficient energy transfer from Y_2O_3 to ZnO is facilitated, resulting in a shorter decay time for Y_2O_3 luminescence. For the sample containing 25 mg ZnO and 2.5 mg Y_2O_3 (10% Y_2O_3), a decay time value of 6.15 μs was measured, whereas for the sample containing 100 mg ZnO and 2.5 mg Y_2O_3 (2.5% Y_2O_3), this value was measured as 5.23 μs. Based on the provided data, it can be inferred that there is indeed energy transfer between Y_2O_3 and ZnO.

6. Upon examination of the luminescence properties of doped Y_2O_3 samples and all YAG samples, no suitable emission characteristics capable of exciting ZnO were found. There is no energy transfer observed between these materials and ZnO. These findings are consistent with the results observed in photocatalytic outputs.

7. The effects of all synthesized luminescent materials on photocatalytic reactions were investigated. According to the results, both Y_2O_3 and YAG materials showed no photocatalytic activity when used individually. Consistent with the luminescence results, neither pure nor doped YAG materials exhibited suitable emission characteristics, thereby failing to enhance the photocatalytic performance of ZnO when used together. Conversely, the presence of YAG material in the environment created a shading effect on ZnO, thereby deteriorating its photocatalytic performance. This hindered the efficient absorption of UV light by ZnO.

8. As pure Y_2O_3 itself does not exhibit any photocatalytic effect, it significantly enhances the photocatalytic performance of ZnO through its emissions. However, the process of doping Eu and Ce diminishes the ability of Y_2O_3 to enhance the photocatalytic performance. As the dopant concentration increases, this positive effect decreases. This phenomenon is attributed to the significant alteration in emission characteristics due to the addition of dopants. As a result of the doping process, the

emission of Y_2O_3 deviates from the wavelength suitable for exciting ZnO. The amount of pure Y_2O_3 used is also a crucial parameter affecting the photocatalytic performance of ZnO. The composite with the best performance demonstrated is the ZnO-5Y_2O_3, where the weight percentage of Y_2O_3 is 5% relative to ZnO. The degradation rate exhibited by the ZnO-5Y_2O_3 composite was 0.0242 min^{-1}, whereas pure ZnO showed a degradation rate of 0.009 min^{-1}. After 150 minutes of UV irradiation, the ZnO-5Y_2O_3 composite achieved a degradation efficiency of 98.4%, whereas for pure ZnO, it was 77%. Additionally, the ZnO-5Y_2O_3 composite material exhibited no performance degradation after 5 repeated photocatalytic analyses, indicating its reusability and stability.

9. Considering the level of photocatalytic improvement achieved, the additional production costs are deemed to be feasible. This is because the Y_2O_3 material, which is used in very small quantities and is relatively easy to produce, presents an acceptable extra cost for the resulting photocatalytic enhancement.

Based on these outputs, future planning can be conducted as follows;

The photocatalytic performance of the ZnO-Y_2O_3 composite structure is significantly influenced by the amount of Y_2O_3 present. To achieve better results, the material proportions within the composite can be tailored more precisely and in detail.

The final surface area of Y_2O_3 varies depending on the acid concentration used during solution preparation. The impact of this variation in surface area on luminescence properties and, consequently, on photocatalytic performance can be investigated.

Our newly developed approach demonstrates how photoluminescent materials can significantly enhance the performance of photocatalytic materials. Using this framework, the effects of various photoluminescent materials on photocatalytic efficiency can be systematically investigated. In particular, photoluminescent materials capable of emitting in the 300-400 nm range show strong potential as effective candidates for such applications.

REFERENCES

Abdel Messih, M. F., Ahmed, M. A., Soltan, A. & Anis, S. S. (2019). Synthesis and characterization of novel Ag/ZnO nanoparticles for photocatalytic degradation of methylene blue under UV and solar irradiation. *Journal of Physics and Chemistry of Solids, 135*, 109086.

Adam, R. E., Pozina, G., Willander, M. & Nur, O. (2018). Synthesis of ZnO nanoparticles by co-precipitation method for solar driven photodegradation of Congo red dye at different pH. *Photonics and Nanostructures-Fundamentals and Applications, 32*, 11-18.

Adán, C., Marugán, J., Sánchez, E., Pablos, C. & van Grieken, R. (2016). Understanding the effect of morphology on the photocatalytic activity of TiO2 nanotube array electrodes. *Electrochimica Acta, 191*, 521-529.

Afridha, M. S. H. F., Prakash, S. H. & Roopan, S. M. (2025). MoO3 based nanocomposites for the photocatalytic degradation of colourants – A review. *Journal of the Taiwan Institute of Chemical Engineers, 166*, 105354.

Aieta, E. M., Berg, J. D., Roberts, P. V. & Cooper, R. C. (1980). Comparison of Chlorine Dioxide and Chlorine in Wastewater Disinfection. *Journal (Water Pollution Control Federation), 52* (4), 810-822.

Akpan, U. G. & Hameed, B. H. (2009). Parameters affecting the photocatalytic degradation of dyes using TiO2-based photocatalysts: a review. *Journal of hazardous materials, 170* (2-3), 520-529.

Akpan, U. G. & Hameed, B. H. (2009). Parameters affecting the photocatalytic degradation of dyes using TiO2-based photocatalysts: A review. *Journal of Hazardous Materials, 170* (2), 520-529.

Aleshin, D. K., Mashkovtsev, M. A., Kosykh, A. S., Kuznetsova, Y. A., Zatsepin, A. F. & Rychkov, V. N. (2023). Synthesis of spherical Y2O3:Er emitting particles with variable radial composition by controlled double-jet precipitation of layered precursors. *Particuology, 74*, 92-102.

Ali, D., Butt, M. Z., Muneer, I., Farrukh, M. A., Aftab, M., Saleem, M., Bashir, F. & Khan, A. U. (2019). Synthesis and characterization of sol-gel derived La and Sm doped ZnO thin films: A solar light photo catalyst for methylene blue. *Thin Solid Films, 679*, 86-98.

Amoriello, S., Bianco, A., Eusebio, L. & Gronchi, P. (2011). Evolution of two acid steps sol–gel phases by FTIR. *Journal of Sol-Gel Science and Technology, 58* (1), 209-217.

Anil Kumar, Y., Koyyada, G., Ramachandran, T., Kim, J. H., Hegazy, H. H., Singh, S. & Moniruzzaman, M. (2023). Recent advancement in quantum dot-based materials for energy storage applications: a review. *Dalton Transactions, 52* (25), 8580-8600.

Asahi, R., Morikawa, T., Ohwaki, T., Aoki, K. & Taga, Y. (2001). Visible-Light Photocatalysis in Nitrogen-Doped Titanium Oxides. *Science, 293* (5528), 269-271.

Ba-Abbad, M. M., Kadhum, A. A. H., Bakar Mohamad, A., Takriff, M. S. & Sopian, K. (2013). The effect of process parameters on the size of ZnO nanoparticles synthesized via the sol–gel technique. *Journal of Alloys and Compounds, 550*, 63-70.

Bajorowicz, B., Kobylański, M. P., Gołąbiewska, A., Nadolna, J., Zaleska-Medynska, A. & Malankowska, A. (2018). Quantum dot-decorated semiconductor micro- and nanoparticles: A review of their synthesis, characterization and application in photocatalysis. *Advances in Colloid and Interface Science, 256*, 352-372.

Balayeva, N. O., Fleisch, M. & Bahnemann, D. W. (2018). Surface-grafted WO3/TiO2 photocatalysts: Enhanced visible-light activity towards indoor air purification. *Catalysis Today, 313*, 63-71.

Ballari, M. d. l. M., Brandi, R., Alfano, O. & Cassano, A. (2008). Mass transfer limitations in photocatalytic reactors employing titanium dioxide suspensions: I. Concentration profiles in the bulk. *Chemical Engineering Journal, 136* (1), 50-65.

Barhoum, A., Van Assche, G., Rahier, H., Fleisch, M., Bals, S., Delplancked, M.-P., Leroux, F. & Bahnemann, D. (2017). Sol-gel hot injection synthesis of ZnO nanoparticles into a porous silica matrix and reaction mechanism. *Materials & Design, 119*, 270-276.

Baruah, S. & Dutta, J. (2009). Hydrothermal growth of ZnO nanostructures. *Science and technology of advanced materials*.

Bayarri, B., Abellán, M. N., Giménez, J. & Esplugas, S. (2007). Study of the wavelength effect in the photolysis and heterogeneous photocatalysis. *Catalysis Today, 129* (1), 231-239.

Belghiti, M., El Mersly, L., Tanji, K., Belkodia, K., Lamsayety, I., Ouzaouit, K., Faqir, H., Benzakour, I., Rafqah, S. & Outzourhit, A. (2023). Sol-gel combined mechano-thermal synthesis of Y2O3, CeO2, and PdO partially coated ZnO for sulfamethazine and basic yellow 28 photodegradation under UV and visible light. *Optical Materials, 136*, 113458.

Benabbou, A. K., Derriche, Z., Felix, C., Lejeune, P. & Guillard, C. (2007). Photocatalytic inactivation of Escherischia coli: Effect of concentration of TiO2 and microorganism, nature, and intensity of UV irradiation. *Applied Catalysis B: Environmental, 76* (3), 257-263.

Berehe, B. A., Assen, A. H., Kumar, A. S. K., Ulla, H., Duma, A. D., Chang, J.-Y., Gedda, G. & Girma, W. M. (2023). Highly efficient visible light active ZnO/Cu-DPA composite photocatalysts for the treatment of wastewater contaminated with organic dye. *Scientific Reports, 13* (1), 16454.

Bhosle, V., Tiwari, A. & Narayan, J. (2006). Metallic conductivity and metal-semiconductor transition in Ga-doped ZnO. *Applied Physics Letters, 88* (3).

Bizarro, M. (2010). High photocatalytic activity of ZnO and ZnO:Al nanostructured films deposited by spray pyrolysis. *Applied Catalysis B: Environmental, 97* (1), 198-203.

Bomila, R., Suresh, S. & Srinivasan, S. (2019). Synthesis, characterization and comparative studies of dual doped ZnO nanoparticles for photocatalytic applications. *Journal of Materials Science: Materials in Electronics, 30* (1), 582-592.

Boonprakob, N., Wetchakun, N., Phanichphant, S., Waxler, D., Sherrell, P., Nattestad, A., Chen, J. & Inceesungvorn, B. (2014). Enhanced visible-light photocatalytic activity of g-C3N4/TiO2 films. *Journal of Colloid and Interface Science, 417*, 402-409.

Bose, P. P., Gupta, M. K., Mittal, R., Rols, S., Achary, S. N., Tyagi, A. K. & Chaplot, S. L. (2011). Phase transitions and thermodynamic properties of yttria, Y2O3: Inelastic neutron scattering shell model and first-principles calculations. *Physical Review B, 84* (9), 094301.

Boukerika, A. & Guerbous, L. (2014). Annealing effects on structural and luminescence properties of red Eu3+-doped Y2O3 nanophosphors prepared by sol–gel method. *Journal of Luminescence, 145*, 148-153.

Boyer, D., Bertrand-Chadeyron, G. & Mahiou, R. (2004). Structural and optical characterizations of YAG:Eu3+ elaborated by the sol–gel process. *Optical Materials, 26* (2), 101-105.

Brunauer, S., Emmett, P. H. & Teller, E. (1938). Adsorption of Gases in Multimolecular Layers. *Journal of the American Chemical Society, 60* (2), 309-319.

Burkhard, R., Deletic, A. & Craig, A. (2000). Techniques for water and wastewater management: a review of techniques and their integration in planning. *Urban Water, 2* (3), 197-221.

Callister, W. D. & Rethwisch, D. G. (2007). *Materials science and engineering: an introduction*: Wiley New York.

Campbell, A. K. (1988). Chemiluminescence. Principles and applications in biology and medicine.

Carp, O., Huisman, C. L. & Reller, A. (2004). Photoinduced reactivity of titanium dioxide. *Progress in solid state chemistry, 32* (1-2), 33-177.

Chambers, J. & Parsons, G. (2001). Physical and electrical characterization of ultrathin yttrium silicate insulators on silicon. *Journal of applied physics, 90* (2), 918-933.

Chao, W.-H., Wu, R.-J. & Wu, T.-B. (2010). Structural and luminescent properties of YAG:Ce thin film phosphor. *Journal of Alloys and Compounds, 506* (1), 98-102.

Chavali, M. S. & Nikolova, M. P. (2019). Metal oxide nanoparticles and their applications in nanotechnology. *SN Applied Sciences, 1* (6), 607.

Chen, D., Xiang, W., Liang, X., Zhong, J., Yu, H., Ding, M., Lu, H. & Ji, Z. (2015). Advances in transparent glass–ceramic phosphors for white light-emitting diodes—A review. *Journal of the European Ceramic Society, 35* (3), 859-869.

Chen, D., Cheng, Y., Zhou, N., Chen, P., Wang, Y., Li, K., Huo, S., Cheng, P., Peng, P., Zhang, R., Wang, L., Liu, H., Liu, Y. & Ruan, R. (2020). Photocatalytic degradation of organic pollutants using TiO2-based photocatalysts: A review. *Journal of Cleaner Production, 268*, 121725.

Chen, F. (2012). Micro-and submicrometric waveguiding structures in optical crystals produced by ion beams for photonic applications. *Laser & Photonics Reviews, 6* (5), 622-640.

Chen, X., Wu, Z., Liu, D. & Gao, Z. (2017). Preparation of ZnO Photocatalyst for the Efficient and Rapid Photocatalytic Degradation of Azo Dyes. *Nanoscale Research Letters, 12* (1), 143.

Chen, Y.-W. & Hsu, Y.-H. (2021). Effects of Reaction Temperature on the Photocatalytic Activity of TiO2 with Pd and Cu Cocatalysts. *Catalysts, 11* (8), 966.

da Silva Júnior, M. G., Arzuza, L. C. C., Sales, H. B., Farias, R. M. d. C., Neves, G. d. A., Lira, H. d. L. & Menezes, R. R. (2023). A Brief Review of MoO3 and MoO3-Based Materials and Recent Technological Applications in Gas Sensors, Lithium-Ion Batteries, Adsorption, and Photocatalysis. *Materials, 16* (24), 7657.

de Andrade Gomes, M., Ernesto Giroldo Valerio, M. & Soares Macedo, Z. (2011). Particle Size Control of Y2O3:Eu3+ Prepared via a Coconut Water-Assisted Sol-Gel Method. *Journal of Nanomaterials, 2011* (1), 469685.

Dean, P. J. (1982). Photoluminescence as a diagnostic of semiconductors. *Progress in Crystal Growth and Characterization, 5* (1), 89-174.

Degen, A. & Kosec, M. (2000). Effect of pH and impurities on the surface charge of zinc oxide in aqueous solution. *Journal of the European Ceramic Society, 20* (6), 667-673.

Demchenko, A. P. (2015). Fluorescence Detection Techniques. In *Introduction to Fluorescence Sensing* (69-132). Cham: Springer International Publishing.

Demirci, S., Dikici, T., Yurddaskal, M., Gultekin, S., Toparli, M. & Celik, E. (2016). Synthesis and characterization of Ag doped TiO2 heterojunction films and their photocatalytic performances. *Applied Surface Science, 390*, 591-601.

Demirci, S., Dikici, T., Tünçay, M. M. & Kaya, N. (2020). A study of heating rate effect on the photocatalytic performances of ZnO powders prepared by sol-gel route: Their kinetic and thermodynamic studies. *Applied Surface Science, 507*, 145083.

Di Mauro, A., Cantarella, M., Nicotra, G., Pellegrino, G., Gulino, A., Brundo, M. V., Privitera, V. & Impellizzeri, G. (2017). Novel synthesis of ZnO/PMMA nanocomposites for photocatalytic applications. *Scientific Reports, 7* (1), 40895.

Dikici, T. & Demirci, S. (2019). Influence of thermal oxidation temperature on the microstructure and photoelectrochemical properties of ZnO nanostructures fabricated on the zinc scraps. *Journal of Alloys and Compounds, 779*, 752-761.

Djurišić, A. B., He, Y. & Ng, A. M. C. (2020). Visible-light photocatalysts: Prospects and challenges. *APL Materials, 8* (3).

Dobrozhan, O., Klymov, O., Agouram, S., Martínez-Tomás, C., Muñoz-Sanjosé, V. & Opanasyuk, A. (2024). Grain growth of ZnO nanocrystals synthesized in polyol

medium with polyvinylpyrrolidone additives. *Ceramics International, 50* (4), 6941-6949.

Dobson, K. D. & McQuillan, A. J. (1997). An Infrared Spectroscopic Study of Carbonate Adsorption to Zirconium Dioxide Sol−Gel Films from Aqueous Solutions. *Langmuir, 13* (13), 3392-3396.

Dong, H., Zeng, G., Tang, L., Fan, C., Zhang, C., He, X. & He, Y. (2015). An overview on limitations of TiO2-based particles for photocatalytic degradation of organic pollutants and the corresponding countermeasures. *Water Research, 79*, 128-146.

Dubey, V., Agrawal, S. & Kaur, J. (2015). Photoluminescence and thermoluminescence behavior of Gd doped Y2O3 phosphor. *Optik, 126* (1), 1-5.

Dupont, A., Parent, C., Le Garrec, B. & Heintz, J. M. (2003). Size and morphology control of Y2O3 nanopowders via a sol–gel route. *Journal of Solid State Chemistry, 171* (1), 152-160.

Durose, K., Asher, S. E., Jaegermann, W., Levi, D., McCandless, B. E., Metzger, W., Moutinho, H., Paulson, P. D., Perkins, C. L., Sites, J. R., Teeter, G. & Terheggen, M. (2004). Physical characterization of thin-film solar cells. *Progress in Photovoltaics: Research and Applications, 12* (2-3), 177-217.

Edgar, A. (2017). Luminescent Materials. In *Springer Handbook of Electronic and Photonic Materials* (1-1). Cham: Springer International Publishing.

Empedocles, S. A., Neuhauser, R., Shimizu, K. & Bawendi, M. G. (1999). Photoluminescence from Single Semiconductor Nanostructures. *Advanced Materials, 11* (15), 1243-1256.

Esplugas, S., Gimenez, J., Contreras, S., Pascual, E. & Rodríguez, M. (2002). Comparison of different advanced oxidation processes for phenol degradation. *Water Research, 36* (4), 1034-1042.

Fadlalla, H. M. H., Tang, C. C., Elssfah, E. M. & Shi, F. (2008). Synthesis and characterization of single crystalline YAG:Eu nano-sized powder by sol–gel method. *Materials Chemistry and Physics, 109* (2), 436-439.

Fajrina, N. & Tahir, M. (2019). A critical review in strategies to improve photocatalytic water splitting towards hydrogen production. *International Journal of Hydrogen Energy, 44* (2), 540-577.

Fan, H., Zhao, X., Yang, J., Shan, X., Yang, L., Zhang, Y., Li, X. & Gao, M. (2012). ZnO–graphene composite for photocatalytic degradation of methylene blue dye. *Catalysis Communications, 29*, 29-34.

Fang, S., Rahaman, M., Bharti, J., Reisner, E., Robert, M., Ozin, G. A. & Hu, Y. H. (2023). Photocatalytic CO2 reduction. *Nature Reviews Methods Primers, 3* (1), 61.

Farhadian, N., Akbarzadeh, R., Pirsaheb, M., Jen, T.-C., Fakhri, Y. & Asadi, A. (2019). Chitosan modified N, S-doped TiO2 and N, S-doped ZnO for visible light photocatalytic degradation of tetracycline. *International Journal of Biological Macromolecules, 132*, 360-373.

Farley, N. R., Staddon, C. R., Zhao, L., Edmonds, K. W., Gallagher, B. L. & Gregory, D. H. (2004). Sol-gel formation of ordered nanostructured doped ZnO films. *Journal of Materials Chemistry, 14* (7), 1087-1092.

Fereidooni, M., Márquez, V., Gholami, R., Paz, C. V., Villanueva, M. S., Kanjanaboos, P., Kamjam, N., Khan, R. A., Praserthdam, S. & Praserthdam, P. (2024). Transforming sunlight through ultrasonically engineered ZnO and g-C_3N_4 Z-scheme heterostructure for superior photocatalysis: Experimental and theoretical study. *Materials Research Bulletin, 180*, 113034.

Fernández-Pérez, A. & Marbán, G. (2022). Visible Light Spectroscopic Analysis of Methylene Blue in Water. *Journal of Applied Spectroscopy, 88* (6), 1284-1290.

Fouda, A., El-Din Hassan, S., Salem, S. S. & Shaheen, T. I. (2018). In-Vitro cytotoxicity, antibacterial, and UV protection properties of the biosynthesized Zinc oxide nanoparticles for medical textile applications. *Microbial Pathogenesis, 125*, 252-261.

Friend, R. H., Denton, G. J., Halls, J. J. M., Harrison, N. T., Holmes, A. B., Köhler, A., Lux, A., Moratti, S. C., Pichler, K., Tessler, N., Towns, K. & Wittmann, H. F.

(1997). Electronic excitations in luminescent conjugated polymers. *Solid State Communications, 102* (2), 249-258.

Fu, L., Guo, Y., Pan, S., Huang, J. & Wang, L. (2019). Core-shell type Tourmaline@ZnO composites equipped with carbon dots for high efficiency photocatalyst. *Surface and Coatings Technology, 359,* 190-196.

Fu, Y., Ren, Z., Wu, J., Li, Y., Liu, W., Li, P., Xing, L., Ma, J., Wang, H. & Xue, X. (2021). Direct Z-scheme heterojunction of ZnO/MoS2 nanoarrays realized by flowing-induced piezoelectric field for enhanced sunlight photocatalytic performances. *Applied Catalysis B: Environmental, 285,* 119785.

Fujishima, A. & Honda, K. (1972). Electrochemical Photolysis of Water at a Semiconductor Electrode. *Nature, 238* (5358), 37-38.

Fujita, S., Yoshihara, S., Sakamoto, A., Yamamoto, S. & Tanabe, S. (2005). YAG glass-ceramic phosphor for white LED (I): background and development *Fifth International Conference on Solid State Lighting* (Vol. 5941, 594111): International Society for Optics and Photonics.

Gajović, A., Tomašić, N., Djerdj, I., Su, D. S. & Furić, K. (2008). Influence of mechanochemical processing to luminescence properties in Y2O3 powder. *Journal of Alloys and Compounds, 456* (1), 313-319.

Gao, P., Liu, Z. & Sun, D. D. (2013). The synergetic effect of sulfonated graphene and silver as co-catalysts for highly efficient photocatalytic hydrogen production of ZnO nanorods. *Journal of Materials Chemistry A, 1* (45), 14262-14269.

Gaya, U. I. & Abdullah, A. H. (2008). Heterogeneous photocatalytic degradation of organic contaminants over titanium dioxide: a review of fundamentals, progress and problems. *Journal of photochemistry and photobiology C: Photochemistry reviews, 9* (1), 1-12.

Ghorbani, S., Razavi, R. S., Loghman-Estarki, M. & Alhaji, A. (2017). Synthesis of MgO-Y2O3 composite nanopowder with a high specific surface area by the Pechini method. *Ceramics International, 43* (1), 345-354.

Ghorbani, S., Razavi, R. S., Loghman-Estarki, M. R. & Alhaji, A. (2017). Synthesis of MgO-Y2O3 composite nanopowder with a high specific surface area by the Pechini method. *Ceramics International, 43* (1, Part A), 345-354.

Giancaterini, L., Cantalini, C., Cittadini, M., Sturaro, M., Guglielmi, M., Martucci, A., Resmini, A. & Anselmi-Tamburini, U. (2015). Au and Pt Nanoparticles Effects on the Optical and Electrical Gas Sensing Properties of Sol–Gel-Based ZnO Thin-Film Sensors. *IEEE Sensors Journal, 15* (2), 1068-1076.

Gowda, G. (1986). Synthesis of yttrium aluminates by the sol-gel process. *Journal of Materials Science Letters, 5* (10), 1029-1032.

Graham, J. D. & Hammer, N. I. (2012). Photocatalytic Water Splitting and Carbon Dioxide Reduction. In *Handbook of Climate Change Mitigation* (1755-1780). New York, NY: Springer US.

Gregory, J. & Dhond, R. V. (1972). Wastewater treatment by ion exchange. *Water Research, 6* (6), 681-694.

Gu, X., Lin, S., Qi, K., Yan, Y., Li, R., Popkov, V. & Almjasheva, O. (2024). Application of tungsten oxide and its composites in photocatalysis. *Separation and Purification Technology, 345*, 127299.

Guo, H., Zhang, W., Lou, L., Brioude, A. & Mugnier, J. (2004). Structure and optical properties of rare earth doped Y2O3 waveguide films derived by sol–gel process. *Thin Solid Films, 458* (1), 274-280.

Gurylev, V. (2021). Photocatalysis: Fundamentals. In *Nanostructured Photocatalyst via Defect Engineering: Basic Knowledge and Recent Advances* (1-36). Cham: Springer International Publishing.

Gültekin, S., Yıldırım, S., Yılmaz, O., Keskin, İ. Ç., Katı, M. İ. & Çelik, E. (2019). Structural and optical properties of SrAl2O4: Eu2+/Dy3+ phosphors synthesized by flame spray pyrolysis technique. *Journal of Luminescence, 206*, 59-69.

Habisreutinger, S. N., Schmidt-Mende, L. & Stolarczyk, J. K. (2013). Photocatalytic Reduction of CO2 on TiO2 and Other Semiconductors. *Angewandte Chemie International Edition, 52* (29), 7372-7408.

Hamelmann, F. U. (2016). Thin film zinc oxide deposited by CVD and PVD. *Journal of Physics: Conference Series, 764* (1), 012001.

Hanaor, D. A. H., Ghadiri, M., Chrzanowski, W. & Gan, Y. (2014). Scalable Surface Area Characterization by Electrokinetic Analysis of Complex Anion Adsorption. *Langmuir, 30* (50), 15143-15152.

Harun, K., Salleh, N. A., Deghfel, B., Yaakob, M. K. & Mohamad, A. A. (2020). DFT + U calculations for electronic, structural, and optical properties of ZnO wurtzite structure: A review. *Results in Physics, 16*, 102829.

Hasnidawani, J., Azlina, H., Norita, H., Bonnia, N., Ratim, S. & Ali, E. (2016). Synthesis of ZnO nanostructures using sol-gel method. *Procedia Chemistry, 19*, 211-216.

Hassanzadeh-Tabrizi, S. A., Taheri-Nassaj, E. & Sarpoolaky, H. (2008). Synthesis of an alumina–YAG nanopowder via sol–gel method. *Journal of Alloys and Compounds, 456* (1), 282-285.

Hassanzadeh-Tabrizi, S. A. (2011). Low temperature synthesis and luminescence properties of YAG: Eu nanopowders prepared by modified sol-gel method. *Transactions of Nonferrous Metals Society of China, 21* (11), 2443-2447.

Hench, L. L. & West, J. K. (1990). The sol-gel process. *Chemical Reviews, 90* (1), 33-72.

Hoang, V. C., Dave, K. & Gomes, V. G. (2019). Carbon quantum dot-based composites for energy storage and electrocatalysis: Mechanism, applications and future prospects. *Nano Energy, 66*, 104093.

Hoffmann, M. R., Martin, S. T., Choi, W. & Bahnemann, D. W. (1995). Environmental Applications of Semiconductor Photocatalysis. *Chemical Reviews, 95* (1), 69-96.

Hong, J., Katsumata, K.-i. & Matsushita, N. (2016). Fabrication of Al-Doped ZnO Film with High Conductivity Induced by Photocatalytic Activity. *Journal of Electronic Materials, 45* (10), 4875-4880.

Hong, R., Li, J., Chen, L., Liu, D., Li, H., Zheng, Y. & Ding, J. (2009). Synthesis, surface modification and photocatalytic property of ZnO nanoparticles. *Powder Technology, 189* (3), 426-432.

Hosseini, S. M., Sarsari, I. A., Kameli, P. & Salamati, H. (2015). Effect of Ag doping on structural, optical, and photocatalytic properties of ZnO nanoparticles. *Journal of Alloys and Compounds, 640*, 408-415.

Huber, F., Madel, M., Reiser, A., Bauer, S. & Thonke, K. (2016). New CVD-based method for the growth of high-quality crystalline zinc oxide layers. *Journal of Crystal Growth, 445*, 58-62.

Huber, G., Kränkel, C. & Petermann, K. (2010). Solid-state lasers: status and future. *JOSA B, 27* (11), B93-B105.

Hunge, Y. M., Yadav, A. A. & Mathe, V. L. (2019). Photocatalytic hydrogen production using TiO2 nanogranules prepared by hydrothermal route. *Chemical Physics Letters, 731*, 136582.

Huo, P., Zhou, M., Tang, Y., Liu, X., Ma, C., Yu, L. & Yan, Y. (2016). Incorporation of N–ZnO/CdS/Graphene oxide composite photocatalyst for enhanced photocatalytic activity under visible light. *Journal of Alloys and Compounds, 670*, 198-209.

Husson, E., Proust, C., Gillet, P. & Itié, J. P. (1999). Phase transitions in yttrium oxide at high pressure studied by Raman spectroscopy. *Materials Research Bulletin, 34* (12), 2085-2092.

Ikesue, A., Furusato, I. & Kamata, K. (1995). Fabrication of polycrystal line, transparent YAG ceramics by a solid-state reaction method. *Journal of the American Ceramic Society, 78* (1), 225-228.

Ikesue, A., Kinoshita, T., Kamata, K. & Yoshida, K. (1995). Fabrication and optical properties of high-performance polycrystalline Nd: YAG ceramics for solid-state lasers. *Journal of the American Ceramic Society, 78* (4), 1033-1040.

Ilican, S., Caglar, Y., Caglar, M. & Yakuphanoglu, F. (2006). Electrical conductivity, optical and structural properties of indium-doped ZnO nanofiber thin film deposited by spray pyrolysis method. *Physica E: Low-dimensional Systems and Nanostructures, 35* (1), 131-138.

Iqbal, S. & Liu, J. (2024). Unveiling S-scheme synergies: Synthesis and photocatalytic advancement of Au NRs-infused Fe_2O_3QDs/g-C_3N_4 hybrids–A new frontier in visible light-driven water splitting. *Journal of Environmental Chemical Engineering, 12* (6), 114866.

Ismael, M. (2020). A review on graphitic carbon nitride (g-C3N4) based nanocomposites: Synthesis, categories, and their application in photocatalysis. *Journal of Alloys and Compounds, 846*, 156446.

Itoh, T. (2012). Fluorescence and Phosphorescence from Higher Excited States of Organic Molecules. *Chemical Reviews, 112* (8), 4541-4568.

Jiang, J.-Q. & Lloyd, B. (2002). Progress in the development and use of ferrate(VI) salt as an oxidant and coagulant for water and wastewater treatment. *Water Research, 36* (6), 1397-1408.

Jiang, L. & Gao, L. (2005). Fabrication and characterization of ZnO-coated multi-walled carbon nanotubes with enhanced photocatalytic activity. *Materials Chemistry and Physics, 91* (2), 313-316.

Jiang, L., Yuan, X., Pan, Y., Liang, J., Zeng, G., Wu, Z. & Wang, H. (2017). Doping of graphitic carbon nitride for photocatalysis: A review. *Applied Catalysis B: Environmental, 217*, 388-406.

Jimenez-Cadena, G., Comini, E., Ferroni, M., Vomiero, A. & Sberveglieri, G. (2010). Synthesis of different ZnO nanostructures by modified PVD process and potential

use for dye-sensitized solar cells. *Materials Chemistry and Physics, 124* (1), 694-698.

Jin, L., Zhao, H., Wang, Z. M. & Rosei, F. (2021). Quantum Dots-Based Photoelectrochemical Hydrogen Evolution from Water Splitting. *Advanced Energy Materials, 11* (12), 2003233.

Jing, S., Zhao, Y., Sun, R.-C., Zhong, L. & Peng, X. (2019). Facile and High-Yield Synthesis of Carbon Quantum Dots from Biomass-Derived Carbons at Mild Condition. *ACS Sustainable Chemistry & Engineering, 7* (8), 7833-7843.

Jose, T., Vincent, C., Lilly, K. O. & Lazar, M. A. (2019). Selective photocatalytic dye degradation by surface charged TiO2. *Materials Today: Proceedings, 9*, 21-26.

Jubu, P. R., Obaseki, O. S., Nathan-Abutu, A., Yam, F. K., Yusof, Y. & Ochang, M. B. (2022). Dispensability of the conventional Tauc's plot for accurate bandgap determination from UV–vis optical diffuse reflectance data. *Results in Optics, 9*, 100273.

Jüstel, T., Nikol, H. & Ronda, C. (1998). New developments in the field of luminescent materials for lighting and displays. *Angewandte Chemie International Edition, 37* (22), 3084-3103.

Kamarulzaman, N., Kasim, M. F. & Rusdi, R. (2015). Band Gap Narrowing and Widening of ZnO Nanostructures and Doped Materials. *Nanoscale Research Letters, 10* (1), 346.

Kaplan, I. G. (2017). *The Pauli exclusion principle: origin, verifications, and applications*: John Wiley & Sons.

Karabunarliev, S. & Bittner, E. R. (2003). Spin-Dependent Electron-Hole Capture Kinetics in Luminescent Conjugated Polymers. *Physical Review Letters, 90* (5), 057402.

Karimi Estahbanati, M. R., Mahinpey, N., Feilizadeh, M., Attar, F. & Iliuta, M. C. (2019). Kinetic study of the effects of pH on the photocatalytic hydrogen production from alcohols. *International Journal of Hydrogen Energy, 44* (60), 32030-32041.

Karthik, K. V., Raghu, A. V., Reddy, K. R., Ravishankar, R., Sangeeta, M., Shetti, N. P. & Reddy, C. V. (2022). Green synthesis of Cu-doped ZnO nanoparticles and its application for the photocatalytic degradation of hazardous organic pollutants. *Chemosphere, 287*, 132081.

Kazeminezhad, I. & Sadollahkhani, A. (2016). Influence of pH on the photocatalytic activity of ZnO nanoparticles. *Journal of Materials Science: Materials in Electronics, 27* (5), 4206-4215.

Keyvani, A., Bahamirian, M. & Esmaeili, B. (2020). Sol-gel synthesis and characterization of ZrO2-25wt.%CeO2-2.5wt.%Y2O3 (CYSZ) nanoparticles. *Ceramics International, 46* (13), 21284-21291.

Khachatourian, A. M., Golestani-Fard, F., Sarpoolaky, H., Vogt, C., Vasileva, E., Mensi, M., Popov, S. & Toprak, M. S. (2016). Microwave synthesis of Y2O3:Eu3+ nanophosphors: A study on the influence of dopant concentration and calcination temperature on structural and photoluminescence properties. *Journal of Luminescence, 169*, 1-8.

Kidyarov, B. & Atuchin, V. (2007). Universal crystal classification system "Point symmetry–Physical property". *Ferroelectrics, 360* (1), 96-99.

Kilinc, E., Demirci, S., Uysal, F., Celik, E. & Kurt, H. (2017). High temperature thermopower of sol–gel processed Zn 1− x− y Al x Me y O (Me: Ga, In). *Journal of Materials Science: Materials in Electronics, 28* (16), 11769-11778.

Koe, W. S., Lee, J. W., Chong, W. C., Pang, Y. L. & Sim, L. C. (2020). An overview of photocatalytic degradation: photocatalysts, mechanisms, and development of photocatalytic membrane. *Environmental Science and Pollution Research, 27* (3), 2522-2565.

Kong, L. B., Huang, Y., Que, W., Zhang, T., Li, S., Zhang, J., Dong, Z. & Tang, D. (2015). Transparent ceramic materials. In *Transparent Ceramics* (29-91): Springer.

Konrad, A., Herr, U., Tidecks, R., Kummer, F. & Samwer, K. (2001). Luminescence of bulk and nanocrystalline cubic yttria. *Journal of applied physics, 90* (7), 3516-3523.

Konstantinou, I. K. & Albanis, T. A. (2004). TiO2-assisted photocatalytic degradation of azo dyes in aqueous solution: kinetic and mechanistic investigations: a review. *Applied Catalysis B: Environmental, 49* (1), 1-14.

Kosyanov, D. Y., Liu, X., Vornovskikh, A. A., Kosianova, A. A., Zakharenko, A. M., Zavjalov, A. P., Shichalin, O. O., Mayorov, V. Y., Kuryavyi, V. G., Qian, X., Zou, J. & Li, J. (2021). Al2O3–Ce:YAG and Al2O3–Ce:(Y,Gd)AG composite ceramics for high brightness lighting: Effect of microstructure. *Materials Characterization, 172*, 110883.

Köhler, A. & Bässler, H. (2009). Triplet states in organic semiconductors. *Materials Science and Engineering: R: Reports, 66* (4), 71-109.

Krauss, W. & Birringer, R. (1997). Metastable phases synthesized by inert-gas-condensation. *Nanostructured Materials, 9* (1), 109-112.

Kulmala, S. & Suomi, J. (2003). Current status of modern analytical luminescence methods. *Analytica Chimica Acta, 500* (1), 21-69.

Kumar, Y., Pal, M., Herrera, M. & Mathew, X. (2016). Effect of Eu ion incorporation on the emission behavior of Y2O3 nanophosphors: A detailed study of structural and optical properties. *Optical Materials, 60*, 159-168.

Lahewil, A. S. Z., Zyoud, S. H., Ahmed, N. M., Omar, A. F. & Azman, N. Z. N. (2022). Synthesis ZnO nanoclusters micro active area using continues wave blue laser-assisted chemical bath deposition based on UV photodetector. *Optik, 260*, 169099.

Lai, Y., Sun, L., Chen, Y., Zhuang, H., Lin, C. & Chin, J. W. (2006). Effects of the Structure of TiO2 Nanotube Array on Ti Substrate on Its Photocatalytic Activity. *Journal of The Electrochemical Society, 153* (7), D123.

Lamiri, L., Guerbous, L., Samah, M., Boukerika, A. & Ouhenia, S. (2015). Structural, morphological and steady state photoluminescence spectroscopy studies of red

Eu3+-doped Y2O3 nanophosphors prepared by the sol-gel method. *Luminescence, 30* (8), 1336-1343.

Landi, S., Segundo, I. R., Freitas, E., Vasilevskiy, M., Carneiro, J. & Tavares, C. J. (2022). Use and misuse of the Kubelka-Munk function to obtain the band gap energy from diffuse reflectance measurements. *Solid State Communications, 341*, 114573.

Lapham, D. P. & Lapham, J. L. (2019). BET surface area measurement of commercial magnesium stearate by krypton adsorption in preference to nitrogen adsorption. *International Journal of Pharmaceutics, 568*, 118522.

Latynina, A., Watanabe, M., Inomata, D., Aoki, K., Sugahara, Y., Víllora, E. G. & Shimamura, K. (2013). Properties of Czochralski grown Ce, Gd: Y3Al5O12 single crystal for white light-emitting diode. *Journal of Alloys and Compounds, 553*, 89-92.

Lawes, G. (1987). Scanning electron microscopy and X-ray microanalysis.

Lee, J., Sorescu, D. C. & Deng, X. (2016). Tunable Lattice Constant and Band Gap of Single- and Few-Layer ZnO. *The Journal of Physical Chemistry Letters, 7* (7), 1335-1340.

Lee, K. M., Lai, C. W., Ngai, K. S. & Juan, J. C. (2016). Recent developments of zinc oxide based photocatalyst in water treatment technology: A review. *Water Research, 88*, 428-448.

Lee, M. K., Park, E. K., Park, J. J. & Rhee, C. K. (2013). Control of Y2O3 phase and its nanostructure formation through a very high energy mechanical milling. *Journal of Solid State Chemistry, 201*, 56-62.

Lei, J., Chen, Y., Shen, F., Wang, L., Liu, Y. & Zhang, J. (2015). Surface modification of TiO2 with g-C3N4 for enhanced UV and visible photocatalytic activity. *Journal of Alloys and Compounds, 631*, 328-334.

Li, D. & Haneda, H. (2003). Morphologies of zinc oxide particles and their effects on photocatalysis. *Chemosphere, 51* (2), 129-137.

Li Puma, G. & Brucato, A. (2007). Dimensionless analysis of slurry photocatalytic reactors using two-flux and six-flux radiation absorption–scattering models. *Catalysis Today, 122* (1), 78-90.

Li, X., Xia, X., Xu, H., Zhong, S. & He, D. (2019). High-temperature high pressure synthesis of monoclinic Y2O3. *Materials Letters, 239*, 82-85.

Li, Z., Wang, S., Wu, J. & Zhou, W. (2022). Recent progress in defective TiO2 photocatalysts for energy and environmental applications. *Renewable and Sustainable Energy Reviews, 156*, 111980.

Lie, L. H., Duerdin, M., Tuite, E. M., Houlton, A. & Horrocks, B. R. (2002). Preparation and characterisation of luminescent alkylated-silicon quantum dots. *Journal of Electroanalytical Chemistry, 538-539*, 183-190.

Limpouchová, Z. & Procházka, K. (2016). Theoretical Principles of Fluorescence Spectroscopy. In *Fluorescence Studies of Polymer Containing Systems* (91-149). Cham: Springer International Publishing.

Lin, J., Pan, Z. & Wang, X. (2014). Photochemical Reduction of CO2 by Graphitic Carbon Nitride Polymers. *ACS Sustainable Chemistry & Engineering, 2* (3), 353-358.

Liqiang, J., Yichun, Q., Baiqi, W., Shudan, L., Baojiang, J., Libin, Y., Wei, F., Honggang, F. & Jiazhong, S. (2006). Review of photoluminescence performance of nano-sized semiconductor materials and its relationships with photocatalytic activity. *Solar Energy Materials and Solar Cells, 90* (12), 1773-1787.

Liu, D., Lv, Y., Zhang, M., Liu, Y., Zhu, Y., Zong, R. & Zhu, Y. (2014). Defect-related photoluminescence and photocatalytic properties of porous ZnO nanosheets. *Journal of Materials Chemistry A, 2* (37), 15377-15388.

Liu, J., Zhang, H., Tang, D., Zhang, X., Yan, L., Han, Y., Huang, H., Liu, Y. & Kang, Z. (2014). Carbon Quantum Dot/Silver Nanoparticle/Polyoxometalate Composites as Photocatalysts for Overall Water Splitting in Visible Light. *ChemCatChem, 6* (9), 2634-2641.

Liu, Q., Yuan, Y., Li, J., Liu, J., Hu, C., Chen, M., Lin, L., Kou, H., Shi, Y. & Liu, W. (2014). Preparation and properties of transparent Eu: YAG fluorescent ceramics with different doping concentrations. *Ceramics International, 40* (6), 8539-8545.

Loembe, L.-M., Fu, Z., Wang, W. & Wang, H. (2015). Sol-gel synthesis and characterization of lithium yttrium oxide. *International Journal of Research in Engineering and Technology, 4* (06), 1-7.

Lopez, T., Sanchez, E., Bosch, P., Meas, Y. & Gomez, R. (1992). FTIR and UV-Vis (diffuse reflectance) spectroscopic characterization of TiO2 sol-gel. *Materials Chemistry and Physics, 32* (2), 141-152.

López, T., Bosch, P., Asomoza, M., Gómez, R. & Ramos, E. (1997). DTA-TGA and FTIR spectroscopies of sol-gel hydrotalcites: aluminum source effect on physicochemical properties. *Materials Letters, 31* (3), 311-316.

Lu, Q., Dong, W., Wang, H. & Wang, X. (2002). A Novel Way to Synthesize Yttrium Aluminum Garnet from Metal–Inorganic Precursors. *Journal of the American Ceramic Society, 85* (2), 490-492.

Luna-Arredondo, E., Maldonado, A., Asomoza, R., Acosta, D., Melendez-Lira, M. & Olvera, M. d. l. L. (2005). Indium-doped ZnO thin films deposited by the sol–gel technique. *Thin Solid Films, 490* (2), 132-136.

Luo, J., Wang, Y. & Zhang, Q. (2018). Progress in perovskite solar cells based on ZnO nanostructures. *Solar Energy, 163*, 289-306.

Ma, H. & Wu, C. (2023). Chapter 6 - Feasibility and performance evaluation of cementitious material mixed with coal gangue solid waste. In *Managing Mining and Minerals Processing Wastes* (99-130): Elsevier.

Machrouhi, A., Khiar, H., Elhalil, A., Sadiq, M., Abdennouri, M. & Barka, N. (2023). Synthesis, characterization, and photocatalytic degradation of anionic dyes using a novel ZnO/activated carbon composite. *Watershed Ecology and the Environment, 5*, 80-87.

Mahdavi, R. & Talesh, S. S. A. (2017). The effect of ultrasonic irradiation on the structure, morphology and photocatalytic performance of ZnO nanoparticles by sol-gel method. *Ultrasonics Sonochemistry, 39*, 504-510.

Malato, S., Fernández-Ibáñez, P., Maldonado, M. I., Blanco, J. & Gernjak, W. (2009). Decontamination and disinfection of water by solar photocatalysis: recent overview and trends. *Catalysis today, 147* (1), 1-59.

Manalert, R. & Rahaman, M. N. (1996). Sol-gel processing and sintering of yttrium aluminum garnet (YAG) powders. *Journal of Materials Science, 31* (13), 3453-3458.

Martín-García, B., Paulo, P. M. R., Costa, S. M. B. & Velázquez, M. M. (2013). Photoluminescence Dynamics of CdSe QD/Polymer Langmuir–Blodgett Thin Films: Morphology Effects. *The Journal of Physical Chemistry C, 117* (28), 14787-14795.

Mendoza-Núñez, E. M., Solis-García, A., Ortiz-Domínguez, C., Soto-Arteaga, C. E., Domínguez, D., Contreras, O. E., Fuentes-Moyado, S. & Díaz de León, J. N. (2022). Insight into alcohol transformation over binary Al2O3-Y2O3 mixed oxide nanoparticles. *Applied Catalysis B: Environmental, 315*, 121567.

Meng, F., Liu, Y., Wang, J., Tan, X., Sun, H., Liu, S. & Wang, S. (2018). Temperature dependent photocatalysis of g-C3N4, TiO2 and ZnO: Differences in photoactive mechanism. *Journal of Colloid and Interface Science, 532*, 321-330.

Meng, H. L., Cui, C., Shen, H. L., Liang, D. Y., Xue, Y. Z., Li, P. G. & Tang, W. H. (2012). Synthesis and photocatalytic activity of TiO2@CdS and CdS@TiO2 double-shelled hollow spheres. *Journal of Alloys and Compounds, 527*, 30-35.

Menzer, G. (1929). XX. Die Kristallstruktur der Granate. *Zeitschrift für Kristallographie - Crystalline Materials, 69* (1-6), 300-396.

Mills, A. & Le Hunte, S. (1997). An overview of semiconductor photocatalysis. *Journal of photochemistry and photobiology A: Chemistry, 108* (1), 1-35.

Mochane, M. J., Motloung, M. T., Mokhena, T. C. & Mofokeng, T. G. (2022). Morphology and Photocatalytic Activity of Zinc Oxide Reinforced Polymer Composites: A Mini Review. *Catalysts, 12* (11), 1439.

Mohamadpour, F. & Amani, A. M. (2024). Photocatalytic systems: reactions, mechanism, and applications. *RSC Advances, 14* (29), 20609-20645.

Mohamed, H. H., Hammami, I., Akhtar, S. & Youssef, T. E. (2019). Highly efficient Cu-phthalocyanine-sensitized ZnO hollow spheres for photocatalytic and antimicrobial applications. *Composites Part B: Engineering, 176*, 107314.

Mohamed, R., McKinney, D. & Sigmund, W. (2012). Enhanced nanocatalysts. *Materials Science and Engineering: R: Reports, 73* (1), 1-13.

Mohan, R., Krishnamoorthy, K. & Kim, S.-J. (2012). Enhanced photocatalytic activity of Cu-doped ZnO nanorods. *Solid State Communications, 152* (5), 375-380.

Mohd Razali, N. A., Wan Salleh, W. N., Aziz, F., Jye, L. W., Yusof, N. & Ismail, A. F. (2021). Review on tungsten trioxide as a photocatalysts for degradation of recalcitrant pollutants. *Journal of Cleaner Production, 309*, 127438.

Mudavakkat, V. H., Atuchin, V. V., Kruchinin, V. N., Kayani, A. & Ramana, C. V. (2012). Structure, morphology and optical properties of nanocrystalline yttrium oxide (Y2O3) thin films. *Optical Materials, 34* (5), 893-900.

Nachimuthu, S., Thangamani, C., Thiyagarajulu, N., Thangaraj, K., Paramasivam, D., Thangavel, S., Kannan, K., Parvathiraja, C., Visalakshi, V. B., Velmurugan, P., Chinnathambi, A., Alharbi, S. A. & Basavegowda, N. (2023). Facile synthesis of ZnO-Y2O3 nanocomposite for photocatalytic and biological applications. *Catalysis Communications, 184*, 106786.

Nasir, M., Xi, Z., Xing, M., Zhang, J., Chen, F., Tian, B. & Bagwasi, S. (2013). Study of Synergistic Effect of Ce- and S-Codoping on the Enhancement of Visible-Light Photocatalytic Activity of TiO2. *The Journal of Physical Chemistry C, 117* (18), 9520-9528.

Niu, P., Dai, J., Zhi, X., Xia, Z., Wang, S. & Li, L. (2021). Photocatalytic overall water splitting by graphitic carbon nitride. *InfoMat, 3* (9), 931-961.

Núñez, J., Fresno, F., Platero-Prats, A. E., Jana, P., Fierro, J. L. G., Coronado, J. M., Serrano, D. P. & de la Peña O'Shea, V. A. (2016). Ga-Promoted Photocatalytic H2 Production over Pt/ZnO Nanostructures. *ACS Applied Materials & Interfaces, 8* (36), 23729-23738.

O'Hara, P. & Kovács, A. (2022). The Pauli exclusion principle. *Unified field theory and occam's razor: simple solutions to deep questions. London: World Scientific*, 275-292.

Ohno, T., Murakami, N., Koyanagi, T. & Yang, Y. (2014). Photocatalytic reduction of CO2 over a hybrid photocatalyst composed of WO3 and graphitic carbon nitride (g-C3N4) under visible light. *Journal of CO2 Utilization, 6*, 17-25.

Ong, C. B., Ng, L. Y. & Mohammad, A. W. (2018). A review of ZnO nanoparticles as solar photocatalysts: Synthesis, mechanisms and applications. *Renewable and Sustainable Energy Reviews, 81*, 536-551.

Osipov, V. V., Rasuleva, A. V. & Solomonov, V. I. (2008). Luminescence of pure yttria. *Optics and Spectroscopy, 105* (4), 524-530.

Osipov, V. V., Solomonov, V. I., Spirina, A. V., Vovkotrub, E. G. & Strekalovskii, V. N. (2014). Raman scattering and luminescence of yttria nanopowders and ceramics. *Optics and Spectroscopy, 116* (6), 946-955.

Özgür, Ü., Alivov, Y. I., Liu, C., Teke, A., Reshchikov, M. A., Doğan, S., Avrutin, V., Cho, S.-J. & Morkoç, H. (2005). A comprehensive review of ZnO materials and devices. *Journal of Applied Physics, 98* (4).

Padmanabhan, P., Sreekumar, K., Thiyagarajan, T., Satpute, R., Bhanumurthy, K., Sengupta, P., Dey, G. & Warrier, K. (2006). Nano-crystalline titanium dioxide formed by reactive plasma synthesis. *Vacuum, 80* (11-12), 1252-1255.

Pan, M., Liu, J.-R., Yang, P., Lu, M.-K., Xu, D., Yuan, D.-R. & Chen, D.-R. (2001). Strong luminescence of pure and yttria doped zirconia xerogels. *Journal of Materials Science Letters, 20* (17), 1565-1567.

Park, G. D., Lee, J.-H., Lee, J.-K. & Kang, Y. C. (2014). Effect of esterification reaction of citric acid and ethylene glycol on the formation of multi-shelled cobalt oxide powders with superior electrochemical properties. *Nano Research, 7*, 1738-1748.

Pera-Titus, M., García-Molina, V., Baños, M. A., Giménez, J. & Esplugas, S. (2004). Degradation of chlorophenols by means of advanced oxidation processes: a general review. *Applied Catalysis B: Environmental, 47* (4), 219-256.

Pham, H. D., Tekalgne, M. A., Do, H. H., Nguyen, V.-H., Vo, D.-V. N., Cheng, C. K., Shokouhimehr, M., Nguyen, C. C., Singh, P., Raizada, P., Kim, S. Y. & Le, Q. V. (2021). Emerging photocatalysts for air purification. *Materials Letters, 288*, 129355.

Phasey, J., Vandamme, D. & Fallowfield, H. J. (2017). Harvesting of algae in municipal wastewater treatment by calcium phosphate precipitation mediated by photosynthesis, sodium hydroxide and lime. *Algal Research, 27*, 115-120.

Pierre, A. C. (2013). *Introduction to sol-gel processing*: Springer Science & Business Media.

Pirsaheb, M., Asadi, A., Sillanpää, M. & Farhadian, N. (2018). Application of carbon quantum dots to increase the activity of conventional photocatalysts: A systematic review. *Journal of Molecular Liquids, 271*, 857-871.

Porrawatkul, P., Nuengmatcha, P., Kuyyogsuy, A., Pimsen, R. & Rattanaburi, P. (2023). Effect of Na and Al doping on ZnO nanoparticles for potential application in sunscreens. *Journal of Photochemistry and Photobiology B: Biology, 240*, 112668.

Prazeres, A. R., Luz, S., Fernandes, F. & Jerónimo, E. (2020). Cheese wastewater treatment by acid and basic precipitation: Application of H2SO4, HNO3, HCl,

Ca(OH)2 and NaOH. *Journal of Environmental Chemical Engineering, 8* (2), 103556.

Qi, K., Cheng, B., Yu, J. & Ho, W. (2017). Review on the improvement of the photocatalytic and antibacterial activities of ZnO. *Journal of Alloys and Compounds, 727*, 792-820.

Qiu, F., Pu, X., Li, J., Liu, X., Pan, Y. & Guo, J. (2005). Thermal behavior of the YAG precursor prepared by sol–gel combustion process. *Ceramics International, 31* (5), 663-665.

Raizada, P., Sudhaik, A. & Singh, P. (2019). Photocatalytic water decontamination using graphene and ZnO coupled photocatalysts: A review. *Materials Science for Energy Technologies, 2* (3), 509-525.

Raji, R. & Gopchandran, K. G. (2017). ZnO nanostructures with tunable visible luminescence: Effects of kinetics of chemical reduction and annealing. *Journal of Science: Advanced Materials and Devices, 2* (1), 51-58.

Rao, R. P. (1996). Growth and characterization of Y2O3: Eu3+ phosphor films by sol-gel process. *Solid State Communications, 99* (6), 439-443.

Regnier, P., Sapin, M. & de Montpreville, C. T. (1989). On the substitution of Y2O3 with ZrO2 in the synthesis of YBa2Cu3O7-δ. *Superconductor Science and Technology, 2* (3), 173.

Richardson, S. D. (2010). Environmental mass spectrometry: emerging contaminants and current issues. *Analytical chemistry, 82* (12), 4742-4774.

Rodríguez, A., Rosal, R., Perdigón-Melón, J. A., Mezcua, M., Agüera, A., Hernando, M. D., Letón, P., Fernández-Alba, A. R. & García-Calvo, E. (2008). Ozone-Based Technologies in Water and Wastewater Treatment. In *Emerging Contaminants from Industrial and Municipal Waste: Removal Technologies* (127-175). Berlin, Heidelberg: Springer Berlin Heidelberg.

Rouquerol, J., Rouquerol, F., Llewellyn, P., Maurin, G. & Sing, K. (2013). *Adsorption by powders and porous solids: principles, methodology and applications*: Academic press.

Ruan, S.-K., Zhou, J.-G., Zhong, A.-M., Duan, J.-F., Yang, X.-B. & Su, M.-Z. (1998). Synthesis of Y3Al5O12:Eu3+ phosphor by sol-gel method and its luminescence behavior. *Journal of Alloys and Compounds, 275-277*, 72-75.

Salah, N., Habib, S. S., Khan, Z. H., Memic, A., Azam, A., Alarfaj, E., Zahed, N. & Al-Hamedi, S. (2011). High-energy ball milling technique for ZnO nanoparticles as antibacterial material. *International Journal of Nanomedicine, 6* (null), 863-869.

Saleh, R. & Djaja, N. F. (2014). UV light photocatalytic degradation of organic dyes with Fe-doped ZnO nanoparticles. *Superlattices and Microstructures, 74*, 217-233.

Samadi, M., Zirak, M., Naseri, A., Khorashadizade, E. & Moshfegh, A. Z. (2016). Recent progress on doped ZnO nanostructures for visible-light photocatalysis. *Thin Solid Films, 605*, 2-19.

Sammon, C., Mura, C., Yarwood, J., Everall, N., Swart, R. & Hodge, D. (1998). FTIR−ATR Studies of the Structure and Dynamics of Water Molecules in Polymeric Matrixes. A Comparison of PET and PVC. *The Journal of Physical Chemistry B, 102* (18), 3402-3411.

Santos, J. C. A., Silva, E. P., Sampaio, D. V., Alves, Y. G. S., Rezende, M. V. S., Kucera, C., Ballato, J. & Silva, R. S. (2019). Structural, microstructural, and luminescent properties of laser-sintered Eu-doped YAG ceramics. *Optical Materials, 89*, 334-339.

Sasabe, H. & Kido, J. (2013). Recent Progress in Phosphorescent Organic Light-Emitting Devices. *European Journal of Organic Chemistry, 2013* (34), 7653-7663.

Serpone, N. (1997). Relative photonic efficiencies and quantum yields in heterogeneous photocatalysis. *Journal of Photochemistry and Photobiology A: Chemistry, 104* (1), 1-12.

Setlur, A. & Srivastava, A. (2007). On the relationship between emission color and Ce3+ concentration in garnet phosphors. *Optical Materials, 29* (12), 1647-1652.

Shimpi, N. G., Jain, S., Karmakar, N., Shah, A., Kothari, D. & Mishra, S. (2016). Synthesis of ZnO nanopencils using wet chemical method and its investigation as LPG sensor. *Applied Surface Science, 390*, 17-24.

Shinde, K. N., Dhoble, S. J., Swart, H. C. & Park, K. (2012). Basic Mechanisms of Photoluminescence. In *Phosphate Phosphors for Solid-State Lighting* (41-59). Berlin, Heidelberg: Springer Berlin Heidelberg.

Shionoya, S., Yen, W. M. & Yamamoto, H. (2018). *Phosphor handbook*: CRC press.

Siahsahlan, M., Aref, S. M., Naghshara, H. & Azmayesh, R. (2024). Optical characteristics and stability of ZnO-NPs/Graphene composites for visible light-driven hydrogen generation. *Ceramics International*.

Silva, C. G., Sampaio, M. J., Carabineiro, S. A. C., Oliveira, J. W. L., Baptista, D. L., Bacsa, R., Machado, B. F., Serp, P., Figueiredo, J. L., Silva, A. M. T. & Faria, J. L. (2014). Developing highly active photocatalysts: Gold-loaded ZnO for solar phenol oxidation. *Journal of Catalysis, 316*, 182-190.

Silva, J. M. P., Julião, R. S., Nicácio, T. C. N., Melo, M. C. N., Santos, R. M., Bomio, M. R. D. & Motta, F. V. (2024). A study of Nb-doped ZnO ceramic and its enhanced solar photocatalysis, photoluminescence and antimicrobial properties. *Journal of Alloys and Compounds, 985*, 173978.

Sim, S. M., Keller, K. A. & Mah, T. I. (2000). Phase formation in yttrium aluminum garnet powders synthesized by chemical methods. *Journal of Materials Science, 35* (3), 713-717.

Singh, A., Chaudhary, S. & Pandya, D. K. (2016). High conductivity indium doped ZnO films by metal target reactive co-sputtering. *Acta Materialia, 111*, 1-9.

Siswanto, Rochman, N. T. & Akwalia, P. R. (2017). Fabrication and characterization of Zinc Oxide (ZnO) nanoparticle by sol-gel method. *Journal of Physics: Conference Series, 853* (1), 012041.

Solomonov, V. V., Spirina, A. V., Spirin, A. V. & Paranin, S. N. (2016). Intrinsic luminescence centers in scandia, yttria, and their solid solutions. *Optics and Spectroscopy, 121* (5), 696-700.

Song, Z., Liao, J., Ding, X., Liu, X. & Liu, Q. (2013). Synthesis of YAG phosphor particles with excellent morphology by solid state reaction. *Journal of crystal growth, 365*, 24-28.

Soni, S., Teli, S., Teli, P. & Agarwal, S. (2024). Empowering sustainability: Charting the seven years of progress in g-C_3N_4 based materials and their crucial role in building a greener future. *Sustainable Chemistry and Pharmacy, 41*, 101693.

Šostar-Turk, S., Petrinić, I. & Simonič, M. (2005). Laundry wastewater treatment using coagulation and membrane filtration. *Resources, Conservation and Recycling, 44* (2), 185-196.

Speghini, A., Piccinelli, F. & Bettinelli, M. (2011). Synthesis, characterization and luminescence spectroscopy of oxide nanopowders activated with trivalent lanthanide ions: the garnet family. *Optical Materials, 33* (3), 247-257.

Stamnes, K. (2003). ULTRAVIOLET RADIATION. In *Encyclopedia of Atmospheric Sciences* (2467-2473). Oxford: Academic Press.

Su, T.-m., Qin, Z.-z., Ji, H.-b. & Jiang, Y.-x. (2014). Preparation, Characterization, and Activity of Y2O3-ZnO Complex Oxides for the Photodegradation of 2,4-Dinitrophenol. *International Journal of Photoenergy, 2014*, 794057.

Suárez, S., Carballa, M., Omil, F. & Lema, J. M. (2008). How are pharmaceutical and personal care products (PPCPs) removed from urban wastewaters? *Reviews in Environmental Science and Bio/Technology, 7* (2), 125-138.

Sun, H., Xu, X., Kim, H., Jung, W., Zhou, W. & Shao, Z. (2023). Electrochemical Water Splitting: Bridging the Gaps Between Fundamental Research and Industrial Applications. *ENERGY & ENVIRONMENTAL MATERIALS, 6* (5), e12441.

Sun, Z., Yuan, D., Li, H., Duan, X., Sun, H., Wang, Z., Wei, X., Xu, H., Luan, C., Xu, D. & Lv, M. (2004). Synthesis of yttrium aluminum garnet (YAG) by a new sol–gel method. *Journal of Alloys and Compounds, 379* (1), L1-L3.

Talebian, N., Amininezhad, S. M. & Doudi, M. (2013). Controllable synthesis of ZnO nanoparticles and their morphology-dependent antibacterial and optical properties. *Journal of Photochemistry and Photobiology B: Biology, 120*, 66-73.

Tangcharoen, T., Klysubun, W. & Kongmark, C. (2018). Synthesis of nanocrystalline NiO/ZnO heterostructured composite powders by sol-gel auto combustion method and their characterizations. *Journal of Molecular Structure, 1156*, 524-533.

Tian, N., Huang, H., Du, X., Dong, F. & Zhang, Y. (2019). Rational nanostructure design of graphitic carbon nitride for photocatalytic applications. *Journal of Materials Chemistry A, 7* (19), 11584-11612.

Tian, S., Liu, Q., Sun, J., Zhu, M., Wu, S. & Zhao, X. (2019). Mesoporous ZnO nanorods array with a controllable area density for enhanced photocatalytic properties. *Journal of Colloid and Interface Science, 534*, 389-398.

Tissue, B. M. & Yuan, H. B. (2003). Structure, particle size, and annealing of gas phase-condensed Eu3+:Y2O3 nanophosphors. *Journal of Solid State Chemistry, 171* (1), 12-18.

Toyoda, M., Watanabe, J. & Matsumiya, T. (1999). Evolution of Structure of the Precursor During Sol-Gel Processing of ZnO and Low Temperature Formation of Thin Films. *Journal of Sol-Gel Science and Technology, 16* (1), 93-99.

Trandafilović, L. V., Jovanović, D. J., Zhang, X., Ptasińska, S. & Dramićanin, M. (2017). Enhanced photocatalytic degradation of methylene blue and methyl orange by ZnO: Eu nanoparticles. *Applied Catalysis B: Environmental, 203*, 740-752.

Trandafilović, L. V., Jovanović, D. J., Zhang, X., Ptasińska, S. & Dramićanin, M. D. (2017). Enhanced photocatalytic degradation of methylene blue and methyl orange by ZnO:Eu nanoparticles. *Applied Catalysis B: Environmental, 203*, 740-752.

Tynell, T. & Karppinen, M. (2014). Atomic layer deposition of ZnO: a review. *Semiconductor Science and Technology, 29* (4), 043001.

Tzu, F.-M., Chen, J.-S. & Hsu, S.-H. (2021). Light Emitted Diode on Detecting Thin-Film Transistor through Line-Scan Photosensor. *Micromachines, 12* (4), 434.

Valeur, B. & Berberan-Santos, M. N. (2011). A brief history of fluorescence and phosphorescence before the emergence of quantum theory. *Journal of Chemical Education, 88* (6), 731-738.

Van Gerven, T., Mul, G., Moulijn, J. & Stankiewicz, A. (2007). A review of intensification of photocatalytic processes. *Chemical Engineering and Processing: Process Intensification, 46* (9), 781-789.

Veith, M., Mathur, S., Kareiva, A., Jilavi, M., Zimmer, M. & Huch, V. (1999). Low temperature synthesis of nanocrystalline Y3Al5O12 (YAG) and Ce-doped Y3Al5O12via different sol–gel methods. *Journal of Materials Chemistry, 9* (12), 3069-3079.

Velázquez, J. J., Fernández-González, R., Díaz, L., Pulido Melián, E., Rodríguez, V. D. & Núñez, P. (2017). Effect of reaction temperature and sacrificial agent on the photocatalytic H2-production of Pt-TiO2. *Journal of Alloys and Compounds, 721*, 405-410.

Vetrone, F., Boyer, J.-C., Capobianco, J. A., Speghini, A. & Bettinelli, M. (2003). Concentration-dependent near-infrared to visible upconversion in nanocrystalline and bulk Y2O3: Er3+. *Chemistry of Materials, 15* (14), 2737-2743.

Virk, H. S. (2015). History of Luminescence from Ancient to Modern Times. *Defect and Diffusion Forum, 361*, 1-13.

Vittal, R. & Ho, K.-C. (2017). Zinc oxide based dye-sensitized solar cells: A review. *Renewable and Sustainable Energy Reviews, 70*, 920-935.

Wang, J., Mandelis, A., Sun, Q., Li, B. & Gao, C. (2018). Temperature- and Size-Dependent Exciton Dynamics in PbS Colloidal Quantum Dot Thin Films Using

Combined Photoluminescence Spectroscopy and Photocarrier Radiometry. *The Journal of Physical Chemistry C, 122* (10), 5759-5766.

Wang, L., Yang, W., Ding, Y., Ren, Y., Xiao, S., Liu, B., Sinogeikin, S. V., Meng, Y., Gosztola, D. J., Shen, G., Hemley, R. J., Mao, W. L. & Mao, H.-k. (2010). Size-Dependent Amorphization of Nanoscale Y2O3 at High Pressure. *Physical Review Letters, 105* (9), 095701.

Wang, L., Zhao, F., Zhang, M., Hou, T., Li, Z., Pan, C. & Huang, H. (2016). Preparation and photoluminescence properties of YAG:Ce3+ phosphors by a series of amines assisted co-precipitation method. *Journal of Alloys and Compounds, 661*, 148-154.

Wang, L., Wang, K., He, T., Zhao, Y., Song, H. & Wang, H. (2020). Graphitic Carbon Nitride-Based Photocatalytic Materials: Preparation Strategy and Application. *ACS Sustainable Chemistry & Engineering, 8* (43), 16048-16085.

Wang, L. & Yu, J. (2023). Chapter 1 - Principles of photocatalysis. In *Interface Science and Technology* (1-52): Elsevier.

Wen, Y., Ding, H. & Shan, Y. (2011). Preparation and visible light photocatalytic activity of Ag/TiO 2/graphene nanocomposite. *Nanoscale, 3* (10), 4411-4417.

Wintgens, T., Salehi, F., Hochstrat, R. & Melin, T. (2008). Emerging contaminants and treatment options in water recycling for indirect potable use. *Water Science and Technology, 57* (1), 99-107.

Woan, K., Pyrgiotakis, G. & Sigmund, W. (2009). Photocatalytic carbon-nanotube–TiO2 composites. *Advanced Materials, 21* (21), 2233-2239.

Wu, H.-L., Li, X.-B., Tung, C.-H. & Wu, L.-Z. (2019). Semiconductor Quantum Dots: An Emerging Candidate for CO2 Photoreduction. *Advanced Materials, 31* (36), 1900709.

Wu, S., Pan, Z., Chen, R. & Liu, X. (2017). Fundamentals of Luminescent Materials. In *Long Afterglow Phosphorescent Materials* (1-19): Springer.

Xia, Z. & Liu, Q. (2016). Progress in discovery and structural design of color conversion phosphors for LEDs. *Progress in Materials Science, 84*, 59-117.

Xia, Z. & Meijerink, A. (2017). Ce 3+-Doped garnet phosphors: composition modification, luminescence properties and applications. *Chemical Society Reviews, 46* (1), 275-299.

Xu, T., Zhang, L., Cheng, H. & Zhu, Y. (2011). Significantly enhanced photocatalytic performance of ZnO via graphene hybridization and the mechanism study. *Applied Catalysis B: Environmental, 101* (3), 382-387.

Xue, B. & Zou, Y. (2018). High photocatalytic activity of ZnO–graphene composite. *Journal of Colloid and Interface Science, 529*, 306-313.

Yacobi, B. & Holt, D. (1986). Cathodoluminescence scanning electron microscopy of semiconductors. *Journal of applied physics, 59* (4), R1-R24.

Yan, F., Liu, Z. T. & Liu, W. T. (2011). The properties of the Y2O3 films exposed at elevated temperature. *Physica B: Condensed Matter, 406* (14), 2827-2833.

Yan, X.-h., Zheng, S.-s., Yu, R.-m., Cai, J., Xu, Z.-w., Liu, C.-j. & Luo, X.-t. (2008). Preparation of YAG:Ce3+ phosphor by sol-gel low temperature combustion method and its luminescent properties. *Transactions of Nonferrous Metals Society of China, 18* (3), 648-653.

Yang, H. & Cheng, H. (2007). Controlling nitrite level in drinking water by chlorination and chloramination. *Separation and Purification Technology, 56* (3), 392-396.

Yang, H. K., Chung, J. W., Moon, B. K., Jeong, J. H., Jang, K.-w., Lee, H. S. & Yi, S. S. (2009). Photoluminescence investigations of YAG: Eu nanocomposite powder by high-energy ball milling. *Current Applied Physics, 9* (2), e86-e88.

Yang, H. K. & Jeong, J. H. (2010). Synthesis, crystal growth, and photoluminescence properties of YAG: Eu3+ phosphors by high-energy ball milling and solid-state reaction. *The Journal of Physical Chemistry C, 114* (1), 226-230.

Yang, L., Wang, G., Tang, C., Wang, H. & Zhang, L. (2005). Synthesis and photoluminescence of corn-like ZnO nanostructures under solvothermal-assisted heat treatment. *Chemical Physics Letters, 409* (4), 337-341.

Yang, L. & Liu, Z. (2007). Study on light intensity in the process of photocatalytic degradation of indoor gaseous formaldehyde for saving energy. *Energy Conversion and Management, 48* (3), 882-889.

Yang, Y., Li, X., Zhou, C., Xiong, W., Zeng, G., Huang, D., Zhang, C., Wang, W., Song, B., Tang, X., Li, X. & Guo, H. (2020). Recent advances in application of graphitic carbon nitride-based catalysts for degrading organic contaminants in water through advanced oxidation processes beyond photocatalysis: A critical review. *Water Research, 184*, 116200.

Yaqoob, A. A., Mohd Noor, N. H. b., Serrà, A. & Mohamad Ibrahim, M. N. (2020). Advances and Challenges in Developing Efficient Graphene Oxide-Based ZnO Photocatalysts for Dye Photo-Oxidation. *Nanomaterials, 10* (5), 932.

Yu, J., Xiong, J., Cheng, B. & Liu, S. (2005). Fabrication and characterization of Ag–TiO2 multiphase nanocomposite thin films with enhanced photocatalytic activity. *Applied Catalysis B: Environmental, 60* (3-4), 211-221.

Yu, P., Zhang, K., Huang, H., Wen, M., Li, Q., Zhang, W., Hu, C. & Zheng, W. (2017). Oxygen vacancies dependent phase transition of Y2O3 films. *Applied Surface Science, 410*, 470-478.

Zeng, H., Duan, G., Li, Y., Yang, S., Xu, X. & Cai, W. (2010). Blue Luminescence of ZnO Nanoparticles Based on Non-Equilibrium Processes: Defect Origins and Emission Controls. *Advanced Functional Materials, 20* (4), 561-572.

Zhai, Q., Xie, S., Fan, W., Zhang, Q., Wang, Y., Deng, W. & Wang, Y. (2013). Photocatalytic Conversion of Carbon Dioxide with Water into Methane: Platinum and Copper(I) Oxide Co-catalysts with a Core–Shell Structure. *Angewandte Chemie International Edition, 52* (22), 5776-5779.

Zhang, J., Zhang, Z., Tang, Z., Lin, Y. & Zheng, Z. (2002). Luminescent properties of Y2O3:Eu synthesized by sol–gel processing. *Journal of Materials Processing Technology, 121* (2), 265-268.

Zhang, L. & Jaroniec, M. (2020). Chapter 2 - Fundamentals of adsorption for photocatalysis. In *Interface Science and Technology* (39-62): Elsevier.

Zhang, X., Wang, J., Guo, K., Chen, H., Yang, X. & Zhao, J. (2012). Synthesis and luminescence properties of Y2O3:Eu with flower-like microstructure. *Journal of Alloys and Compounds, 517*, 149-156.

Zhang, X., Gui, W. & Zeng, Q. (2017). First-principles study of structural, mechanical, and thermodynamic properties of cubic Y2O3 under high pressure. *Ceramics International, 43* (3), 3346-3355.

Zhang, Y. & Yu, H. (2009). Synthesis of YAG powders by the co-precipitation method. *Ceramics International, 35* (5), 2077-2081.

Zhao, G., Wang, M., Cao, X., Guo, Y., Liu, W. & Teng, H. (2020). Effects of pH on the microstructure and surface charge of BiVO4 prepared via hydrothermal method: formation mechanism and photocatalytic performance. *Research on Chemical Intermediates, 46* (2), 1487-1506.

Zhong Lin, W. (2004). Zinc oxide nanostructures: growth, properties and applications. *Journal of Physics: Condensed Matter, 16* (25), R829.

Zhu, L., Li, H., Xia, P., Liu, Z. & Xiong, D. (2018). Hierarchical ZnO Decorated with CeO2 Nanoparticles as the Direct Z-Scheme Heterojunction for Enhanced Photocatalytic Activity. *ACS Applied Materials & Interfaces, 10* (46), 39679-39687.

Zhu, Q. Q., Hu, W. W., Ju, L. C., Hao, L. Y., Xu, X. & Agathopoulos, S. (2013). Synthesis of 3512:2+ Phosphor by a Facile Hydrogen Iodide-AssistedSol–Gel Method. *Journal of the American Ceramic Society, 96* (3), 701-703.

Zink, J. I., Hardy, G. E. & Sutton, J. E. (1976). Triboluminescence of sugars. *The Journal of Physical Chemistry, 80* (3), 248-249.

Zinkevich, M. (2007). Thermodynamics of rare earth sesquioxides. *Progress in Materials Science, 52* (4), 597-647.